

Gravity stratified mixed convection in liquid metal pools:  
implications and experimental interpretation for LMFBRs

by

Brendan C. Ward

B.S., Iowa State University, 2013

---

AN ABSTRACT OF A DISSERTATION

submitted in partial fulfillment of the  
requirements for the degree

DOCTOR OF PHILOSOPHY

Alan Levin Department of Mechanical and Nuclear Engineering  
Carl R. Ice College of Engineering

KANSAS STATE UNIVERSITY  
Manhattan, Kansas

2020

# Abstract

Understanding stratification and mixing in large enclosures, how buoyancy effects the dispersion of concentration or temperature, plays an important role in safety analyses for the gamut of nuclear reactor types. In the upper plena of pool-type liquid metal cooled fast reactors (LMFRs) this phenomenon becomes more complex due to the extremely strong thermal diffusion (Prandtl number,  $Pr \ll 1$ ) of the liquid metal coolant, making safety envelope predictions difficult. High fidelity experimental data on thermal stratification is needed to validate and improve safety analysis codes for LMFRs.

Design of an experimental facility and instrumentation becomes complicated with liquid sodium, the preferred coolant for U.S. based LMFR designs. A surrogate fluid simplifies the design and operation considerably, providing the flexibility to obtain high quality measurements. The scaled experimental facility, the Gallium Thermal-hydraulic Experiment (GaTE), is designed using verified models based upon similarity analysis and physical constraints of the advanced sensors. Liquid gallium ( $Pr \sim 0.025$ ) is chosen as a surrogate for liquid sodium ( $Pr \sim 0.005$ ) considering scaling factors, material handling constraints, and the capabilities of the sensors.

The advanced sensors are key to understanding stratification in the plenum. Distributed temperature is captured using fiber-optic interferometry based on the principles of Rayleigh backscattering. This technique allows for higher temporal resolution (22 Hz) and finer spatial pitch (2.6 mm throughout) than those employed by previous research. Distributed velocity is measured using ultrasonic Doppler velocimetry (UDV) since optical techniques are not possible with the opaque liquid metal. The pulsed UDV technique, capturing information at 19 Hz and 1 mm pitch, also provides the necessary high resolution, distributed information. These higher resolutions and distributed sensing allow investigation of key transient information. The higher temporal resolution allows the fluctuating component of temperature,  $T'$ ,

and velocity,  $w'$ , to be captured to relevant scales; the spatial resolution allows for accurate representation of their respective gradients. A variety of tests are needed to measure these parameters. Forced-circulation isothermal tests benchmark the velocity behavior without buoyant influences. Conversely, natural-circulation driven flows provide affirmation of loop dynamics under various ‘core’ conditions. Cold step-transients, with injection of colder fluid at the bottom of the plenum, investigate the transition where flow fluctuations can overcome the restorative buoyant forces. The output of these tests, simulated or experimental, provide the framework for the scaling analysis, model development, and model validation.

The scaling analysis investigated the effects of differences in  $Pr$ , average temperatures, size, and shape of the upper plenum on scaling distortions. These are computed with the help of model calculations and output parameters such as eddy thermal diffusivity ( $\kappa_\tau = \overline{w'T'}/\frac{\partial \overline{T}}{\partial z}$ ), quantifying the effect on the temporal temperature evolution during model transients. This parameter is empirically modeled as a function of geometry, material properties, flow, and temperature conditions of the jet entering the plenum.

The capabilities of the GaTE allow maneuvering and monitoring of the flux Richardson number ( $Ri_f = \frac{g\beta\overline{w'T'}}{u'w'\partial\overline{w}/\partial z}$ ) which signifies the transition from planar to fluctuating thermally stratified front. With the background for the unique spectral behavior in liquid metal outlined and verified, the framework for explaining the fluctuations on the thermal front is established. Using the spectral turbulence data, a map of  $\kappa_\tau$  is constructed and compares well with the scaling analysis empirical model and the molecular diffusivity. Experimental data match global expectations of the empirically modeled and measured turbulent Prandtl number ( $Pr_\tau = (\overline{u'w'}/\frac{\partial\overline{w}}{\partial z})/(\overline{w'T'}/\frac{\partial\overline{T}}{\partial z})$ ). The behavior unique to liquid metal thermal stratification is explained: the relatively weak influence of buoyancy due to the strong horizontal diffusion of temperature; and the sustained turbulent action of the momentum in the inertial-diffusive governed flows increases the  $\kappa_\tau$  despite relatively calm thermal behavior.

Throughout this dissertation, the understanding of  $\kappa_\tau$  and  $Pr_\tau$  have been used, interpreted, and expanded upon. Liquid metal’s uniquely low  $Pr$  in stably stratified turbulence was explored and understood through specialized advanced sensors, allowing a deeper fundamental understanding for higher accuracy in system level safety analysis codes for LMFRRs.

Gravity stratified mixed convection in liquid metal pools:  
implications and experimental interpretation for LMFBRs

by

Brendan C. Ward

B.S., Iowa State University, 2013

---

A DISSERTATION

submitted in partial fulfillment of the  
requirements for the degree

DOCTOR OF PHILOSOPHY

Alan Levin Department of Mechanical and Nuclear Engineering  
Carl R. Ice College of Engineering

KANSAS STATE UNIVERSITY  
Manhattan, Kansas

2020

Approved by:

Major Professor  
Hitesh Bindra

# Copyright

© Brendan C. Ward.

# Abstract

Understanding stratification and mixing in large enclosures, how buoyancy effects the dispersion of concentration or temperature, plays an important role in safety analyses for the gamut of nuclear reactor types. In the upper plena of pool-type liquid metal cooled fast reactors (LMFRs) this phenomenon becomes more complex due to the extremely strong thermal diffusion (Prandtl number,  $Pr \ll 1$ ) of the liquid metal coolant, making safety envelope predictions difficult. High fidelity experimental data on thermal stratification is needed to validate and improve safety analysis codes for LMFRs.

Design of an experimental facility and instrumentation becomes complicated with liquid sodium, the preferred coolant for U.S. based LMFR designs. A surrogate fluid simplifies the design and operation considerably, providing the flexibility to obtain high quality measurements. The scaled experimental facility, the Gallium Thermal-hydraulic Experiment (GaTE), is designed using verified models based upon similarity analysis and physical constraints of the advanced sensors. Liquid gallium ( $Pr \sim 0.025$ ) is chosen as a surrogate for liquid sodium ( $Pr \sim 0.005$ ) considering scaling factors, material handling constraints, and the capabilities of the sensors.

The advanced sensors are key to understanding stratification in the plenum. Distributed temperature is captured using fiber-optic interferometry based on the principles of Rayleigh backscattering. This technique allows for higher temporal resolution (22 Hz) and finer spatial pitch (2.6 mm throughout) than those employed by previous research. Distributed velocity is measured using ultrasonic Doppler velocimetry (UDV) since optical techniques are not possible with the opaque liquid metal. The pulsed UDV technique, capturing information at 19 Hz and 1 mm pitch, also provides the necessary high resolution, distributed information. These higher resolutions and distributed sensing allow investigation of key transient information. The higher temporal resolution allows the fluctuating component of temperature,  $T'$ ,

and velocity,  $w'$ , to be captured to relevant scales; the spatial resolution allows for accurate representation of their respective gradients. A variety of tests are needed to measure these parameters. Forced-circulation isothermal tests benchmark the velocity behavior without buoyant influences. Conversely, natural-circulation driven flows provide affirmation of loop dynamics under various ‘core’ conditions. Cold step-transients, with injection of colder fluid at the bottom of the plenum, investigate the transition where flow fluctuations can overcome the restorative buoyant forces. The output of these tests, simulated or experimental, provide the framework for the scaling analysis, model development, and model validation.

The scaling analysis investigated the effects of differences in  $Pr$ , average temperatures, size, and shape of the upper plenum on scaling distortions. These are computed with the help of model calculations and output parameters such as eddy thermal diffusivity ( $\kappa_\tau = \overline{w'T'}/\frac{\partial \overline{T}}{\partial z}$ ), quantifying the effect on the temporal temperature evolution during model transients. This parameter is empirically modeled as a function of geometry, material properties, flow, and temperature conditions of the jet entering the plenum.

The capabilities of the GaTE allow maneuvering and monitoring of the flux Richardson number ( $Ri_f = \frac{g\beta\overline{w'T'}}{u'w'\partial\overline{w}/\partial z}$ ) which signifies the transition from planar to fluctuating thermally stratified front. With the background for the unique spectral behavior in liquid metal outlined and verified, the framework for explaining the fluctuations on the thermal front is established. Using the spectral turbulence data, a map of  $\kappa_\tau$  is constructed and compares well with the scaling analysis empirical model and the molecular diffusivity. Experimental data match global expectations of the empirically modeled and measured turbulent Prandtl number ( $Pr_\tau = (\overline{u'w'}/\frac{\partial\overline{w}}{\partial z})/(\overline{w'T'}/\frac{\partial\overline{T}}{\partial z})$ ). The behavior unique to liquid metal thermal stratification is explained: the relatively weak influence of buoyancy due to the strong horizontal diffusion of temperature; and the sustained turbulent action of the momentum in the inertial-diffusive governed flows increases the  $\kappa_\tau$  despite relatively calm thermal behavior.

Throughout this dissertation, the understanding of  $\kappa_\tau$  and  $Pr_\tau$  have been used, interpreted, and expanded upon. Liquid metal’s uniquely low  $Pr$  in stably stratified turbulence was explored and understood through specialized advanced sensors, allowing a deeper fundamental understanding for higher accuracy in system level safety analysis codes for LMFRRs.

# Table of Contents

|  |       |
|--|-------|
| List of Figures . . . . .  | xi    |
| List of Tables . . . . .   | xvii  |
| Nomenclature . . . . .   | xviii |
| Acknowledgements . . . . .   | xix   |
| 1 Introduction . . . . .   | 1     |
| 1.1 Liquid Metal Cooled Fast Reactors and thermal stratification . . . . . | 2     |
| 1.2 The impact of thermal stratification on nuclear safety . . . . .       | 2     |
| 1.2.1 Thermal fatigue . . . . .  | 4     |
| 1.2.2 Core reactivity . . . . .  | 5     |
| 1.2.3 Natural circulation – core cooling . . . . .                         | 5     |
| 1.3 Conditions required for thermal stratification . . . . .               | 6     |
| 1.3.1 What makes liquid metals different? . . . . .                        | 8     |
| 1.4 Challenges with data collection . . . . .                              | 10    |
| 1.4.1 Modeling and liquid metals . . . . .                                 | 10    |
| 1.4.2 Experimental experience in liquid metals . . . . .                   | 11    |
| 1.5 This work . . . . .  | 12    |
| 2 Scaling the upper plenum . . . . .                                       | 14    |
| 2.1 Scaling needs . . . . .  | 15    |
| 2.2 Methodology of scaling analysis . . . . .                              | 16    |
| 2.3 Similarity variables and design constraints . . . . .                  | 16    |
| 2.3.1 The other constraints . . . . .                                      | 20    |

|       |  |    |
|-------|--|----|
| 2.3.2 | Design of scaled-down model . . . . .                              | 21 |
| 2.4   | Evaluation of physics in different scales . . . . .                | 22 |
| 2.4.1 | Numerical simulations–Verification . . . . .                       | 24 |
| 2.5   | Results and discussion . . . . .                                   | 27 |
| 2.5.1 | Comparison of empirical and numerical results . . . . .            | 28 |
| 2.5.2 | Scaling evaluation . . . . .                                       | 29 |
| 2.6   | Evaluation summary . . . . .                                       | 31 |
| 3     | The Gallium Thermal-hydraulic Experiment (GaTE) facility . . . . . | 33 |
| 3.1   | GaTE system features . . . . .                                     | 34 |
| 3.1.1 | System flow control and measurement . . . . .                      | 34 |
| 3.1.2 | System temperature control and measurement . . . . .               | 34 |
| 3.2   | GaTE plenum features . . . . .                                     | 36 |
| 3.3   | Distributed temperature sensing . . . . .                          | 36 |
| 3.3.1 | Recent advancements . . . . .                                      | 36 |
| 3.3.2 | DTS working principles . . . . .                                   | 38 |
| 3.3.3 | Information from the SWI-DTS . . . . .                             | 40 |
| 3.4   | Ultrasonic Doppler Velocimetry (UDV) . . . . .                     | 41 |
| 3.4.1 | UDV working principles . . . . .                                   | 41 |
| 3.4.2 | Gallium oxide . . . . .  | 42 |
| 3.4.3 | Data collection parameters . . . . .                               | 44 |
| 3.4.4 | Verification of the UDV probe in the GaTE . . . . .                | 46 |
| 3.4.5 | Information from the UDV system . . . . .                          | 48 |
| 4     | Cold step-transient tests . . . . .                                | 52 |
| 4.1   | Balancing buoyancy and inertia . . . . .                           | 53 |
| 4.2   | Cold step-transient test procedure . . . . .                       | 53 |
| 4.2.1 | Experimental procedure . . . . .                                   | 53 |

|       |  |     |
|-------|--|-----|
| 4.2.2 | Experimental case studies . . . . .  | 54  |
| 4.3   | Results and discussion . . . . .   | 56  |
| 4.3.1 | Estimation of turbulent Prandtl number . . . . .                                       | 56  |
| 4.3.2 | Observation of critical $Ri$ in liquid metal . . . . .                                 | 57  |
| 4.4   | Critical $Ri$ behavior . . . . .   | 60  |
| 5     | Turbulent scaling laws and their influence on eddy diffusion in liquid metal . . . . . | 64  |
| 5.1   | Turbulent scaling framework . . . . .  | 65  |
| 5.2   | GaTE tests . . . . .   | 68  |
| 5.3   | Scaling law results . . . . .  | 69  |
| 5.3.1 | Transient evolution of turbulent scaling . . . . .                                     | 69  |
| 5.3.2 | Spectral Richardson number and BO59 scaling . . . . .                                  | 70  |
| 5.3.3 | The thermal microscale . . . . .   | 72  |
| 5.4   | Eddy diffusivity results . . . . .   | 75  |
| 5.4.1 | Mapping diffusivity measurements . . . . .   | 75  |
| 5.4.2 | Influence of scaling laws . . . . .  | 79  |
| 5.5   | Spectral synopsis . . . . .  | 82  |
| 6     | Conclusions . . . . .  | 83  |
|       | Bibliography . . . . .   | 86  |
| A     | Moving magnet pump characterization . . . . .  | 95  |
| B     | EMFM Calibration . . . . .   | 99  |
| C     | Despiking velocimetry signals . . . . .  | 105 |
| D     | Python scripts for Chapter 5 . . . . .   | 108 |
| E     | Instrumentation uncertainty and propagation of uncertainty . . . . .                   | 113 |
| F     | ICONE28-2020-16661 . . . . .   | 116 |

# List of Figures

|     |  |    |
|-----|--|----|
| 1.1 | Advanced Burner Test Reactor (ABTR) <sup>1</sup> , sodium cooled LMFR design, outlet plenum and internals. <sup>2</sup> . . . . .  | 3  |
| 1.2 | Thermally stratified interface development inside the outlet plenum of the ABTR <sup>1</sup> nearing the IHX entrance height . . . . .   | 4  |
| 1.3 | Illustration of reactor temperature reactivity feedback mechanisms. . . . .  | 6  |
| 1.4 | Illustration of thermal stratification interfaces with varying fluid properties. Colder fluid entering the hot plenum from below at the same bulk velocity has different axial temperature responses depending on combination of $Pr$ and thermo-fluid characteristics. . . . .  | 8  |
| 2.1 | Scale to scale representation (Equations 2.18 and 2.19) of the ABTR prototype and model plenum . . . . .   | 19 |
| 2.2 | 2-D sketch of the GaTE facility with dimensions. Vertical segregation into four regions for analysis. . . . .  | 22 |
| 2.3 | Mixing efficiency best fit functions of turbulence intensity for three zones: Molecular (M); Transitional (T); and Energetic (E). . . . .  | 24 |
| 2.4 | Scaled model of the proposed experimental facility. . . . .  | 25 |
| 2.5 | Thermally stratified interface progression in the outlet plenum model under varying flow rate colder fluid injection. Effect of different flow injection rates into the upper cavity model: the thermally stratified front has $Ri=553$ and $\kappa_\tau \ll \kappa$ ; the well mixed profile has $Ri=0.033$ and $\kappa_\tau > 148\kappa$ . . . . . | 27 |
| 2.6 | Comparison of empirical evaluation of mixing efficiency with that of the numerical evaluation. . . . .   | 29 |

|     |   |    |
|-----|---|----|
| 2.7 | Comparison between the ABTR and GaTE; the scaling distortion quantified by the mixing efficiency output. . . . .  | 30 |
| 3.1 | The GaTE system. Top: scaled upper plenum directly connected to three heat exchangers (2x side coolers; 1x bottom heater). Left (behind the Brendan): wall mounted VFD control panel and oil circulation heater connected by hose to the bottom heater. Bottom: moving magnet pump above the liquid storage tank. . . . . | 35 |
| 3.2 | GaTE plenum geometry and key component dimensions and locations. . . . .  | 37 |
| 3.3 | GaTE instrumentation platform and system components. . . . .  | 38 |
| 3.4 | Loss of flow test without heater trip - steady state natural circulation (N.C.) develops. With a heater trip, the temperature profile in the hot leg (plenum) progresses, lowering the natural circulation force. Left: system instrumentation; right: SWI-DTS information from the UIS pass (most central). . . . .      | 41 |
| 3.5 | Verification of UDV snapshot (blue), including mean (red) and $\pm$ one standard deviation (orange), to axial stage velocities (dashed black). . . . .  | 47 |
| 3.6 | Converged means of $U = 40$ and $60\text{mm/s}$ ( $Re = 7700, 10, 600$ ). Solid black lines are the medians of the respective replicates (3 for $40\text{mm/s}$ and 9 for $60\text{mm/s}$ ); dark fill is the IQR; and light fill shows maximum-minimum range. . . . .  | 48 |
| 3.7 | Statistics of dynamic contributions of the velocity differences of $U = 40$ and $60\text{mm/s}$ ( $Re = 7700, 10, 600$ ). Solid black lines are the medians of the respective replicates (3 for $40\text{mm/s}$ and 9 for $60\text{mm/s}$ ); dark fill is the IQR; and light fill shows maximum-minimum range. . . . .    | 49 |
| 3.8 | Isothermal contours of $U = 20, 40,$ and $60\text{mm/s}$ ( $Re = 3500, 7700, 10, 600$ ). Red lines show rise/run (displacement/time or velocity) of dominant eddies. At the core barrel height, solid-structure echoes cloud the signal; likewise, at the top, over saturation clouds the signal. . . . .                 | 51 |

|     |  |    |
|-----|--|----|
| 4.1 | (a) Components of the GaTE system used for manipulation of fluid conditions to ensure accurate and repeatable transients. (b) The pump speed is set to meet the set-point flow rate requirements of the test. (c) The scaled plenum is heated to the set-point temperature. (c) The transient is started and data collection established. . . . .          | 55 |
| 4.2 | Example transient system information: EMFM output (scaled to represent core $U$ ) and thermocouple readings are shown accompanied by plenum inlet and outlet height SWI-DTS information from the ‘outer’ DTS strand. . . . .   | 56 |
| 4.3 | SWI-DTS data at $tU/d \approx 26$ into two transients for all radial locations [‘UIS’, ‘Inner’, & ‘Outer’] next to SWI-DTS data for the entire transient for these locations. Horizontal dashed lines represent plenum exit channel height; vertical solid lines on the contour plots represent the time snapshot. . . . .                                 | 59 |
| 4.4 | Radial temperature difference in the fluid segments of the SWI-DTS (‘outer’-‘inner’) of three inlet conditions nearing the transition away from unidirectional. Time series data is plotted for the entire transients at the 0.20m (above the bottom) height. . . . .  | 60 |
| 4.5 | Axial temperature distribution of the ‘Inner’ SWI-DTS segment time-dependent contour (horizontal dashed lines represent plenum exit channel height). As $Ri_f$ approaches its theoretical critical value of 1, the stratification is transitioning away from unidirectional; below $Ri_f = 1$ clear fluctuations on the interface can be observed. . . . . | 61 |
| 4.6 | Regime transition through the critical flux Richardson number of 1. . . . .  | 62 |

|     |  |    |
|-----|--|----|
| 5.1 | Pictorial turbulence spectrum of the velocity and temperature shown with dashed line modifiers for active regions of the spectrum. Parallel lines in the passive region show -5/3 power law scaling (K41); vertical lines show important microscales: $k_B$ - Bolgiano (Active→Passive); $k_{\eta_T}$ - Obukov-Corrsin (inertial-convective → inertial-diffusive); and $k_\eta$ - Kolmogorov (inertial → diffusive). . . . . | 67 |
| 5.2 | Cold step-transient ( $Pe = 180, 260$ (left, right), $g\beta\Delta T = 0.006$ (both)) with temperature isotherms drawn in black over the velocity contour. Dashed black lines indicate exit channel dimensions. . . . .  | 68 |
| 5.3 | $Pe = 180$ spectral composition of $w'$ (isothermal-active transient-post transient :: left-right) and $T'$ (active - post transient :: left-right) at the $z = 125mm$ location. The active transient period shows similar theoretical features illustrated in Fig. 5.1. -5/3 power law lines are drawn for reference in each. . . . .   | 69 |
| 5.4 | $Ri_x$ : Spectral $Ri \sim (g\beta)k^{-1/2}\Gamma(k)^{1/2}/(kE(k))$ , two replicates (top,bottom) for each set of $Pe$ . $Ri_x = 1$ for active turbulence; the narrower the spectral range at unity, the more passive the behavior. . . . .  | 71 |
| 5.5 | Spectral $Ri$ (top) - color mapping elevation is consistent with Fig. 5.4. $Ri_x \approx 1$ (shaded region) compared to compensated ( $\times k^n$ ) spectra of $w'$ ( $E(k)$ ), $T'$ ( $\Gamma(k)$ ), and co-spectra $w'T'$ ( $\Sigma(k)$ ). . . . .  | 72 |
| 5.6 | $Ri_x \approx 1$ (shaded region) compared to compensated spectra of $w'$ ( $E(k)$ ), $T'$ ( $\Gamma(k)$ ), and co-spectra $w'T'$ ( $\Sigma(k)$ ). In the case with lower inlet velocity higher in the plenum, the BO59 scaling is replaced by inertial-diffusive temperature scaling. . . . .  | 73 |
| 5.7 | Compensated thermal spectra to identify inertial-diffusive scaling law regions; uncompensated corresponding spectra are shown in the insets. . . . .   | 74 |

|      |  |     |
|------|--|-----|
| 5.8  | Eddy thermal diffusivity measurement map for transients $Pe = 180$ (top) and $Pe = 260$ (bottom) with respective histograms. Blue dashed lines corresponding to their respective medians are provided as well as the lower ‘floor’ of the diffusivity. The black dotted line is the molecular value ( $1.2e-05[m^2/s]$ ). . . . .  | 76  |
| 5.9  | Normalized eddy thermal diffusivity measurements from the GaTE. The points represent all transient cases, $Pe = 180, 260$ at $g\beta\Delta T = 0.006$ (2 each), at all elevations measured during all temporal intervals. The grey band shows the smoothed empirical relationship described in Figure 2.3. . . . .   | 77  |
| 5.10 | $Pr_\tau$ spectral estimation. The black dashed line shows the empirical relationship $Pr_\tau = 0.85 + 182.4/(PrRe^{0.888})^3$ with the small dotted line representing the limit, $Pr_\tau = 0.85$ . Color mapping elevation is consistent with Fig. 5.9. . . . .   | 79  |
| 5.11 | Eddy thermal diffusivity measurements by measured $Ri$ ( $\frac{g\beta\sqrt{\langle(\partial T/\partial z)^2\rangle}}{\langle(\partial w'/\partial z)^2\rangle}$ )(left) and global average by global $Ri$ ( $\frac{g\beta\Delta T}{U^2}$ )(right) compared to the $\hat{\kappa}$ functions of the empirical parameterization <sup>4</sup> ( $\hat{\kappa}_{emp.} = f(Re_\tau/Ri)$ ) and modified empirical expectation for use with liquid metal ( $\hat{\kappa}_{emp.} = f(Re_\tau/Ri_f) = f(Re_\tau Pr_\tau/Ri)$ ). . . . . | 81  |
| A.1  | Pictorial representation of the disc-type moving magnet pump. . . . .  | 96  |
| A.2  | Suction (inlet) flanges of the GaTE pump. . . . .  | 96  |
| A.3  | The GaTE characteristic curves: pump and system limits. Pump affinity curves using $(\frac{N}{N_0}) = (\frac{Q}{Q_0})^2 = (\frac{H}{H_0})^1$ . . . . .   | 98  |
| B.1  | GaTE electromagnet flow meter: teflon pipe, grounded cage, and permanent magnet construction. Electric pickups measure the orthogonal emf as the conductive fluid moves through the transverse magnetic field. The pipe ID (and pickup screw distance) is 0.5", increasing the local velocity to produce a larger emf. . . . .   | 99  |
| B.2  | Calibration cylinder details and flow path. . . . .  | 100 |

|     |   |     |
|-----|---|-----|
| B.3 | Determination of calibration cylinder velocity (dots, solid lines); the corresponding EMFM output (multiplied by C factor) is shown for reference. . . .  | 102 |
| B.4 | Multiple tests were ensembled to determine the calibration constant (with a random half of the tests) while the other half were compared to the calibration constant to determine statistical agreement. . . . .                  | 103 |
| B.5 | EMFM error quantification from the calibration. . . . .   | 104 |
| C.1 | Pictorial representation of impact noise has on power spectral density of the measured UDV signal. Adapted from Durgesh et. al. <sup>5</sup> to include despiking. .  | 105 |
| C.2 | Phase space of velocity signal from GaTE UDV data. Circles identify the spikes outside of the ellipse. The left figure shows the raw signal; the right shows after the despiking is complete. . . . .                             | 106 |
| C.3 | Entire 6000 point isothermal test data of vertical velocity by time. Blue is raw; black is despiked signal. The red box on the left shows the display area of the right sub-figure. . . . .                                       | 107 |
| C.4 | Power spectral density of the UDV signal. Blue is raw; black is despiked signal; dashed line represents -5/3 power scaling. The relative effectiveness of the despiking method depends on the location within the plenum. . . . . | 107 |
| D.1 | Routines for PSD and integration and part 1/2 of data input. . . . .  | 109 |
| D.2 | Part 2/2 of data input. . . . .   | 110 |
| D.3 | Code to interpret and plot $\kappa$ by $Re_\tau/Ri$ part 1/2. . . . .   | 111 |
| D.4 | Code to interpret and plot $\kappa$ by $Re_\tau/Ri$ part 2/2. . . . .   | 112 |
| E.1 | Figure 3.5 shown here for reference. Verification of UDV snapshot (blue), including mean (red) and $\pm$ one standard deviation (orange), to axial stage velocities (dashed black). . . . .                                       | 114 |

# List of Tables

|     |  |     |
|-----|--|-----|
| 1.1 | Details of previous thermal stratification experiments. <sup>6</sup> . . . . .   | 11  |
| 2.1 | Parameters of the ABTR used for scaling analysis <sup>1</sup> . . . . .  | 18  |
| 2.2 | Unique solutions to Equations 2.14 and 2.15 for the fluid properties of the tabulated temperature range. $D$ characteristic length or effective ABTR core flow diameter. . . . . | 21  |
| 2.3 | Average mixing efficiency, $\hat{\kappa}$ , values for the outlet plenum of prototype ABTR and GaTE facility using the empirical model. . . . .                                  | 30  |
| 3.1 | Details of previous and ongoing thermal stratification experiments. . . . .  | 39  |
| 5.1 | Scaling laws of liquid metal mixed convection. $k^n$ dependence breakdown by scale regime and variable. . . . .  | 67  |
| E.1 | Instrumentation uncertainties . . . . .  | 114 |
| E.2 | Distributed velocity verification . . . . .  | 114 |
| E.3 | Uncertainty associated with turbulent flux parameters. . . . .   | 115 |

# Nomenclature

|                   |   | <b>Units</b>  |
|-------------------|---|---|
| $D$               | Characteristic Length   | $[m]$   |
| $U$               | Bulk fluid velocity   | $[ms^{-1}]$   |
| $\beta$           | Coefficient of thermal expansion  | $[^{\circ}C^{-1}]$  |
| $\rho$            | Fluid density   | $[kgm^{-3}]$  |
| $g$               | Gravitational constant  | $[ms^{-1}]$   |
| $z$               | Direction of gravity  |   |
| $T$               | Temperature   | $[^{\circ}C]$   |
| $u$               | Horizontal velocity field component                                     | $[ms^{-1}]$   |
| $w$               | Vertical velocity field component                                       | $[ms^{-1}]$   |
| $x'$              | Fluctuations on variable $x$  |   |
| $\bar{x}$         | Time average on variable $x$  |   |
| $\Delta T$        | Change in temperature (Hot - Cold)                                      | $[^{\circ}C]$   |
| $\kappa$          | Thermal diffusivity   | $[m^2s^{-1}]$   |
| $\nu$             | Kinematic viscosity   | $[m^2s^{-1}]$   |
| $\kappa_{\tau}$   | Eddy thermal diffusivity $\overline{w'T'}/(\partial\bar{T}/\partial z)$ | $[m^2s^{-1}]$   |
| $\nu_{\tau}$      | Eddy viscosity $\overline{u'w'}/(\partial\bar{w}/\partial z)$           | $[m^2s^{-1}]$   |
| <b>Definition</b> |   |   |
| $Pr$              | Prandtl number  | $\nu/\kappa$  |
| $Ri$              | Global Richardson number  | $g\beta(\Delta T)D/U^2$   |
| $Re$              | Reynolds number   | $UD/\nu$  |
| $Pe$              | Péclet number   | $UD/\kappa$   |
| $Pr_{\tau}$       | Turbulent Prandtl number  | $\nu_{\tau}/\kappa_{\tau}$  |
| $Ri_f$            | Flux Richardson number  | $g\beta\overline{w'T'}/(\overline{u'w'}\partial\bar{w}/\partial z)$ |

# Acknowledgments

This research was funded in part by the Department of Energy’s Nuclear Engineering University Program, under Grant no. DE-NE0008559 and DE-NE0008498.

I would like to thank my advisor, Dr. Hitesh Bindra, for all of his advice and guidance. He has constructed a research platform that has allowed me to tackle the problems presented in this dissertation with singular focus.

I also want to thank Dr. Terry Beck, Dr. Bret Flanders, Dr. Hrant Hakobyan, and Dr. Mingjun Wei for their time and being apart of my supervisory committee.

None of this would have been possible without the support of my wonderful wife, Erin.

And last but not least, my buddy, Lewis Fry Richardson, who is credited for the notion of a turbulent energy cascade and development of the modern framework of how we understand buoyant convection. His intuitive and poetic definition of turbulence worth sharing:

*“Big whorls have little whorls,  
which feed on their velocity;  
And little whorls have lesser whorls,  
And so on to viscosity.”*

# Chapter 1

## Introduction

## 1.1 Liquid Metal Cooled Fast Reactors and thermal stratification

Liquid metal cooled fast reactors (LMFRs) are one of the next generation of reactor designs which utilize passive cooling capabilities as a means of safely shutting down the reactor and maintaining their shutdown condition. The thermal-fluid characteristics of the liquid metal coolant allows density gradients during shutdown transients to drive natural circulation and heat removal from the reactor core. However, these same density gradients and natural circulation flow conditions lend themselves to thermal stratification in the upper plenum above the outlet of the reactor core under certain reactor transients.

As it is, system level codes are limited in their ability to capture thermal stratification. Cases where 3D computational fluid dynamics (CFD) codes are used to model high thermal diffusivity, mixed convection flows are computationally expensive. These require validation and experimental data sets are sparse. Understanding thermal stratification will allow for more accurate safety analyses to be conducted with the full impact on primary loop temperatures (coolant and solid-structure) to be known. These analyses will better inform the margins associated with reactor safety by understanding the mechanisms thermal stratification uses to influence nuclear safety.

## 1.2 The impact of thermal stratification on nuclear safety

The primary components and the design of a pool-type reactor system can be seen in Figure 1.1. Liquid metal coolant is circulated between the core and the intermediate heat exchangers (IHXs), where the nuclear power is delivered to the secondary loop in the process of power production or use<sup>7</sup>. An internal structure (redan) separates the hot and cold portions of the pool. In a shutdown reactor, during a loss of forced convection condition, the flow path is identical; however, the pumps previously forcing the fluid flow through the path are not operable. Instead, due to the large density variation in liquid metals (e.g. sodium, lead-bismuth eutectic) as a function of temperature, buoyancy driven natural circulation is the

reliable convective heat removal mechanism from the core. But these natural circulation driven flows are significantly smaller in magnitude, leading to thermal stratification in the upper (hot) plenum<sup>8</sup>. Buoyancy will maintain vertical temperature separation in the upper plenum with the higher density fluid entering from the shut down core settling at the bottom.

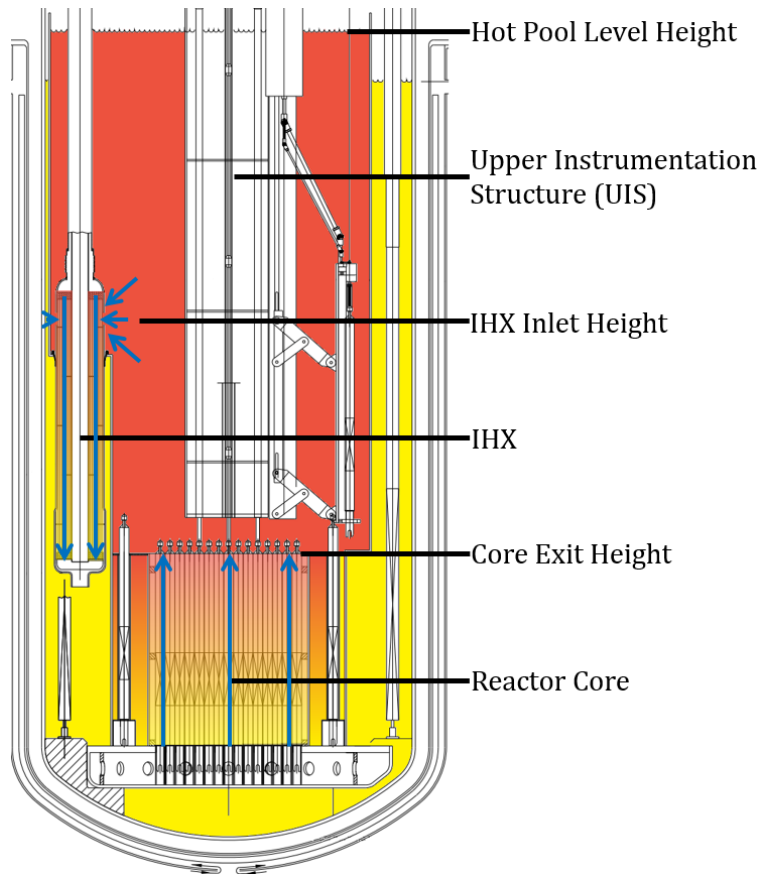


Figure 1.1: Advanced Burner Test Reactor (ABTR)<sup>1</sup>, sodium cooled LMFR design, outlet plenum and internals.<sup>2</sup>

For a given system, a low  $Pr$  fluid ( $Pr \ll 1$ , characteristic of liquid metals) will require much more inertia to mix the stratified zones because of their high molecular thermal diffusivity. Thermal stratification in LMFRs, especially outlet plenum, can cause design challenges and impact the overall safety of these reactors. In particular, the following phenomenon show the direct impact of thermal stratification on reactor safety: thermal fatigue at solid-liquid interfaces (mechanical), impact core reactivity (neutronics), and core cooling with natural circulation (thermal).

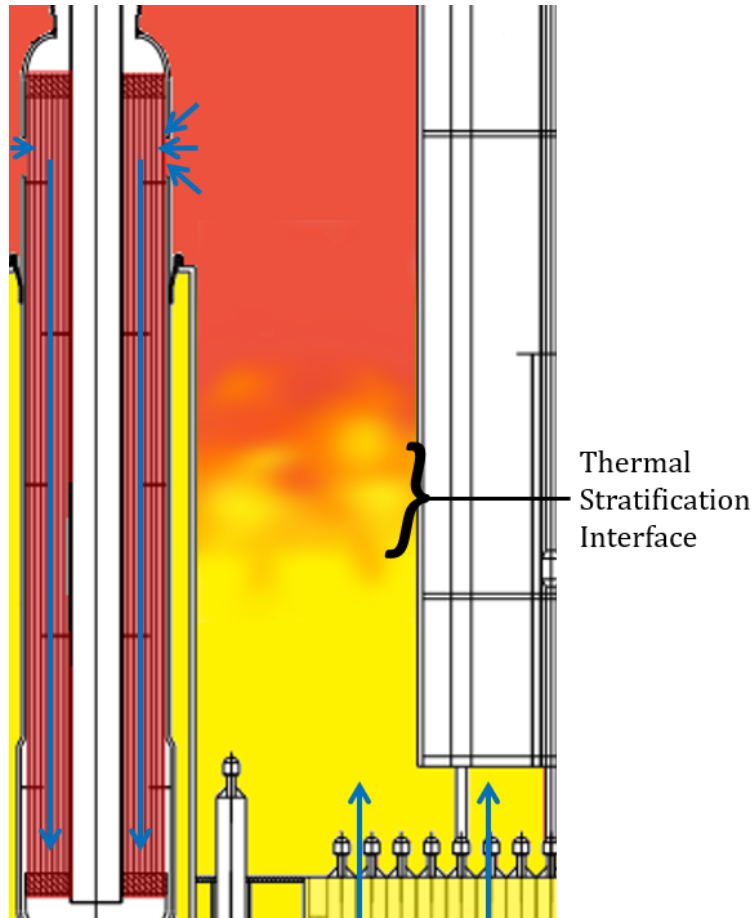


Figure 1.2: Thermally stratified interface development inside the outlet plenum of the ABTR<sup>1</sup> nearing the IHX entrance height

### 1.2.1 Thermal fatigue

The thermally stratified interface between the hot and cold zones can be small, with a very large change in temperature over a short length scale. As the interface is perturbed, its location relative to the solid structures inside the reactor can oscillate. These oscillations can cause sudden temperature changes in the solid structures leading to accelerated fatigue. The impact of accelerated thermal fatigue causes cracks to propagate in the structures such as the upper instrumentation structure (UIS - or, often, upper internal structure). This issue, caused by thermal stratification, can complicate design and, if not properly understood, could lead to unexpected premature failure of reactor components.

### 1.2.2 Core reactivity

The UIS, shown above the reactor centerline in Figure 1.1 houses the control rod drive-lines, as seen in Figure 1.3. During reactor shutdown the control rods are inserted in the reactor but the total rod worth is dependent on their position within the core. The control rod drive-line in the UIS can expand with an increase in local temperature, which can add negative reactivity into the system. Conversely, the lowering of control rod drive-line temperature causes contraction and removal of negative reactivity. Additional feedback based on the thermal response of the primary system includes fuel expansion (negative fuel temperature feedback) and vessel expansion, impacting the fuel-control rod proximity. The expansion and contraction of the control rod drive-line, fuel, and vessel are dependent on the local temperature of the surrounding fluid. Understanding thermal stratification, where the interface will be located, and how it will evolve can be used to understand the control rod reactivity contributions during transients more accurately.

### 1.2.3 Natural circulation – core cooling

The natural circulation circuit is driven by the density (temperature) difference between the fluid on either side of the redan. As the cold front enters the outlet plenum through the reactor core, the hot fluid is displaced and exits the plenum through the IHX inlet. As the temperature gradient evolves, the height of the interface can be at higher elevation or equal to the IHX inlet. Under such scenarios, colder fluid will flow through IHX to the cold plenum, leaving the hotter fluid to stagnate above. This reduces the heat transfer and natural circulation capabilities of the direct reactor auxiliary cooling system (DRACS). The coolant temperature exiting the hot plenum is the primary variable responsible for understanding how the overall passive cooling system will behave. Understanding the physics behind thermal stratification will allow designers to optimize these heights with respect to each other.

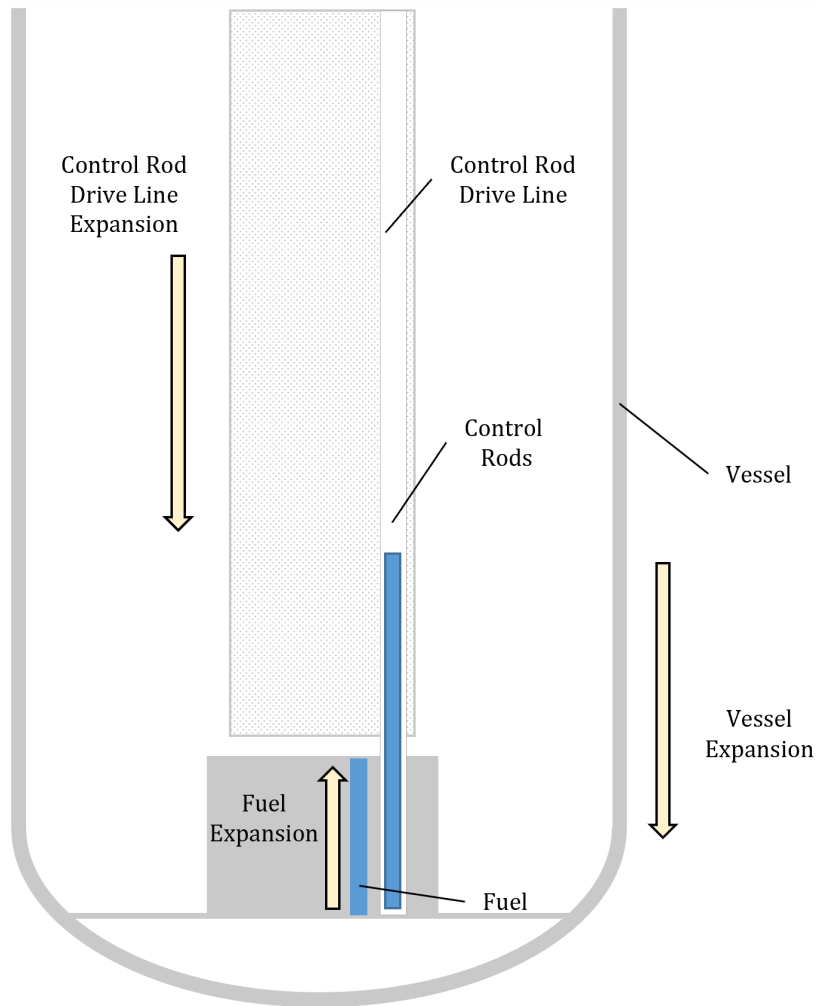


Figure 1.3: Illustration of reactor temperature reactivity feedback mechanisms.

### 1.3 Conditions required for thermal stratification

Thermal stratification is a state where convective flux is insufficient to disrupt the thermally driven positive density gradient in the direction of gravity. This buoyancy locked condition keeps the system under stable equilibrium and thermal gradients unidirectional.

In an opposite case, for example in the case of Rayleigh-Bénard convection, where the density gradient is directly against the direction of gravity, only a small flow perturbation is sufficient to trigger the flow circulation and thermal gradients are not unidirectional. Generally, the transient evolution of thermal profiles or interfaces in large liquid pools or enclosures is dependent upon the direction and magnitude of the density gradient, the magnitude of

external flow disturbances or perturbations, and fluid properties. How these interfaces behave or evolve under the conditions in-between the two aforementioned extreme scenarios are not well understood. This study focuses on thermally stratified pools and to understand the role of injected convective flux on the evolution of the interface.

The parameter to quantify the effect of convective flux on the state of stratification is the flux Richardson number:

$$Ri_f = \frac{g\beta\overline{w'T'}}{u'w'\partial\overline{w}/\partial z} \quad (1.1)$$

which is the ratio of the buoyant dissipation to shear production of the turbulent kinetic energy<sup>9-11</sup>). In a stable environment buoyant dissipation is greater than shear production ( $Ri_f > 1$ ) and the convective flux is insufficient to overturn the planar thermal front.

As expected from the definition, the critical flux Richardson number,  $Ri_{f,crit} \leq 1$ , is the sufficient criteria where the convective flux is able to promote thermal fluctuations about the stratified interface. Further reduction in this parameter,  $Ri_{f,crit} \leq 0$ , renders the system highly unstable. Although it is a well-defined and definitive way to establish the transition criteria, it is often difficult to measure the fluctuations in the flow field and temperature field simultaneously, even in the most carefully designed experiments. Therefore, a more easily quantifiable and measurable parameter is the global Richardson number,  $Ri$ , which signifies the ratio of buoyant forces to inertial forces. In a controlled experiment or even in a prototypical environment, the magnitude of  $Ri$  can be readily estimated. The fundamental relationship between  $Ri$  and  $Ri_f$  is given by

$$Ri = \frac{N^2}{(\frac{\partial\overline{w}}{\partial z})^2} = \left( \frac{\overline{u'w'}/(\frac{\partial\overline{w}}{\partial z})}{\overline{w'T'}/(\frac{\partial\overline{T}}{\partial z})} \right) \left( \frac{g\beta\overline{w'T'}}{\overline{u'w'}/(\frac{\partial\overline{w}}{\partial z})} \right) = Pr_\tau Ri_f \quad (1.2)$$

Where,  $N = \sqrt{g\beta\partial\overline{T}/\partial z}$ <sup>10</sup>, the Brunt-Väisällä frequency i.e. the characteristic frequency related to the buoyancy forces or the restorative forces to maintain a planar interface. The turbulent Prandtl number,  $Pr_\tau$ , is a function of the material property ( $Pr$ ) and the flow characteristics. There is a strong influence of  $Pr$  on the state of thermal stratification.

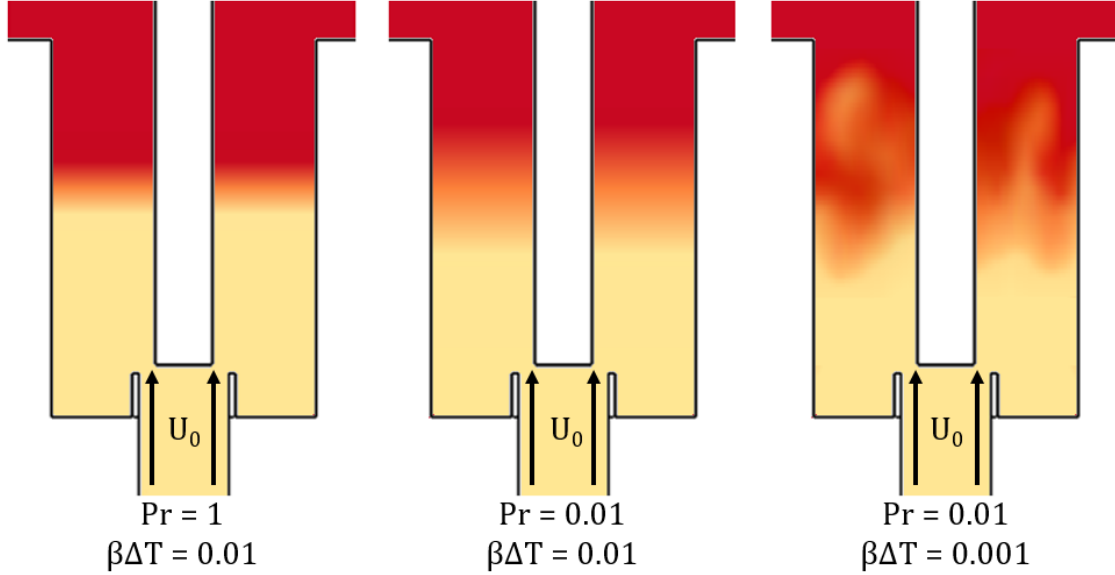


Figure 1.4: Illustration of thermal stratification interfaces with varying fluid properties. Colder fluid entering the hot plenum from below at the same bulk velocity has different axial temperature responses depending on combination of  $Pr$  and thermo-fluid characteristics.

### 1.3.1 What makes liquid metals different?

To illustrate the qualitative effect of material properties ( $Pr, \beta$ ) and buoyancy conditions under the same flow injection conditions, the state of thermally stratified interface in a liquid pool for three cases is depicted in Figure 1.4. Under strong buoyant influence, different  $Pr$  fluids both exhibit planar stratification fronts with the difference being the diffusion across the front. When buoyancy is reduced (as in the sub-figure on the right), the strong horizontal diffusion weakens the baroclinic torque ( $\nabla P \times g\beta\nabla T$ )<sup>12</sup>, reducing the impact of gravity. By how much it is reduced or how much it is masked by the diffusion widened front depends on the conditions under investigation.

In the case of fluids with  $Pr \ll 1$ , the value of  $Pr_\tau$  can be strongly dependent upon the flow conditions<sup>13</sup>, parameterized best by the Péclet number,  $Pe$  (the product of  $Pr$  and the Reynolds number,  $Re$ ). In a quantifiable example, in a sodium ( $Pr = 0.005$ ) pipe flow of  $Re = 10,000$ , where turbulent fluctuations of the velocity are expected to dictate local dynamics, the  $Pe$  is 50. In such a case, where local temperature inputs are communicated axially and spread by the strong molecular diffusivity, the behavior is unique and not expected for a case

where  $Pe > 100$ <sup>14;15</sup>, despite the  $Re$  being so large and momentum transfer locally defined. In a stratified pool, this allows rapid horizontal communication of the temperature, assisting in one-dimensionalization the temperature front.

Beyond the spatial impact on the temperature behavior, the  $Pr$  and  $Pe$  also play a critical role in the dynamics as well. For turbulent flows, the relative fluctuations of velocity at different time scales are well characterized by a turbulent energy cascade with relatively well-defined ratios between scales. At the smallest scales, molecular action begins to dominate and is characterized by the turbulent microscale (often called the Kolmogorov microscale after the foundational K41 theory<sup>16</sup>). Through dimensional arguments, the scale ( $\eta$ ) can be quantified by  $Re$ :

$$\frac{\eta}{L} = Re_L^{-3/4} \quad (1.3)$$

Analogously, there is a turbulent microscale for temperature, where the molecular action begins to dominate. It is quantified by the  $Pe$ :

$$\frac{\eta_T}{L} = Pe_L^{-3/4} \quad (1.4)$$

Where the relationship between the two can be shown<sup>17</sup>:  $\eta_T/\eta = Pr^{-3/4}$ .

These scales act as the cutoff scale at which the molecular low-pass filter acts. Clearly, for low  $Pr$  fluids, the scale at which the higher frequency thermal dynamics are damped out is much smaller than that of velocity.

Quantification of these scales and their effect on global dynamics, either by validated computational modeling tools or experimental measurement, is necessary for accurately predicting the behavior in safety analyses. However, neither of these options comes without their own challenges.

## 1.4 Challenges with data collection

### 1.4.1 Modeling and liquid metals

System level codes such as SAS4A/SASSYS-1 have been used to capture a wide variety of transient effects; however, they are not as accurate as CFD codes and are limited in their ability to capture thermal stratification effects under mixed convection<sup>18;19</sup>. Current modeling of large volumes (such as the upper plenum) are limited to either a perfect mixing model or a coarse 1D thermal stratification model, both of which can lead to divergence of the models from known reactor transients (such as EBR-II's SHRT-45R unprotected loss of flow test<sup>20</sup>). It has been shown that different plenum geometries impact the stratification behavior<sup>21;22</sup> and, since full scale tests on every potential geometry is not practical, there is still a need for better numerical models. A more accurate assessment by 3D CFD type codes would require significantly more computational time. So a solution needs to be found, one in which where 3D CFD derived models can be interpreted in the 1D system level codes. Solutions to CFD models are complicated with the use of a liquid metal coolant with strong thermal diffusivity properties in mixed convection flows.

The primary difficulties involved in modeling for LMFBRs are the geometric complexities and no one-size-fits-all modeling parameters. For example, models often use  $Pr_\tau$  as a constant, relying on Reynold's analogy ( $Pr_\tau = 1$  [or similar, often 0.85]) everywhere. In certain higher  $Pr$  flows this assumption does not affect the results of the simulation. But for liquid metals, the  $Pr_\tau$  may vary widely across a geometry, depending heavily on local flow variables, and drastically alter the results. Additionally, local anisotropy due to high buoyant influence requires additional modelling terms to more accurately represent reality<sup>23;24</sup>. Some of these problems can be avoided by modeling all scales (such as direct numerical simulation) or most scales (such as large eddy simulation with fine grid spacing) but this comes at higher computational cost. There is still limited experience with matching validation-quality experimental data to these models<sup>23;25</sup>. Therefore, any models derived from CFD outputs need to be validated with experimental data.

## 1.4.2 Experimental experience in liquid metals

Measurement of eddy flow and temperature parameters such as temperature gradients,  $\frac{dT}{dz}$ , and  $T'$ , seen in the eddy thermal diffusivity terms of  $Pr_\tau$  or  $Ri_f$ , are critical in ensuring a complete understanding of the stratification behavior and validation of numerical tools. However, the transport of turbulent energies in low Prandtl number fluids ( $Pr \ll 1$ ) under density stratified conditions still have very few data sets despite their importance in several fields (e.g. astrophysics<sup>26</sup>, continuous casting<sup>27</sup>, and nuclear reactors<sup>23</sup>). These quantities require high spatial and temporal resolutions in order to be captured. While some past experiments have resolved spatial pitches, temperature is not captured throughout the entire plenum with this same resolution. The enhanced spatial resolution is required in an effort to reduce higher order numerical error in calculation of the temperature gradient, a function of the pitch,  $h$ , squared:  $\mathcal{O}(\Delta h^2)$ .

There have been previous experimental reports on the understanding of thermal stratification or mixing in liquid metal reactor plena. A comparison of past experimental work involving temperature measurement in thermally stratified plena is provided in Table 1.1. All of these previous experiments used thermocouples as temperature sensors which have much larger temporal response times than the advanced methods available today. Estimation of eddy temperature,  $T'$ , requires capture of relevant higher frequency information as the breakdown between the averaged  $\bar{T}$  and fluctuating  $T'$  is based on the temporal interpretation of the signal. It is both of these features (lower  $\mathcal{O}(\Delta h^2)$  and higher fidelity  $T'$ ) that the temperature collection, detailed in Chapter 3, is able to excel at.

Table 1.1: Details of previous thermal stratification experiments.<sup>6</sup>

| Experiment              | Fluid         | Vertical Spatial Resolution [mm] | Entire length        | Temporal Resolution |
|-------------------------|---------------|----------------------------------|----------------------|---------------------|
| Ieda <sup>21</sup>      | Sodium, Water | 150, 100, 50, 20                 | No                   | Thermocouple        |
| Kimura <sup>22</sup>    | Water         | 20, 5                            | Yes & No, resp.      | Thermocouple        |
| Moriya <sup>28</sup>    | Water         | Traversing Set of 6              | No (Yes thermistors) | Thermocouple        |
| Puustinen <sup>29</sup> | Water, Steam  | None Given                       | No                   | Thermocouple        |
| Tanaka <sup>30</sup>    | Sodium, Water | None Given                       | -                    | Thermocouple        |
| Uotani <sup>31</sup>    | Pb-Bi         | One Traversing Point             | Yes                  | Thermocouple        |
| Vidil <sup>32</sup>     | Sodium        | 100                              | Yes                  | Thermocouple        |

## 1.5 This work

The prime motivation for this work is to understand thermal stratification behavior in the upper plena of liquid metal reactors and use this understanding to improve safety analyses. There is a long history with using liquid metals such as sodium or lead alloys as coolant in fast spectrum nuclear reactors due to their low neutron interaction probabilities, efficient heat transfer due to high thermal conductivity, and low vapor pressure reducing the need for pressurized system<sup>3334</sup>. There have been several design improvements in the last five decades of experience with liquid metal reactors and the advanced reactors proposed for the future include passive safety features. However, the system scale safety analyses of these advanced reactors lack the thorough understanding of thermal stratification and mixing in the reactor plena under transient conditions.

The next step then is to build an experimental system with high resolution velocity and temperature sensors that can capture an array of information in the context of thermally stratified liquid metal plena. The focus of the information capture will be on the flux and gradient quantities in an effort to help estimate quantities important to the transition of stably stratified to mixed convection, where the impact to reactor safety is least understood.

The following chapter, Chapter 2, will focus on the scaling of the problem from reactor to experimental scale. Key parameters ( $Ri$  and  $Pe$ ) will be investigated on their importance in making a scale-scale conversion of the appropriate aspects on the thermal stratification phenomenon. The use of a simulant fluid is explored and the scaling distortion is quantified. With the scale for the experiment dictated by the physical understanding presented, a system is built and described in Chapter 3. The system, the Gallium Thermal-hydraulic Experiment (GaTE), allows for the accurate and reproducible control of important parameters (namely loop flow and temperature). Additional details are provided for the data collection systems, used to quantify the necessary flux and gradient quantities. In Chapter 4 the methodology for the cold step-transient is introduced. It represents a postulated reactor transient important to safety and allows for the distinctive flow regimes to be observed that are needed to parameterize the physical understanding of thermal stratification. Finally, both temperature

and velocity are simultaneously leveraged during cold step-transients to draw a deeper understanding of liquid metal thermal dynamics and how they influence mixing or stratification in [Chapter 5](#).

## Chapter 2

### Scaling the upper plenum

## 2.1 Scaling needs

Previous experiments and analyses have been conducted to understand thermal stratification in upper plena; however, the data collected was limited to sparsely distributed (pitch as low as 5mm but only in certain sections) thermocouple type temperature sensors, with response times slow in their capturing of cold step-transients. To verify the CFD derived models, not only will a finer spatial and temporal temperature resolution be required, but flow velocity will need to be captured as well. Instruments with spatial and temporal resolution small enough to capture small changes in temperature and velocity are specialized and provide their own limits; the primary limit of these devices is temperature. Construction techniques for these high-fidelity instruments provides an upper limit of their use in temperatures of 200°C. Therefore, to gain the advantage of these devices, the choice of fluid in the scaled upper plenum needs to be scrutinized to ensure optimum scaling capabilities.

A scaled facility's upper plenum needs to represent all of the important geometric and fluid characteristics of the model upper plenum while still lending itself to high-fidelity data collection. The plenum and associated system must also be able to recreate the scaled conditions present in a modeled reactor transient, including flow and reactor power output transients. While the model transients of interest are during natural circulation of the core, the separate effects will be de-coupled for a better understanding of thermal stratification separately.

This chapter<sup>1</sup> outlines the design of scaled-down experimental facility for understanding thermal stratification in outlet plena of LMFRs and evaluation of the expected physical behavior in full-scale prototype. This scaling analysis work uses the ABTR as the reference design<sup>1</sup>. The scaled-down experimental setup is designed to be able to construct a range of understanding of this physics, from fully stratified to fully mixed thermal regimes, by using high fidelity instrumentation. A structured approach to scaling is adopted based upon the accepted guidelines and literature.

---

<sup>1</sup>A majority of this chapter is reprinted with permission from “Scaling of thermal stratification or mixing in outlet plena of SFRs” by Ward, Wiley, Wilson and Bindra, 2018. *Annals of Nuclear Energy*, 113, 1, 431–438. 2018 by Elsevier.<sup>2</sup>

## 2.2 Methodology of scaling analysis

The purpose of conducting a scaling analysis on a separate effect, thermal-hydraulic phenomenon is that it must be able to conserve the essential physics in all geometries. The scaling methodology must be able to assess the presence of distortions or their effects on the parameters of interest to a nuclear power plant accident scenario or set of scenarios. The methodology outlined by Zuber et al.<sup>35</sup> is adopted to optimize the similitude by following the hierarchical, two-tiered scaling analysis (H2TS) approach.

The scaling methodology can be summarized into the following steps:

- Specify experimental objectives based upon identified phenomenon, i.e. thermal stratification or mixing in outlet or hot plena.
- Maintain geometric, kinematic, and dynamic similarity between physical processes occurring at full scale and those taking place in a scaled-down test facility.
- Identify the dominant similarity criterion and provide technical justification.
- Evaluate the applicability of models at different scales and assess the distortions.

The first step was described in the introduction chapter, where thermal stratification phenomenon was identified. The rest of this chapter is organized with details on these steps.

## 2.3 Similarity variables and design constraints

The geometric, kinematic and dynamic similarity parameters must be selected and preserved in the scaled model so that the length scales and time scales related to thermal stratification behavior are similar to the ABTR or prototype. Thermal stratification can be effectively characterized by two dimensionless quantities: Richardson number ( $Ri$ ) and Peclet number ( $Pe$ ). Richardson number signifies the ratio of buoyant to inertial forces and quantifies the extent of stratification,  $Ri = g\beta(\Delta T)D/U^2$ . Peclet number signifies the advective to diffusive transport rates and quantifies the thermal dispersion,  $Pe = UD/\kappa$ .

To maintain thermal stratification physics, the scaling needs to be characterized by both  $Re$  and  $Pe$ <sup>36</sup>. This can be shown by non-dimensionalizing the momentum and energy equations. The incompressible Navier-Stokes equation<sup>37</sup> to describe conservation of momentum can then be paired with non-dimensional substitutions for the constitutive variables:

$$\rho_0 \left( \frac{\partial u}{\partial t} + \nabla \cdot (u \times u) \right) = -\nabla P + \nabla \cdot (\mu \nabla u) - \rho g_z \quad (2.1)$$

$$u^+ = \frac{u_i}{U}; t^+ = \frac{tU}{D}; \nabla^+ = D\nabla; P^+ = \frac{P}{g_z D(\rho_h - \rho_0)}; \rho^+ = \frac{\rho_0}{\rho_h - \rho_0}; \theta = \frac{T - T_0}{T_h - T_0} \quad (2.2)$$

inserting the substitutions into the momentum equation and simplifying;

$$\frac{\rho_0 U^2}{D} \left( \frac{\partial u^+}{\partial t^+} + \nabla^+ \cdot (u^+ \times u^+) \right) = \frac{-\nabla^+ P}{D} + \frac{\mu \nabla^{+2} U u^+}{D^2} - \rho^+ (\rho_h - \rho_0) g_z \quad (2.3)$$

$$\frac{\partial u^+}{\partial t^+} + \nabla^+ \cdot (u^+ \times u^+) = \frac{-\nabla^+ P}{\rho_0 U^2} + \frac{\mu}{\rho_0 U D} \nabla^{+2} u^+ - \frac{\rho^+ (\rho_h - \rho_0) g_z D}{\rho_0 U^2} \quad (2.4)$$

$$\frac{\partial u^+}{\partial t^+} + \nabla^+ \cdot (u^+ \times u^+) = \frac{-\nabla^+ P^+ (\rho_h - \rho_0) g_z D}{\rho_0 U^2} + \frac{\mu}{\rho_0 U D} \nabla^{+2} u^+ - \frac{\rho^+ (\rho_h - \rho_0) g_z D}{\rho_0 U^2} \quad (2.5)$$

and finally using the definitions for  $Re$  and  $Ri$  to define the non-dimensional momentum equation.

$$\boxed{\frac{\partial u^+}{\partial t^+} + \nabla^+ \cdot (u^+ \times u^+) = -\mathbf{Ri} \nabla^+ P^+ + \frac{1}{\mathbf{Re}} \frac{\mu}{\mu_0} \nabla^{+2} u^+ + \mathbf{Ri} \rho^+} \quad (2.6)$$

Likewise, the process is extended to the energy equation:

$$\frac{D}{Dt} (\rho C_P T) = \nabla \cdot (k \nabla T) \quad (2.7)$$

$$\frac{\partial T}{\partial t} + u_i \cdot \nabla T - \nabla \cdot (\kappa \nabla T) = 0 \quad (2.8)$$

$$\frac{\partial(\theta(T_h - T_0) + T_0)U}{\partial t^+ D} + \frac{U u^+ \cdot \nabla^+(\theta(T_h - T_0) + T_0)}{D} - \frac{\nabla^+ \cdot \kappa \nabla^+(\theta(T_h - T_0) + T_0)}{D^2} = 0 \quad (2.9)$$

$$\frac{\partial\theta(T_h - T_0)}{\partial t^+} + u^+ \cdot (\nabla^+ \theta(T_h - T - 0) + T_0) - \frac{\kappa}{UD} \nabla^{+2} (\theta(T_h - T_0) + T_0) = 0 \quad (2.10)$$

where the use of  $Pe$  definition allows simplification to the non-dimensionalized energy equation:

$$\boxed{\frac{\partial\theta}{\partial t^+} + u^+ \cdot \nabla^+ \left( \theta + \frac{T_0}{T_h - T_0} \right) - \frac{1}{\mathbf{Pe}} \nabla^{+2} \left( \theta + \frac{T_0}{T_h - T_0} \right) = 0} \quad (2.11)$$

Table 2.1: Parameters of the ABTR used for scaling analysis<sup>1</sup>.

|                                    | Full Flow             | DRACS   |
|------------------------------------|-----------------------|---------|
| Power [MWth]                       | 250                   | 1.88    |
| Coolant temp In/Out [°C]           | 355/510               | 355/510 |
| Flow rate [m <sup>3</sup> /hr]     | 5280                  | 41      |
| Effective flow Diameter, $D_p$ [m] | 1.015                 | 1.015   |
| Flow velocity, $U_p$ [m/s],        | 1.81                  | 0.014   |
| Number of pumps                    | 4                     | N.C.    |
| Number of Heat Exchangers          | 2 IHX                 | 3 DHX   |
| Richardson Number                  | $3.34 \times 10^{-2}$ | 553     |
| Peclet Number                      | $2.77 \times 10^4$    | 215     |

If these bolded quantities are matched ( $Ri$ ,  $Re$  [ $Re = PePr$ ], and  $Pe$ ), the thermal stratification physics can be maintained in the scaled facility. In order to achieve the scaling of the ABTR, the values for  $Ri_p$  and  $Pe_p$  were computed using fluid condition and dimensional data provided in the ABTR Preconceptual Design Report<sup>1</sup>, shown in Table 2.1. These values were required to be identical for the scaled facility to maintain kinematic and dynamic similarity:

$$Ri_p = Ri_m = \frac{g\beta_m(\Delta T_m)D_m}{U_m^2} \quad (2.12)$$

$$Pe_p = Pe_m = \frac{U_m D_m}{\kappa} \quad (2.13)$$

Where,  $U_m$  and  $D_m$  are the mean velocity and characteristic diameter at the entrance of scaled-down model. Given the fluid properties and constant body force, a unique solution ( $U_m, D_m$ ) to the scaled parameters can be found by solving the above algebraic equations:

$$U_m = \sqrt[3]{\frac{Pe_p g \beta_m (\Delta T_m) \kappa}{Ri_p}} \quad (2.14)$$

$$D_m = \frac{Ri_p U_m^2}{g \beta_m (\Delta T_m)} \quad (2.15)$$

The critical dimensions of the plenum which closely impact thermal stratification – ef-

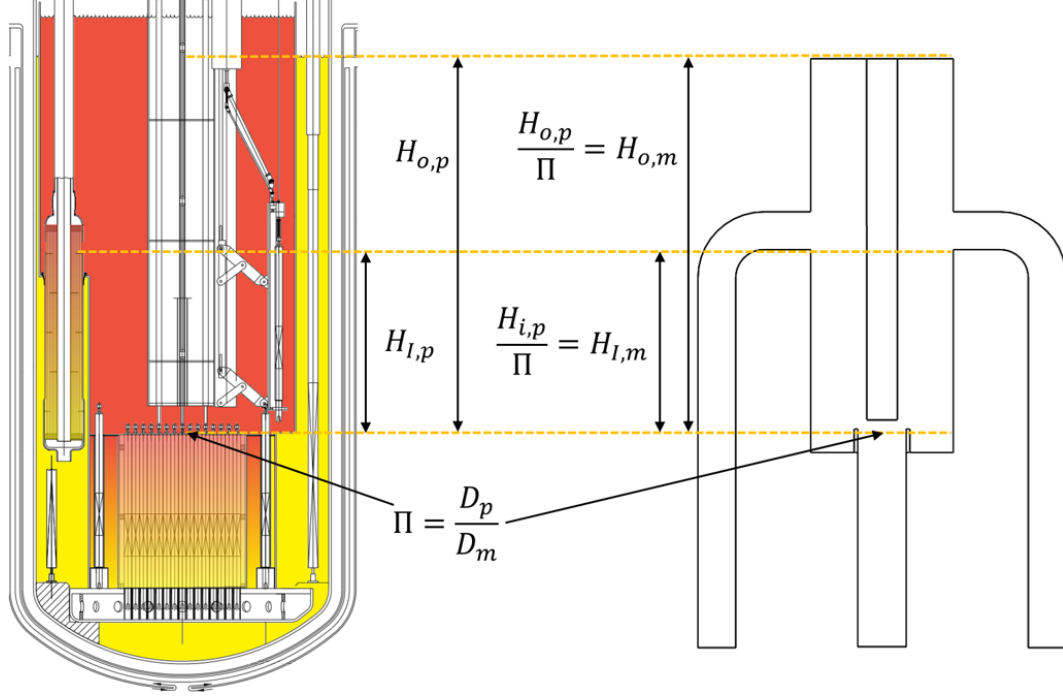


Figure 2.1: Scale to scale representation (Equations 2.18 and 2.19) of the ABTR prototype and model plenum

fective core diameter, height of the liquid pool level from core outlet, and height of the IHX inlet from the core outlet<sup>21;38</sup> – are used to define dimensionless parameters.

$$\Pi_{o,p} = \frac{H_{o,p}}{D_p} \quad (2.16)$$

$$\Pi_{ihx,p} = \frac{H_{ihx,p}}{D_p} \quad (2.17)$$

In order to achieve geometric similarity between scaled model and prototype, following conditions must be met. These are shown in Figure 2.1.

$$\Pi_{o,m} = \Pi_{o,p} \quad (2.18)$$

$$\Pi_{ihx,m} = \Pi_{ihx,p} \quad (2.19)$$

In addition to these scaled dimensions, the UIS diameter and height above the core

barrel exit is also scaled. The heights follows similarly from the above equations; however, the diameter ratio has been chosen such that the physical diameter of the core barrel (not the effective, or hydraulic, diameter) be used in the ratio. This allows a similar flow pattern as seen in the prototype, with the flow area wider than the UIS diameter in both setups.

These relationships are predicated on an identical  $Pr$  (thus solving for  $Re$  as well); however, other constraints for the system design are present, requiring additional consideration and, finally, a quantification of scaling distortion.

### 2.3.1 The other constraints

Additional constraints were also imposed on the design of the scaled-down facility with the following goals in mind: provide a scaled setup that can be easily fabricated, is safe and cost effective, and provides the platform to accurately represent the physics of thermal stratification. These constraints are summarized below.

1. Boundary or wall effects: the shape of the facility will match that of a pool type LMFR hot plenum and be large enough such that thermal boundary interference from the sidewalls will not affect the physics.
2. Temperature limits: the operating temperature needs to be greater than the melting temperature of the fluid and less than the 200°C limit of the flow instrumentation available.
3. Fluid options: an ideal fluid would be a low  $Pr$  liquid metal, similar to sodium but non-reactive with air/water. Toxicity and cost were also constraints imposed in the selection of the fluid.

The numerical values  $(U_m, D_m)$  set for two possible scaled models meeting all of the similarity criteria and constraints are listed in Table 2.2.

As can be seen from the listed values, scaled characteristic length  $(D_m)$  for the two examples are not feasible geometries. Neither would be practicable for a lab environment

Table 2.2: Unique solutions to Equations 2.14 and 2.15 for the fluid properties of the tabulated temperature range.  $D$  characteristic length or effective ABTR core flow diameter.

|                      | Temperature Range [°C] | Fluid   | $D$ [m] | $U$ [m/s] |
|----------------------|------------------------|---------|---------|-----------|
| ABTR                 | 355 to 510             | Sodium  | 1.02    | 0.014     |
| Scaled Sodium Model  | 120 to 200             | Sodium  | 0.83    | 0.017     |
| Scaled Gallium Model | 50 to 200              | Gallium | 0.27    | 0.010     |

where the experimental study of thermal stratification using high fidelity instrumentation would take place.

Previous experiments and studies trying to scale thermal stratification have encountered this conundrum and have chosen  $Ri$  as the primary dimensionless quantity used for scaling<sup>8;21;36</sup>.

### 2.3.2 Design of scaled-down model

With the aforementioned constraints, a fluid was selected along with an optimum geometry of the system. Gallium (melting point  $\sim 30^\circ\text{C}$  and  $Pr \sim 0.025$ ) meets all the requirements stated above and can achieve the  $Ri$  relevant to the prototype ABTR with a model size feasible enough to be built in an academic environment. A 2-D sketch of the GaTE facility, the proposed model for conducting experiments, is shown in Figure 2.2. The inlet, two-outlets, and dimensions of scaled lengths are shown in the figure. The final test vessel design is a 1/20th scale model of the ABTR outlet plenum. The rest of the test loop comprises of three shell and tube heat exchangers (two for cooling - representing the IHX or DRACS - and one for heating - representing the core), and a moving magnet pump with variable frequency drive speed control. The overall system at the above stated temperatures will hold 90kg of liquid gallium.

This facility meets the requirements for geometric, kinematic, and dynamic scaling and those requirements imposed by other constraints by using  $Ri$ ; however, when  $Ri$  alone is used to design the scaled geometry it becomes even more important to evaluate its quantitative impact on the thermal stratification.

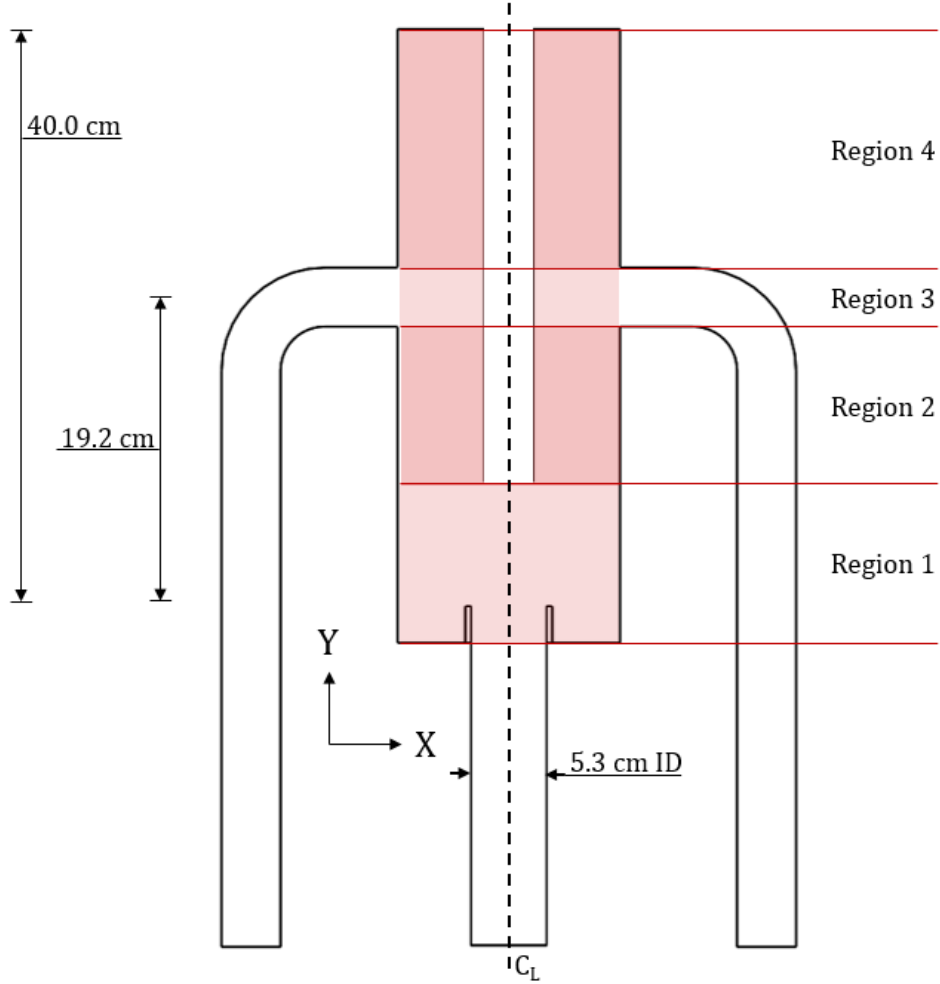


Figure 2.2: 2-D sketch of the GaTE facility with dimensions. Vertical segregation into four regions for analysis.

## 2.4 Evaluation of physics in different scales

Once the scaled design of the model is obtained, it is required to check if it simulates the separate effect physics under consideration with the expected behavior in the prototype. As mentioned before, the objective of this work is to understand the influence of different flow conditions on thermal stratification and mixing behavior in the outlet plenum. The mathematical entity which can directly provide quantitative estimate on the length scales and time scales of the thermal stratification or mixing process in a liquid pool or reservoir, such as outlet plena of LMFRs, is eddy thermal diffusivity. Therefore, relative comparison of eddy thermal diffusivity in the prototype and scaled-down model under test conditions

can provide a reasonable quantification of the scaling effectiveness. Eddy thermal diffusivity is an analogue to molecular diffusivity, which is classically<sup>39</sup> defined analogously to Fick's first law using the turbulent thermal flux ( $\overline{w'T'}$ ):

$$\overline{w'T'} = \kappa_\tau \nabla T \quad (2.20)$$

There are limited closed form models in literature which provide an estimate of eddy thermal diffusivity as a function of fluid mechanics, thermal properties and given thermal constraints<sup>13;40-43</sup>. These models are either developed using high fidelity experimental data, direct numerical simulations, or large eddy simulations, but there are very few detailed studies that can be used to predict this parameter. The particularly relevant model of eddy thermal diffusivity in thermally stratified or mixed large fluid volumes which can be used for the current study was developed by Shih et al<sup>4</sup>. This model provides an empirical relationship between turbulent kinetic energy, buoyancy, fluid properties and eddy or molecular thermal diffusivity. This model determines mixing efficiency with the relative contributions from eddy thermal diffusivity,  $\kappa_\tau$ , and molecular thermal diffusivity,  $\kappa$ . If eddy thermal diffusivity is dominant, then a high level of mixing is anticipated while higher molecular diffusivity implies strong thermal stratification. A normalized parameter  $\hat{\kappa} = (\kappa_\tau + \kappa)/\kappa$  is defined and computed which signifies a quantified measure of mixing efficiency.

The influence of turbulence intensity is captured with the parameter  $Re_\tau = q^2/\nu\varepsilon$ . Where  $q$  is the turbulent kinetic energy,  $\varepsilon$  is the energy dissipation rate, and  $\nu$  is the viscosity of the fluid. The ratio of turbulent Reynolds number to Richardson number,  $\frac{Re_\tau}{Ri}$ , is used here as a model parameter to compute eddy thermal diffusivity and, in turn, mixing efficiency. The empirical model quantifying  $\hat{\kappa}$  as a function of  $\frac{Re_\tau}{Ri}$  is presented in Figure 2.3. The overall the model is divided into three zones: Molecular, Transitional, and Energetic<sup>4;40</sup>.

This empirical model can be used to quantify  $\kappa_\tau$  or  $\hat{\kappa}$  for evaluating thermal stratification or mixing in outlet plena of LMFRs. This requires an estimation for  $Re_\tau$  which is dependent upon  $q$  and  $\varepsilon$ . There are well-established approximations for these parameters which are typically used for initializing Reynolds-averaged Navier-Stokes (RANS)  $k - \varepsilon$  models. For

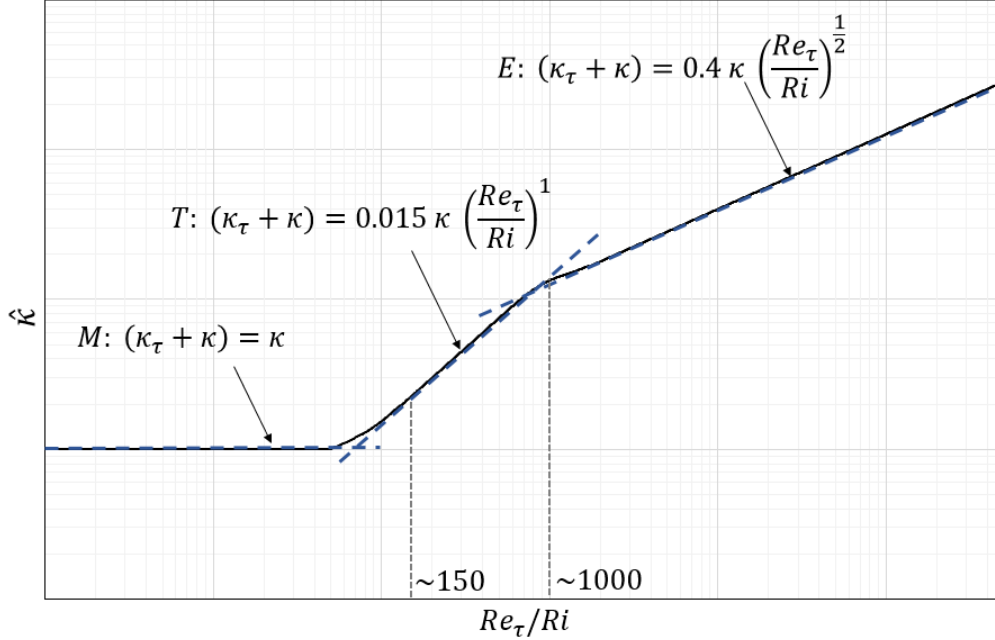


Figure 2.3: Mixing efficiency best fit functions of turbulence intensity for three zones: Molecular (M); Transitional (T); and Energetic (E).

liquid metal (low Prandtl number fluids) flows, the commonly used models<sup>27;44</sup> to estimate these parameters are given by  $q = 0.01U^2$  and  $\varepsilon = \frac{q^{3/2}}{D/2}$  (where  $U$  and  $D$  are the mean velocity and characteristic length described in Section 2.2, resulting in a 5% turbulence intensity ( $I$ ), or  $Re_\tau = IRe$ ). This empirical model is convenient to directly correlate the effect of cold fluid injection flow rates into the hot pool. Verification using more rigorous detailed computations or experimental validation is needed. The next subsection presents detailed computational fluid dynamics (CFD) models used for the verification step.

### 2.4.1 Numerical simulations–Verification

The commercial CFD code ANSYS CFX was used to construct a 3D numerical model of the GaTE facility to simulate the expected experimental physics and to verify the empirical model described earlier. CFX is a multiphysics solver based on the finite volume method. The physics were simulated using simplified boundary conditions with constant inlet flow conditions. The 3D geometry of the model with inlet and outlet is shown in Figure 2.4a, and the meshed geometry is shown in Figure 2.4b. The number of elements in the displayed

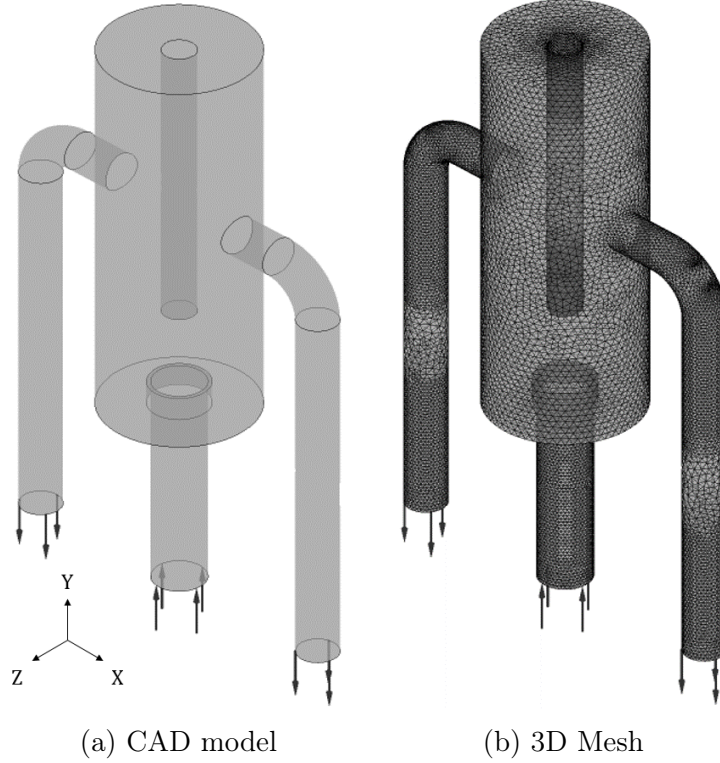


Figure 2.4: Scaled model of the proposed experimental facility.

mesh is 695,504 and the number of nodes is 129,001. It should be noted that this mesh was finalized after grid convergence studies. Steady state flow conditions were initialized with 200°C gallium in the test vessel prior to transient simulations. The inlet condition was then set to gallium entering at a temperature of 50°C. The two outlets shown in the figure were subjected to a constant pressure gradient outflow boundary condition. The top surface (i.e. at the maximum height of the hot pool) is considered to be a free surface and all the remaining surfaces are considered as walls with zero slip boundary conditions. The exit pipe walls have a constant heat flux to remove heat as expected in an actual system with the presence of a heat exchanger.

The CFD code numerically solves coupled partial differential equations, i.e. Navier Stokes equations and energy equation, for the problem domain. The energy equation is simplified to the following form with no-source and no-viscous dissipation assumptions.

$$\frac{D}{Dt}(\rho C_p T) = \nabla \cdot (k \nabla T) \quad (2.21)$$

This energy equation can be rewritten in Einsteinian convention as,

$$\frac{\partial T}{\partial t} = -\frac{\partial}{\partial x_i} \left( u_i T - \kappa \frac{\partial T}{\partial x_i} \right) \quad (2.22)$$

Defining temperature and velocity as the sum of time-smoothed functions and fluctuating functions,

$$T = \bar{T} + T'; u_i = \bar{u}_i + u'_i, \quad (2.23)$$

substituting in the Eqn. 2.22 and time-smoothing leads to

$$\frac{\partial \bar{T}}{\partial t} = -\frac{\partial}{\partial x_i} \left( \bar{u}_i \bar{T} + \overline{u'_i T'} - \kappa \frac{\partial \bar{T}}{\partial x_i} \right). \quad (2.24)$$

Eddy thermal diffusivity is defined as,

$$\overline{u'_i T'} = \kappa_\tau \frac{\partial \bar{T}}{\partial x_i}, \quad (2.25)$$

which leads to a simplified time-smoothed energy equation

$$\frac{\partial \bar{T}}{\partial t} = -\frac{\partial}{\partial x_i} \left( \bar{u}_i \bar{T} + (\kappa_\tau - \kappa) \frac{\partial \bar{T}}{\partial x_i} \right). \quad (2.26)$$

This definition of eddy thermal diffusivity<sup>39</sup> has been widely used in the literature<sup>4;11;13;40</sup> quantified using experimental data or CFD calculations. Here in this work, eddy thermal diffusivity defined in Eqn. 2.25 will be obtained from numerical simulations to verify the empirical model presented in Fig. 2.3.

Numerical simulations were conducted in ANSYS CFX with the following settings. The second order backward euler numerical scheme was used for these simulations. A Multigrid (MG) accelerated Incomplete Lower Upper (ILU) factorization technique is used for solving the discrete system of linearized equations. ANSYS CFX has several options to select laminar and turbulent flow models. The large eddy simulations (LES) were conducted for all cases with wall-adapting local eddy-viscosity (WALE) model. For low flow rate cases, simulation

results obtained using laminar model and LES model are analogous. However, for consistent evaluation of eddy thermal diffusivity from numerical simulations in all cases LES model is used.

## 2.5 Results and discussion

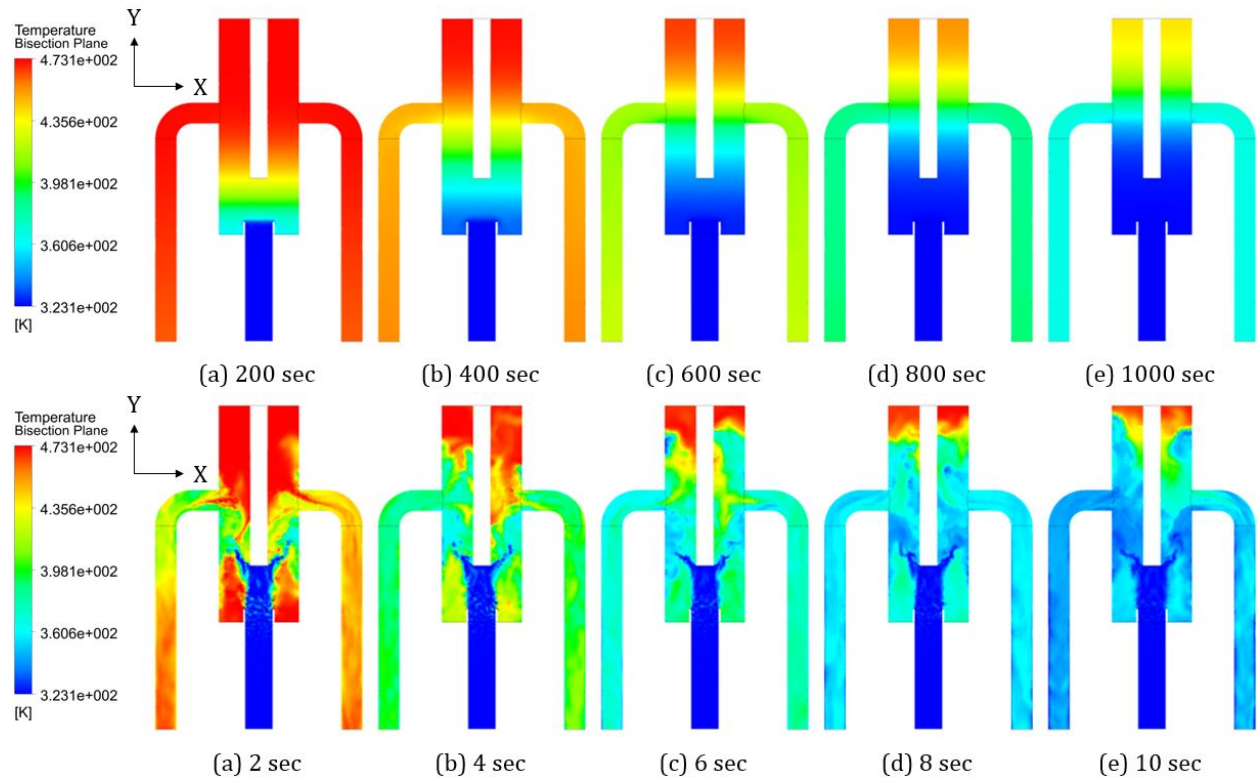


Figure 2.5: Thermally stratified interface progression in the outlet plenum model under varying flow rate colder fluid injection. Effect of different flow injection rates into the upper cavity model: the thermally stratified front has  $Ri=553$  and  $\kappa_{\tau} \ll \kappa$ ; the well mixed profile has  $Ri=0.033$  and  $\kappa_{\tau} > 148\kappa$ .

CFD simulation results are presented in this section, followed by the verification of empirical model for eddy thermal diffusivity and then scaling evaluation. Figure 2.5 shows the transient evolution of the temperature contour plots at the plane passing through center of inlet, outlets and vessel geometry for two inlet flow conditions. The location and dispersion of thermal stratification interface in the hot or outlet plenum is of particular interest for the safety analysis especially under very low flow conditions as mentioned in the introduction.

The simulation results show that, in the case of the low flow rate, the exit serves as an inflection point in the fluid distribution: all momentum diffusion and shear forces effectively cease with the buoyancy of the hot fluid maintaining both its position and temperature above this height (Figure 2.5, top). Low flow simulation results also show that thermal gradients are almost negligible in the radial or azimuthal directions. This is reinforced by Peterson<sup>45</sup> who also studied the extent of mixing and stratification in large enclosures. Under conditions where the ambient medium stratifies, the distribution of mass, energy, and species becomes 1-D<sup>45</sup>. This simplification of the thermally stratified zones into a 1-D model will greatly improve the ability to develop accurate LMFR safety analyses after experimental verification with data generated from this scaled model (GaTE facility). In the high flow case such as shown in Figure 2.5, bottom, the inflection at the exits is less pronounced as the mixing is highly efficient.

Numerical simulations were conducted for 21 separate flow rates with  $Ri$  ranging from 0.033 to 553. For all of these cases, the temperature distribution and vertical velocity distribution were obtained on the plane passing through the center of inlet and outlets. This numerical data is then used to compute eddy thermal diffusivity (Equation 2.25) and, in turn, mixing efficiency.

### 2.5.1 Comparison of empirical and numerical results

Empirical model predictions for mixing efficiency are compared to those obtained from numerical simulations. Figure 2.6 shows separate curves for empirical model under different flow regimes (i.e. Molecular, Transitional and Energetic). Numerically computed values of mixing efficiency averaged over the entire bisection plane are plotted as discrete points for different simulation cases. There is a strong agreement between the predicted mixing efficiency values from empirical model and numerical simulations. As shown in the Figure 2.2, the bisection plane is then divided into 3 different zones based upon their proximity to the inlet or outlet. Numerically predicted values of mixing efficiencies averaged over separate zones are then plotted on the same figure, 2.6. It can be seen that Region 1 and Region

3, due to stronger effects from inlet and outlet, are harder to be predicted from empirical model; whereas, in Region 2 (the central region) mixing efficiency is more predictable.

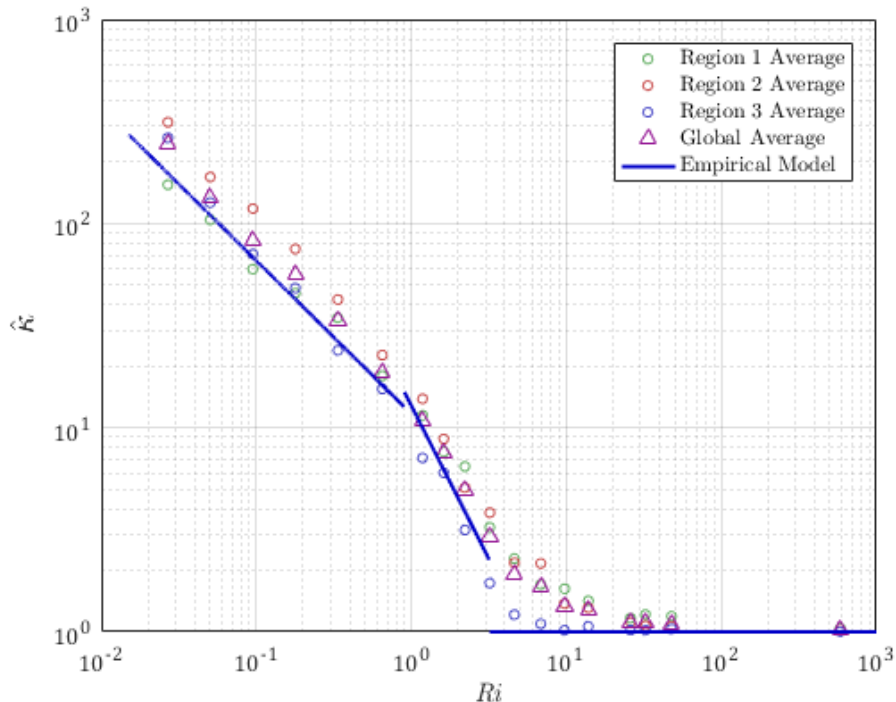


Figure 2.6: Comparison of empirical evaluation of mixing efficiency with that of the numerical evaluation.

This means that either the empirical evaluation or the numerical evaluation may be used to quantify the average thermal mixing efficiency caused by the fluid inertia entering the scaled outlet plenum.

### 2.5.2 Scaling evaluation

The verified empirical model was then used to compute and compare the mixing efficiency for the ABTR and GaTE upper plena for a wide range of flow rates in between the limits of full flow and DRACS flow conditions. The predicted values for these two extreme cases are presented in Table 2.3.

Under low flow conditions, the empirical model shows that for both cases the mixing is negligible as mixing efficiency  $\hat{k}$  is approximately 1. In other words, both scales exhibit

Table 2.3: Average mixing efficiency,  $\hat{\kappa}$ , values for the outlet plenum of prototype ABTR and GaTE facility using the empirical model.

| Richardson Number | ABTR | GaTE |
|-------------------|------|------|
| 0.033 (Full Flow) | 1068 | 149  |
| 1                 | 83   | 13   |
| 553 (DRACS)       | 1    | 1    |

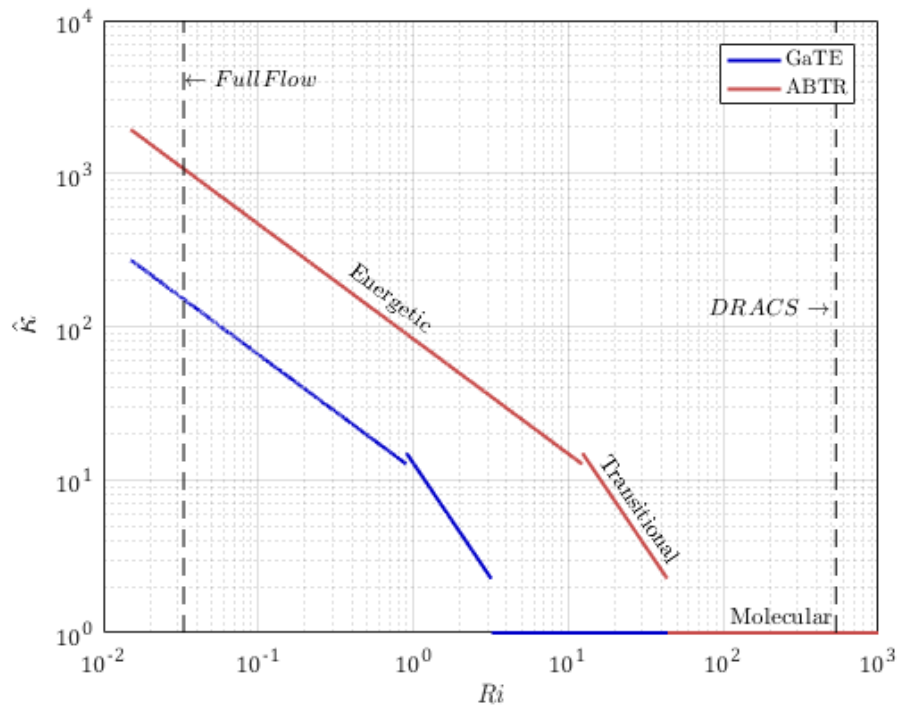


Figure 2.7: Comparison between the ABTR and GaTE; the scaling distortion quantified by the mixing efficiency output.

mixing efficiencies dominated entirely by molecular thermal diffusivity in the low flow or natural circulation flow regime. Therefore, scaling criteria is effectively met for the low flow case.

As the flow rate is further increased resulting into reduction in  $Ri$ , the results from empirical model show that there is expected to be significant differences in the mixing efficiencies in two scales. This trend is observed in both transitional and energetic regimes. For the full flow or normal operation case the mixing efficiency is significantly higher than 1, predicting a well-mixed scenario. At full flow, a well-mixed system assumption can be made for both scales. Therefore, the scaled-down model represents the dominant physical modes in ABTR (prototype) for thermal stratification and mixing under all flow conditions.

## 2.6 Evaluation summary

Thermal stratification of liquid metal in pool type LMFBRs complicates the design of these reactors. Better understanding of thermal stratification behavior is required which can be obtained by developing a scaled-down experimental facility. This work presents the scaling analysis performed to achieve this design and detailed evaluation of the thermal stratification in different scales.

The systematic scaling approach adopted here uses the ABTR as the reference design or prototype. This analysis uses geometric, kinematic, and dynamic similarity along with operating constraints for academic laboratory to achieve a 1/20th scale design of the outlet plenum with gallium as a surrogate fluid. The GaTE facility, the scaled-down model, holds 90kg of gallium and is equipped with high fidelity instrumentation and a moving magnet pump.

Quantitative evaluation of thermal stratification or mixing in scaled-down model or prototype was performed with the help of eddy thermal diffusivity or mixing efficiency. Due to their generic definitions these quantities allow their applicability to all geometries.

An empirical model of mixing efficiency, the normalized contributions of both eddy thermal diffusivity,  $\kappa_T$ , and molecular diffusivity,  $\kappa$ , as a function of turbulent kinetic energy,

buoyancy, and fluid properties, has been validated by CFD simulations using ANSYS CFX. There is strong agreement between the predicted mixing efficiency values from the empirical model and numerical simulations.

The empirical model has provided evidence that both the low flow and high flow cases for both the prototype and model exhibit mixing efficiencies representative of their respective dominant physical modes. In the case of low flows expected during natural circulation, the thermal stratification front is pronounced as the mixing efficiency of the system is dominated by molecular thermal diffusivity. In contrast, in the high, full flow case, eddy thermal diffusivity dominates and the system is well mixed.

The evaluation has shown that the scaled-down model accurately represents the dominant physical modes in the ABTR (prototype) for thermal stratification and mixing under all flow conditions. This will enable the scaled-down model to serve as a successfully scaled platform and allow the accurate understanding of the relevant physics to be obtained and applied to future LMFR designs. In the next chapter, how the scaled-down model is used, what instrumentation is deployed, and the limitations of both are presented.

## Chapter 3

# The Gallium Thermal-hydraulic Experiment (GaTE) facility

## 3.1 GaTE system features

The GaTE system is equipped to allow for exploration of the conditions that lead to thermal stratification interface fluctuations in the scaled upper plenum. Manipulation of ‘core’ exit (or plenum inlet) barrel temperature and velocities, both key variables in the  $Ri$ , is accomplished using the GaTE system features (shown in Figure 3.1).

### 3.1.1 System flow control and measurement

A moving magnet pump controls flow conditions throughout the loop by changing its rotational speed<sup>46;47</sup> (governed by a variable frequency drive with proximity probe speed feedback - characteristic details can be found in Appendix A). This output is measured by an electromagnetic flow meter (EMFM). The EMFM is a custom-built velocity-sensing element: it is a transverse field flow meter where fluid velocity, external magnetic field, and induced voltage are all mutually orthogonal<sup>48</sup>. The induced voltage at an attached set of electrodes is proportional to the fluid velocity<sup>49</sup>. Calibration was completed in-house using a custom calibration cylinder - details are provided in Appendix B. The calibration uncertainty between the expected voltage signal and the measured voltage is less than 5% across a range of flow rates.

### 3.1.2 System temperature control and measurement

Heat exchangers are used to control the loop temperature. The representative ‘core’ and intermediate heat exchangers (‘IHXs’) are of tube and shell construction with gallium present in the tube side for both sets. An oil circulation heater regulates Therminol HTF temperature in the ‘core’ shell side while in the ‘IHX’ shell-side, water maintains the remainder of the loop at 50°C - clamp on thermocouples (response time  $\approx$  12s) monitor this.

The final sensing element for ensuring reliable plenum inlet boundary conditions is the temperature probe placed 1.33 diameters below the inlet to the scaled plenum. A factory calibrated, K-type, 1/16" diameter thermocouple with a published response time of 300ms

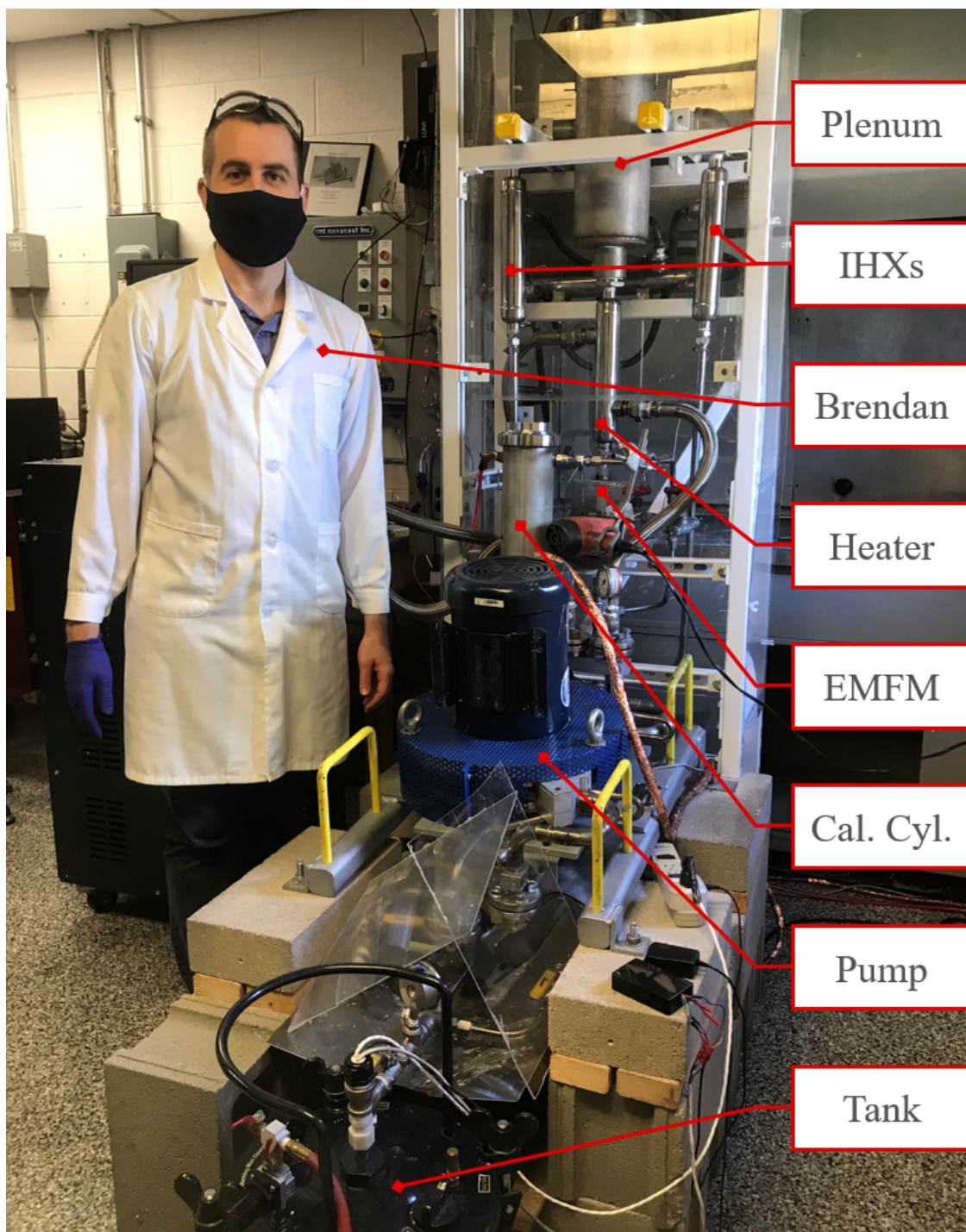


Figure 3.1: The GaTE system. Top: scaled upper plenum directly connected to three heat exchangers (2x side coolers; 1x bottom heater). Left (behind the Brendan): wall mounted VFD control panel and oil circulation heater connected by hose to the bottom heater. Bottom: moving magnet pump above the liquid storage tank.

is installed such that the sensing element is in the center of the fluid path. Steady state values were used as reference for the calibration of the plenum temperature array (section 3.3) and the transient data collected provided determination of the global  $Ri$ . The location of the probe is also shown in Figure 3.2, next to the other important plenum features.

## 3.2 GaTE plenum features

The GaTE plenum resembles, as close as possible, that of a typical LMFR upper plenum. The UIS, a hollow pipe in the GaTE, is included and scaled. The height above the core outlet is scaled similarly (ratio as in Eq. 2.18) but diameter is scaled not by hydraulic diameter of the core but the actual geometry. This leaves the UIS diameter smaller than the core exit barrel in both the prototype and model systems. Additionally, a 25.4mm basin below the plenum inlet is used to help emulate the same backwards step condition present in the prototype (see again Figure 1.1).

Beyond this, the plenum houses the distributed sensing arrays for temperature and velocity, the SWI-DTS (Section 3.3) and UDV (Section 3.4) of Figure 3.3. They are installed on a rotatable instrumentation support structure; the azimuthal location of the sensors, unless specified otherwise, is orthogonal to the exit channel plane. The following sections describe these sensor types and their limitations of use with sample data; however, this data is meant to be descriptive in nature with Chapters 4 and 5 providing more in depth understanding of the physics using the SWI-DTS, UDV, and both, respectively.

## 3.3 Distributed temperature sensing

### 3.3.1 Recent advancements

High-speed distributed sensing temperature measurement system with optical-fiber based sensors has been used previously to study temperature mixing<sup>50;51</sup>. The fibers offer sensing at very high pitch and data collection rates with a single sensor, offering up a far less complex

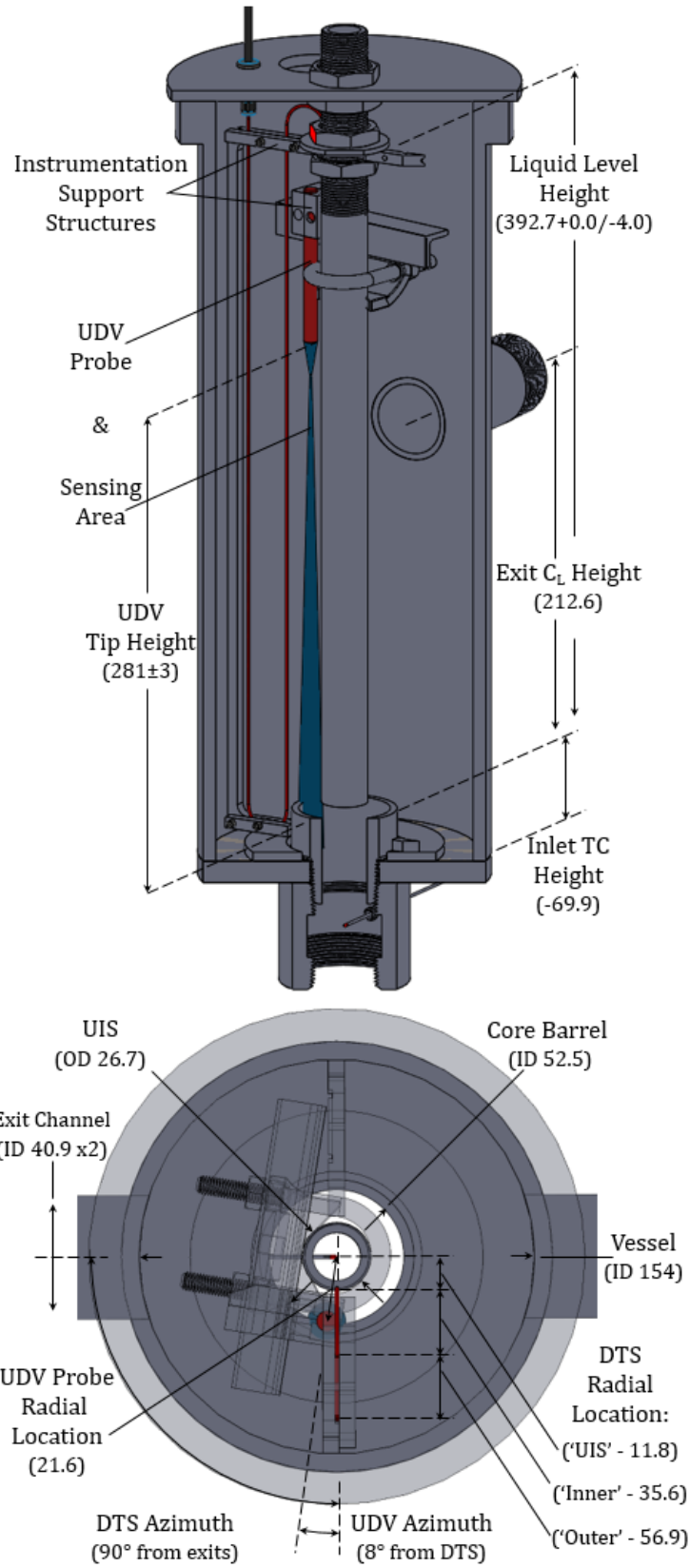


Figure 3.2: GaTE plenum geometry and key component dimensions and locations.

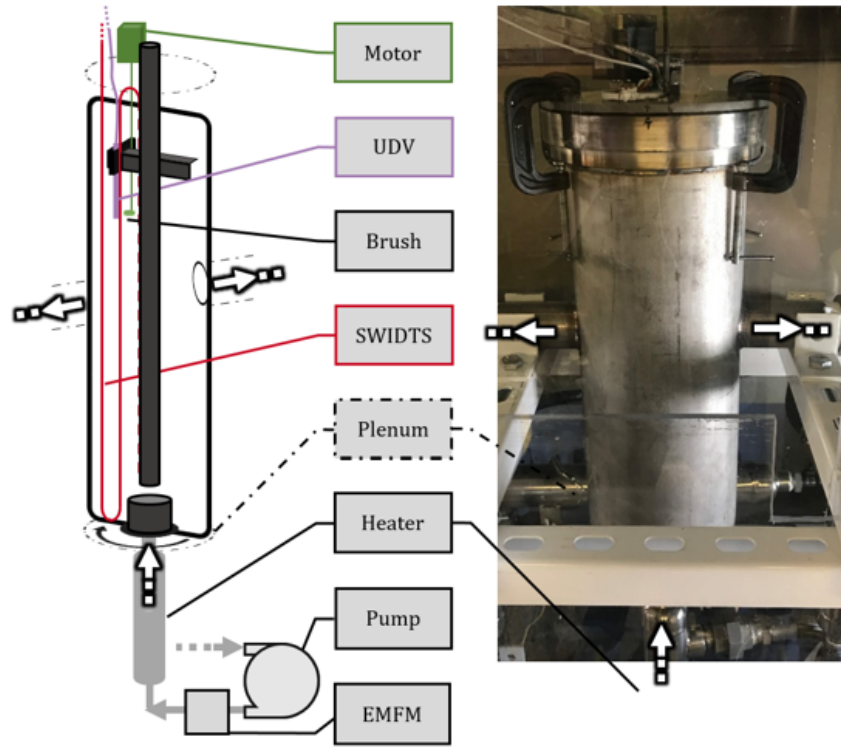


Figure 3.3: GaTE instrumentation platform and system components.

array than could be handled by hundreds of thermocouples. These advancements are key, as they aid in the determination of turbulence mixing quantities  $T'$  and  $\partial T/\partial z$ . A comparison of past experimental work involving temperature measurement in thermally stratified plena is provided in Table 3.1 filled in with recent studies, two of which use the sensors. These two systems have the lowest pitch to height ratio and can achieve complete axial coverage.

### 3.3.2 DTS working principles

The swept wavelength coherent interferometry distributed temperature sensor (SWI-DTS) system is able to interpret measurement distributed along its entire probe path, i.e. the entire axial length, as stated above. This allows for novel measurements using Rayleigh back-scattering principles with predictable fiber responses due to changes in temperature. The SWI-DTS is installed in a three-segment (multiple radial location) manner down the entire length of the plenum. Two of the three segments are completely surrounded by fluid

Table 3.1: Details of previous and ongoing thermal stratification experiments.

| Experiment (Year)              | Fluid          | Vertical Spatial Resolution [mm] & Pitch/Plenum Height | Entire length           | Temporal Resolution |
|--------------------------------|----------------|--|-------------------------|---------------------|
| Ieda <sup>21</sup> (1990)      | Sodium, Water  | 150, 100, 50, 20<br>$\geq 0.0133$                      | No                      | Thermocouple        |
| Kimura <sup>22</sup> (2012)    | Water          | 20, 5<br>$\geq 0.0068$                                 | Yes & No, resp.         | Thermocouple        |
| Moriya <sup>28</sup> (1987)    | Water          | Traversing Set of 6                                    | No<br>(Yes thermistors) | Thermocouple        |
| Puustinen <sup>29</sup> (2008) | Water, Steam   | None Given   | No                      | Thermocouple        |
| Tanaka <sup>30</sup> (1990)    | Sodium, Water  | None Given   | -                       | Thermocouple        |
| Uotani <sup>31</sup> (1986)    | Pb-Bi          | One Traversing Point                                   | Yes                     | Thermocouple        |
| Vidil <sup>32</sup> (1998)     | Sodium         | 100<br>0.0313  | Yes                     | Thermocouple        |
| E-SCAPE <sup>52</sup> (2020)   | Pb-Bi          | None Given   | Yes                     | Thermocouple        |
| TSTF <sup>53</sup> (2020)      | Sodium         | 2.67<br>0.0021   | Yes                     | SWI-DTS             |
| <b>GaTE</b> (2020)             | <b>Gallium</b> | <b>2.6</b><br><b>0.0065</b>                            | <b>Yes</b>              | <b>SWI-DTS</b>      |

while the third segment is encompassed by an open trench within the UIS. The respective radial locations of the ‘UIS’, ‘inner’, and ‘outer’ segments are 11.75mm, 35.56mm, and 56.90mm (out of a total 77.03mm radius). The support structure that holds the SWI-DTS sensor is symmetric and can be rotated between experimental tests, as necessary. This multi-segment style of SWI-DTS sensor, as seen in other thermal fluid experiments, allows sampling of a plane along the entire length of the vessel. The current configuration, shown in Figure 3.2, has a vertical pitch of 2.6mm and a collection rate of 22Hz. The SWI-DTS allows the gathering of temperature field information necessary to conceptualize behavior of the thermal stratification interface.

The principle of operation is based on optical frequency domain reflectometry, and any localized strain in the optical fiber due to temperature change is detected by a shift in

optical frequency of the Rayleigh backscattered signal. The system has been assembled and calibrated before its installation in the GaTE plenum. The inlet thermocouple is used to tare the SWI-DTS response (the strain is based on difference measurements, not absolute temperature). Coupled with the calibration of the thermocouple and the deviation associated with random fluctuations of the measurement (noise), the total uncertainty of the system is  $\pm 1.8^\circ\text{C}$ . Besides comparison to other devices, the IHX shell side begins to boil when the system steady state temperature reaches  $100^\circ\text{C}$ . The system in the GaTE uses a stainless steel sheath for increased rigidity and resistance to flow strain (this comes at a cost: some thermal damping is expected with the 1/64 inch thick stainless steel sheath so the actual recording rate is reduced from the 250Hz maximum). Isothermal use of the SWI-DTS shows no increase in deviation associated with temperature measurement even at the highest flow rate possible in the GaTE. How all this can be used to interpret plenum dynamics is described next.

### 3.3.3 Information from the SWI-DTS

As a demonstration case to exhibit some of the uniqueness of the SWI-DTS, an unprotected loss of flow (ULOF) test is shown in Figure 3.4. The plenum temperature is raised to a steady-state  $100^\circ\text{C}$  at nearly 30mm/s. At  $t = 0$  the pump is tripped and the temperature difference between the hot (plenum) and cold legs begins to drive the flow through the system. After 6.5 minutes the heater is tripped and the evolution of the temperature front exiting the ‘core’ progresses, slowly lowering the effectiveness of the natural circulation.

For reference, the SWI-DTS contour represents 24,938 time steps by 149 axial points. What is shown is the UIS pass, the inner-most pass of three, to capture the thermal plumes (that rise mostly straight up, hugging the UIS). The other DTS passes (not shown) contain 170 points each. Overlaid in black on the figure are isotherms. Prior to the trip, convective currents mix the temperature rapidly, raising it from the steady state temperature to almost  $150^\circ\text{C}$ . After the trip, there is some cooling of the whole plenum over the course of the next 10 minutes but most of the cooling occurs at the bottom, where the thermally stratified cold

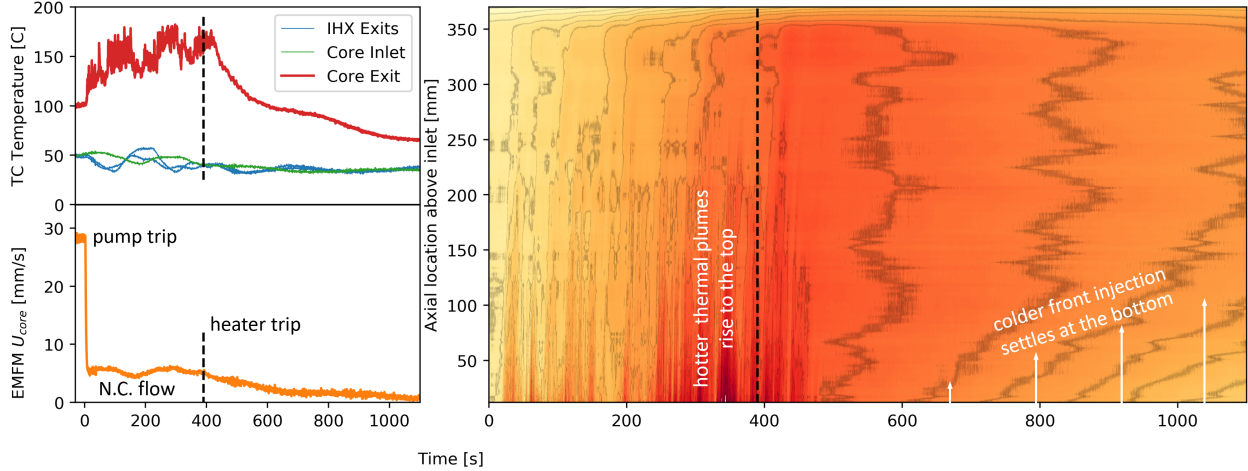


Figure 3.4: Loss of flow test without heater trip - steady state natural circulation (N.C.) develops. With a heater trip, the temperature profile in the hot leg (plenum) progresses, lowering the natural circulation force. Left: system instrumentation; right: SWI-DTS information from the UIS pass (most central).

front is entering. While interesting, this is not the complete picture. The velocity must also be captured and understood; in the next section is how the GaTE system takes distributed velocity data.

## 3.4 Ultrasonic Doppler Velocimetry (UDV)<sup>1</sup>

### 3.4.1 UDV working principles

The UDV system (UDOP4000 - Signal Processing<sup>55</sup>) works on principles of acoustic backscattering, similar to sound navigation and ranging (SONAR), where an ultrasonic pulse is transmitted into the fluid and, as the backscattered signal is returned, the time-of-flight corresponds to the scattering media's position from the probe. For pulsed UDV, this process is repeated continuously such that the position can be tracked in time, leading to velocity measurements along the entire line-of-'sight' of the probe (as seen in Figure 3.2). Depending on the position and velocity of the scattering media, interaction with the pulse will be

<sup>1</sup>A majority of this section is reprinted with permission from "Experimental measurement of liquid metal flow fields in a scaled SFR upper plenum" by Ward, Sieh, and Bindra, 2019. 18th International Topical Meeting on Nuclear Reactor Thermal Hydraulics (NURETH-18). 2019 by American Nuclear Society.<sup>54</sup>

phase shifted by frequency  $f_d$ , the Doppler frequency, from a previous pulse. (It should be noted that the repetition frequency of the pulse cycle is shifted and not the frequency of the emission as in in laser Doppler velocimetry.) The relation to velocity,  $u$ , is a function of this Doppler frequency, the speed of sound,  $c$ , the pulse emission frequency,  $f_e$ , and the angle off parallel from the pulse path,  $\theta$ :  $u = \frac{f_d c}{2f_e \cos(\theta)}$ .

Since the software for determining the velocity based on acquired backscattered signals requires a high degree of correlation between pulses, backscatter media must be adequately echogenic. The degree to which a pulse is reflected or transmitted into a medium is described by its acoustic impedance mismatch with the fluid. A large enough impedance mismatch must be present between the fluid and scattering media in order to obtain a strong signal. For gallium, naturally occurring oxides are echogenic and conveniently meet requirements for use as a seed particle (see Section 3.4.2). However, as other researchers have noted<sup>56–58</sup>, the presence of this oxide can make UDV measurement more difficult.

### 3.4.2 Gallium oxide

Due to its impedance mismatch with gallium metal, gallium oxide is a good candidate for acoustic backscattering techniques in liquid gallium. Its use as a seeding particle requires a specific gravity near that of the liquid. Brito<sup>56;59</sup> has identified the two main oxides:  $\text{GaO}_2$  and  $\text{Ga}_2\text{O}_4$  with specific gravities of 4.77 and 6.44.  $\text{ZrB}_2$  (SG = 6.17) has been used previously, a closer match to the 6.08 specific gravity of the 50°C gallium but would require a greater degree of complexity for extended operation in the GaTE. The oxides' melting points are well above the limits of the probe and will not be impacted by any changes in system temperature. Finally, the size of the particles must be considered since the wavelength of the UDV emission pulse must be greater than the size of the particles. With smaller particles, the acoustic wave is scattered (some backward as echoes and some forward to continue propagation) leaving the main wave mostly unattenuated. If the particles are greater than the wavelength then the process of reflection and refraction is dominant and can greatly attenuate the ultrasonic signal and alter its course. Even though the size and shape of the

oxide particles are not known, through testing and observation of a mostly unattenuated echogram, the use of gallium's oxides for seed particles is mostly successful - with one main exception.

It is the oxides' acoustic impedance, coupled with its affinity to adhere to solid surfaces, that makes UDV measurement with their presence difficult. After an extended period, the oxide begins to form a layer on surfaces (including the probe tip or wall/waveguide interface). As a pulse is transmitted from the probe and into the oxide layer building along the probe, there is an immediate reflectance of nearly all of the pulse signal. The layer buildup period is a function of oxide production rate, flow around the surface, and surface characteristics. Cleaning and suppression of oxide formation is an accepted approach to handling this issue. While other research has focused on reducing oxide production rate<sup>56;57</sup>, due to the size, complexity, and temperature of the GaTE during data collection, this becomes impractical. The most common technique for oxide suppression is to use a solution of 10% HCl in ethanol on the top surface of the gallium. With ethanol's boiling point below operational temperatures of the GaTE, its use as a buffer layer is not a feasible option. The most effective means of removing the impact of a gallium oxide layer on the probe interface was found to be mechanical removal of the oxide layer on the probe interface. Since the period of buildup (prior to velocimetry accuracy degradation) is on the order of tens of minutes with data collection on the order of seconds, the solution employed enables the taking of velocimetry snapshots between removal cycles. A silicone wiper is located near the probe tip - able to mechanically remove oxide accumulation.

### **Oxide concentration and signal to noise ratio**

With the wiper handling the impact of oxides on the immediate reflectance of UDV signal of surface bound particles, the consideration turns to in-fluid oxides. Over the course of hours, particle concentration can change as settling occurs. This does not impact the interpretation of the velocity of moving backscatter media, but it does impact the signal to noise ratio.

The spectral response of the measured echo consists of a peak at the emission frequency

with subsequent modes present as functions of the pulse repetition frequency (PRF), emission burst length frequency, and the frequency shifts created by particle movement. However, the shifts created by particle movement are complex and require a high degree of correlation to exist between pulses - this is where electro-magnetic interference (EMI) can produce spurious velocity signals. If the oxide concentration becomes too low the correlation between pulses due to particle movement can be masked by EMI signals.

The largest source of EMI for the GaTE is the pump motor-VFD (variable frequency drive) cable. The VFD modulates the frequency sent to the 4-pole induction motor - at 60 Hz the motor will spin (nominally) at 1800RPM; at 30 Hz, 900RPM; etc. - allowing control over a wide range of pump flow rates. However, the VFD output at any frequency other than grid 60 Hz is not a clean sine wave and is instead composed of smaller spikes in output composed to represent a slower power frequency. It is these spikes that generate broad-spectrum<sup>60</sup>, high frequency noise. While mitigation strategies have reduced the power of EMI produced by the cable, some leakage still exists and can impact low oxide concentration velocity distributions.

The process of initialization and startup of the system is able to stir up an ample supply of oxide for UDV use. Monitoring of the echograms and limiting the time from startup ensures that the data captured for use is the velocity component of the signal, not the EMI. The experimental process, from start up through the completion of the longest transient of relevance to reactor safety, lasts tens of minutes - well within the hours it takes for signal to noise ratio to have an impact on measurement interpretation. In addition to these steps, parameters of the UDV system can be modified to handle EMI better.

### 3.4.3 Data collection parameters

Of the parameters able to be manipulated on the UDOP system, the four most important for capturing consistent velocity distributions in the presence of EMI are: PRF and emissions/profile (temporal resolution), the resolution (axial pitch), and emitting power.

The pulse repetition frequency (and its inverse,  $T_{PRF}$ ) dictates the timing of the pulses

and therefore both the maximum velocity that can be interpreted as well as the change in velocity with time. To avoid aliasing of the signal and its interpretation, the maximum velocity is defined by  $u_{max} = \frac{c}{4f_e \cos(\theta) T_{PRF}}$ .

A  $T_{PRF}$  of  $800\mu s$  was used in these experiments (corresponding to a  $u_{max}$  of  $223\text{mm/s}$ ) to ensure the entire range of flows present are captured. Any smaller, and slower flows will start to be interpreted as stationary; any larger, and the faster flows cannot be captured.

Coupled with the PRF is the number of emissions/profile in the determination of temporal resolution. Data for an individual profile is collected across multiple ultrasonic emissions. If the number of emissions/profile is large, the variance can be reduced as correlation between the emissions can be averaged; however, if the number of emissions/profile is too large, then there is a loss of temporal resolution. To try and capture profiles that are representative of turbulent flows, a faster (fewer emissions/profile) setting was chosen. At  $800\mu s$  and 50 emissions per profile, the temporal resolution is up to  $25\text{Hz}$ . However, due to delays in electronics, the recording rate with these parameters is  $18.8\text{Hz}$ .

The resolution, or pitch, governs the spacing between axial sampling volumes along the pulse path. However, it does not control the length of the sampling volumes themselves. This is a function of the wavelength of the fluid and pulse length which are hardware settings. For the  $4\text{MHz}$  probes used and the DOP4000 system in gallium, the length of the sampling volumes will be  $1.4\text{mm}$  in length. Any resolution below this can capture the entire axial profile with partially overlapping sampling volumes. However, profiles for resolutions lower than one-half millimeter do not provide a long enough depth of field,  $P_{max}$ , for the PRF chosen and the limitations of the hardware (number of individual spatial points cannot exceed 1000):  $P_{max} = \frac{cT_{PRF}}{2}$ . Therefore, resolutions of one-half and one millimeters were tested. The time averaged velocity distributions were the same but the one millimeter resolution showed to be less susceptible to EMI when experiments were carried out long enough for oxide concentration to begin to drop.

The last parameter set in order to help lower the impact of EMI is the emission power. The DOP4000 has three power settings: low, medium, and high ::  $10, 30, \text{ and } 60 V_{pp}$ , respectively. Solid structures can impact the interpretation of the flow at high power emissions

(strong echo signals resulting in 0 velocity at phase shifted ‘depth’) - the trade-off is a lower signal to noise ratio. To maximize the signal to noise ratio, the ‘high’ setting was used for the tests. This results in a few artifacts of peculiar velocity, but they are easily identifiable and do not impact the interpretation of the flow field. With the settings inputted, tests were conducted to verify instrument velocity.

#### 3.4.4 Verification of the UDV probe in the GaTE

Tests of the probe under controlled conditions with the previously described settings were conducted to ensure that velocity magnitudes would be appropriate for use after installation within the GaTE. Consistent, calibrated flows to test the probe against would require a calibration standard, generally accomplished by another flow velocity instrument. However, these standards are hard to come by for gallium. Instead, a device to generate the velocity with easily measurable metrics, is used. Since the velocity computed by the UDOP does not distinguish between probe motion or backscatter motion, the choice was made to move the probe in a pool of stationary gallium. An axial stage was temporarily installed which was able to move the probe up and down within the gallium in a controlled fashion, again using a stepper motor and gear system with known outputs.

Recordings were made for two speeds both in and out of the pool and are reported in Figure 3.5. The highest error between the stage velocity and recorded mean was observed for the slower speed and was just under 5%. The error dropped significantly when the stage was sped up - down to below 1% for either direction. Standard deviations were similar for all four cases at 2.5mm/s.

Tests were also conducted at elevated temperatures during verification. During these tests, an increase of error of 1.1% across all test speeds was observed without accounting for temperature dependence of the speed of sound. Since the speed of sound,  $c$ , is a computational constant used to interpret velocity in the UDOP, the correct value must be inputted. Updated values for  $c$  were obtained from the relationship in<sup>57</sup> with a difference of 1.05% between temperatures. After accounting for the temperature variation in  $c$ , the error returned

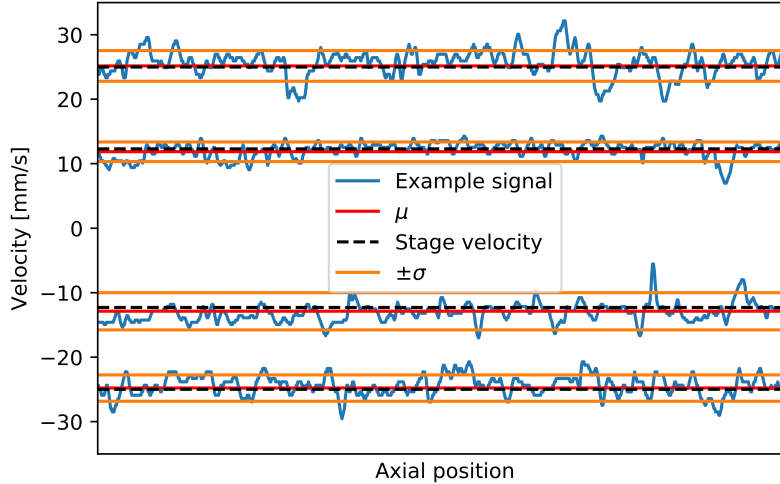


Figure 3.5: Verification of UDV snapshot (blue), including mean (red) and  $\pm$  one standard deviation (orange), to axial stage velocities (dashed black).

to within the bounds already reported. For the tests conducted, as described in the next section, the temperature of the entire plenum is held at a constant value.

## Reproducibility

Additional checks were made to test the day to day or test to test reproducibility of the measured signal. For this, isothermal tests (as described in Appendix F<sup>61</sup>) were conducted with long-duration data captures (6000 time steps at 18.8Hz). Balancing the need to wipe oxide accumulation with the desire to have as many time steps as possible for data analysis, the roughly 5 minute window was chosen. Convergence of the cumulative mean was verified at this time window for all characteristic inlet velocities,  $U$ .

Two characteristic velocities were chosen:  $U = 40$  and  $60$  mm/s ( $Re = 7700, 10,600$ ). These cases represent the mid-upper range of flow rates and important  $Re$ s with a  $50^\circ\text{C}$  temperature delta. To ensure reproducibility of the tests, 3 and 9 (respective) replicates for each  $U$  were collected. Their 6000 point converged means are shown in Figure 3.6. The median of the replicates for each test is shown as a black line through each axial location; the inter-quartile range (IQR) and maximum-minimum range are shown in dark and light fills, respectively. Much closer agreement between replicates can be seen for the 40mm/s case;

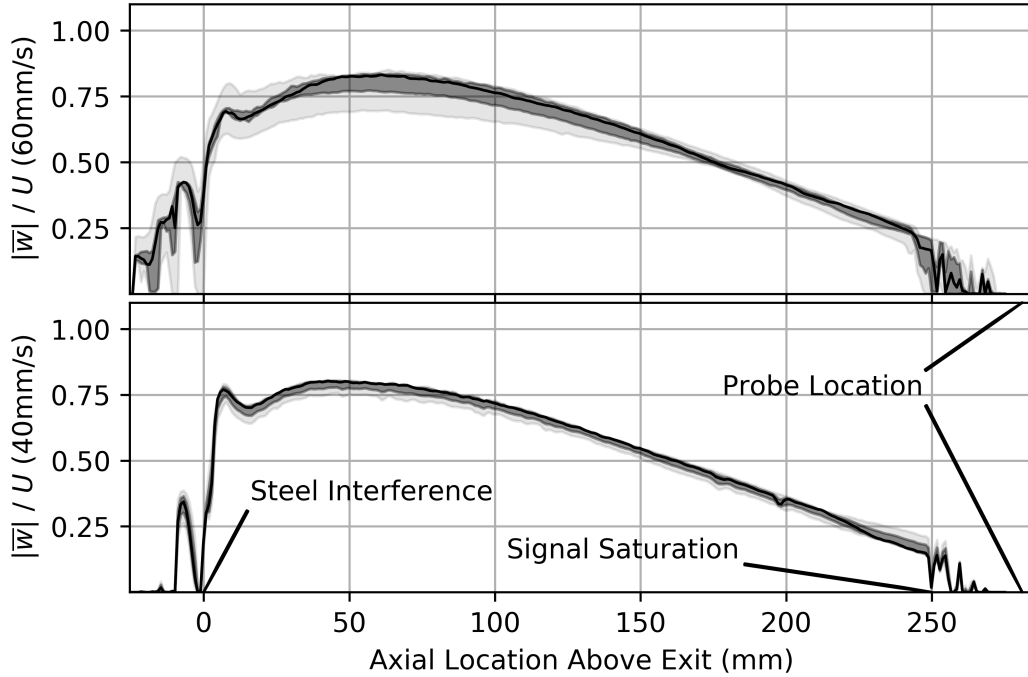


Figure 3.6: Converged means of  $U = 40$  and  $60\text{mm/s}$  ( $Re = 7700, 10, 600$ ). Solid black lines are the medians of the respective replicates (3 for  $40\text{mm/s}$  and 9 for  $60\text{mm/s}$ ); dark fill is the IQR; and light fill shows maximum-minimum range.

increased intermittency of the turbulent flow at the higher  $Re$  creates the deviation seen even at 6000 time steps. To show the dynamics of the systems and highlight this intermittency, Figure 3.7 is included. This figure shows the velocity difference ( $\delta w' = w'(z) - w'(z + r)$  - where  $r$  is an arbitrary distance away, here only one axial node) normalized by the root mean square of the deviation. Good agreement is shown out to  $10^{-2}$  probability density for all cases and locations. Near the inlet the low probability tails, especially in the  $60\text{mm/s}$  case, show the intermittency previously mentioned.

### 3.4.5 Information from the UDV system

Despite the efforts described above in reducing the noise of the system, there is still a limited time to capture clean UDV data (even less when the probe temperature is near  $100^\circ\text{C}$ ). So to demonstrate the capabilities of the UDV system in the GaTE with clean data, cold, isothermal tests were performed. Shown in Figure 3.8 are contours (axial location by time) of

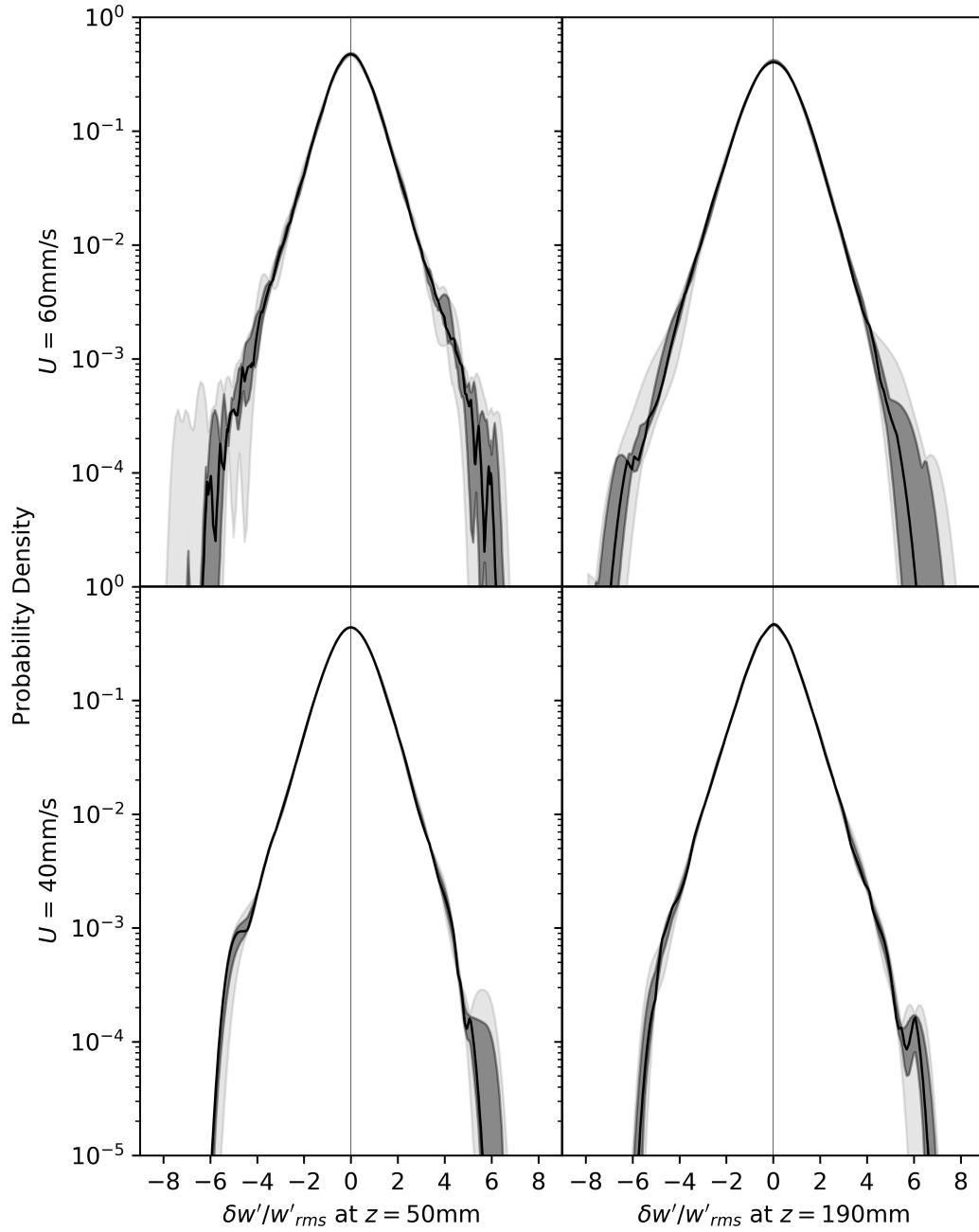


Figure 3.7: Statistics of dynamic contributions of the velocity differences of  $U = 40$  and  $60 \text{ mm/s}$  ( $Re = 7700, 10, 600$ ). Solid black lines are the medians of the respective replicates (3 for  $40 \text{ mm/s}$  and 9 for  $60 \text{ mm/s}$ ); dark fill is the IQR; and light fill shows maximum-minimum range.

three characteristic inlet velocities:  $U = 20, 40,$  and  $60\text{mm/s}$  ( $Re = 3500, 7700, 10,600$ ). All of these tests were despiked, a process for reducing the noise content of the signal using post processing - it is described in more detail in Appendix C. Interesting dynamics at different locations are observable. For example, the flow of large eddies is strong through the bottom of the plenum and tapers off in route to the exit channel height (shown in dashed black lines). The observed vertical velocity shows recirculation at the exits, sometimes pushing flow down for short periods of time. In all cases, the impact of solid structures can be seen at the bottom, where the UDV sensing area intersects the core barrel. Similarly, the over saturation of the initial pulse near the probe reduces the usable sensing area.

Even with these constraints, the system can measure the turbulent flux parameters of interest ( $w', \partial\bar{w}/\partial z$ ). Coupled with the SWI-DTS and control of the plenum parameters, the understanding of thermal stratification in liquid metal plena is possible. In the following chapters more data and finer detail will be provided to show the capabilities of the GaTE instrumentation and how they can be used to determine important information on the measured phenomena.

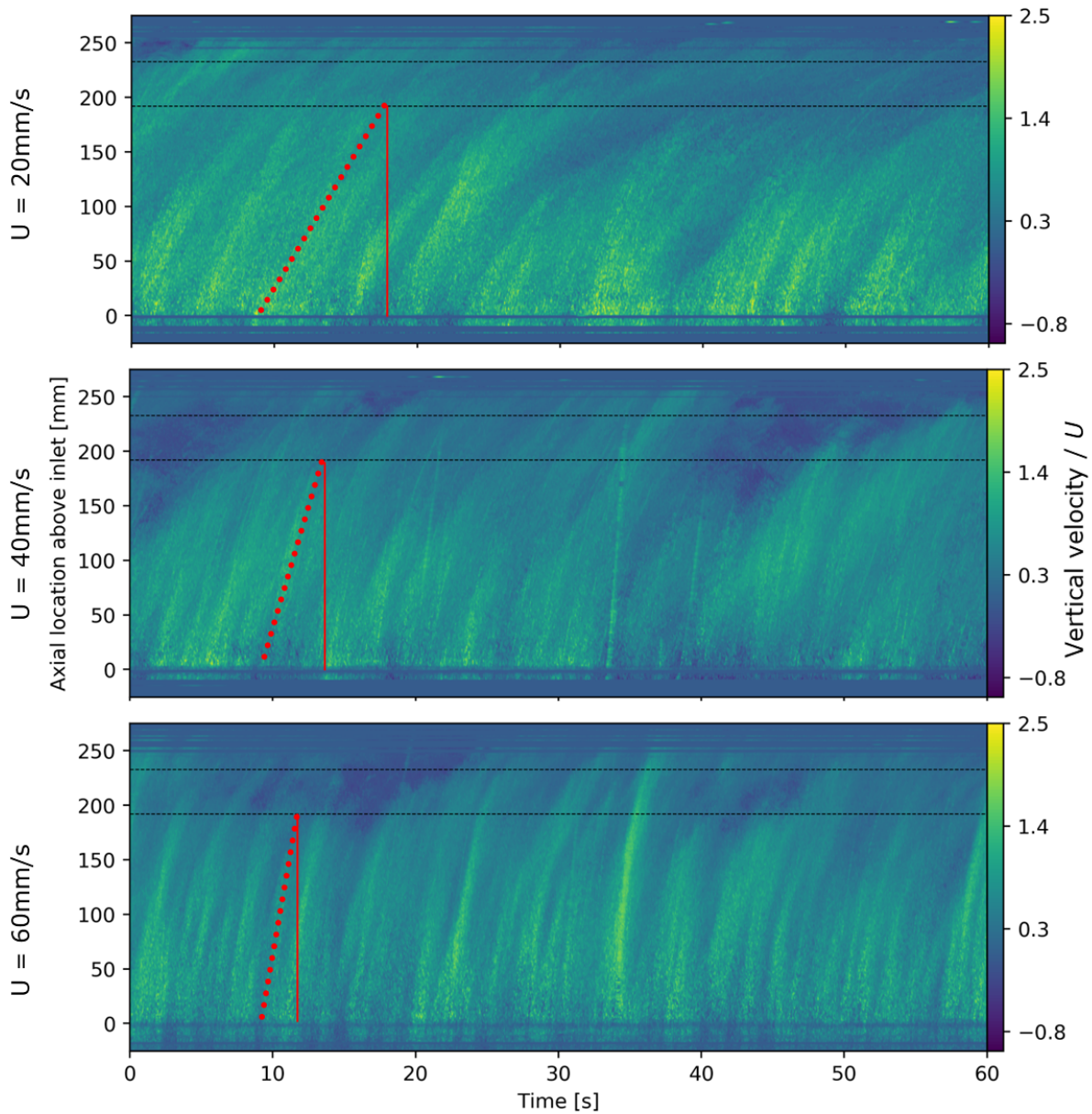


Figure 3.8: Isothermal contours of  $U = 20, 40,$  and  $60\text{mm/s}$  ( $Re = 3500, 7700, 10, 600$ ). Red lines show rise/run (displacement/time or velocity) of dominant eddies. At the core barrel height, solid-structure echoes cloud the signal; likewise, at the top, over saturation clouds the signal.

## Chapter 4

### Cold step-transient tests

## 4.1 Balancing buoyancy and inertia

This chapter<sup>1</sup> describes how the temperature distribution information is obtained using the experimental setup, with varied ‘core’ exit conditions, to observe the transition from stratified into mixing. In this case, with the  $Pr \ll 1$ , it is difficult to find a generic  $Ri$  based transition criteria. But, if existing empirical correlations can be used for estimating  $Pr_\tau$  for a particular fluid type with known  $Pr$ , then the transition or critical  $Ri$  can be obtained from critical  $Ri_f$  using Eqn. 1.2,  $Ri = Pr_\tau Ri_f$ . The transition criteria can be significantly important to gain fundamental understanding in geophysical flows<sup>9;11</sup> and to solve engineering problems such as design of heat storage systems<sup>62</sup> or fatigue analysis in nuclear reactor vessels.

The experiments reported in this work are particularly relevant to the reactor transient with the protected loss of flow scenario. The hot, lower-density fluid occupies the upper plenum when a slow colder fluid enters the bottom of the plenum from the shutdown core: a cold step test. Understanding this axial temperature distribution in a way that can be used for the safety analysis of these reactors and, in a broader sense, determining stratification or mixing for liquid metals is the goal of the experimental procedure described here.

## 4.2 Cold step-transient test procedure

### 4.2.1 Experimental procedure

There are three phases to each experimental test, summarized by Figure 4.1: fill and verification with flow rate set-point control; plenum heating and pre-transient preparation; and the test transient itself.

1. Before each round of tests, the GaTE is filled from its liquid holding tank. The plenum is filled to a level with accuracy of  $\pm 1\%$  of the scaled level. The liquid level is monitored by electrode contact to within  $1\%$  of the scaled height. For the results presented here,

---

<sup>1</sup>A majority of this chapter is reprinted with permission from “Thermal stratification in liquid metal pools under influence of penetrating colder jets” by Ward, Clark, and Bindra, 2019. Experimental Thermal and Fluid Science, 103, 118–125. 2019 by Elsevier.<sup>6</sup>

the SWI-DTS azimuthal location is nearest to the exits for all tests. The pump and an electromagnetic flow meter (EMFM) are tested against reference values obtained immediately after EMFM calibration to ensure that there is no drift or day to day dependence on pump or EMFM performance.

The pump's VFD and discharge control valve (CV) are used to control flow rate. The VFD output speed is held until the completion of the test - any manipulation of flow by valve arrangement can be reversed and the flow rate will return to the set-point value.

2. During the plenum heating and pre-transient preparation, the pump discharge CV is closed down to allow the flow rate through the 'core' heat exchanger to be optimized for temperature control output.
3. Data collection starts and the oil circulation heater is turned off. Then, simultaneously, the pump discharge CV is opened to allow the flow to return to the transient test case rate. Once no cooler power is required to maintain the inlet temperature at 50°C, the transient is considered over and data collection is stopped.

This setup and procedure are the prescribed ways to achieve conditions required to conceptualize the different possible stratification interface behaviors within the plenum. The description of what data and how it is collected is provided in the next section.

### 4.2.2 Experimental case studies

In order to conceptualize the transition from planar to fluctuating interface in the GaTE's liquid metal pool, seven different velocity conditions were evaluated at the same  $\Delta T$  (100°C–50°C).  $Ri$  ranged from 560 (an important condition for safety analysis of a safeguards cooling systems in liquid metal reactors<sup>1</sup>) down to 0.5 (well enough below  $Ri_f=1$  with any practical  $Pr_\tau$ ). The EMFM and inlet thermocouple were used to ensure experimental conditions were appropriate for the tests being conducted. The velocity is controllable to within  $\pm 2\%$  of

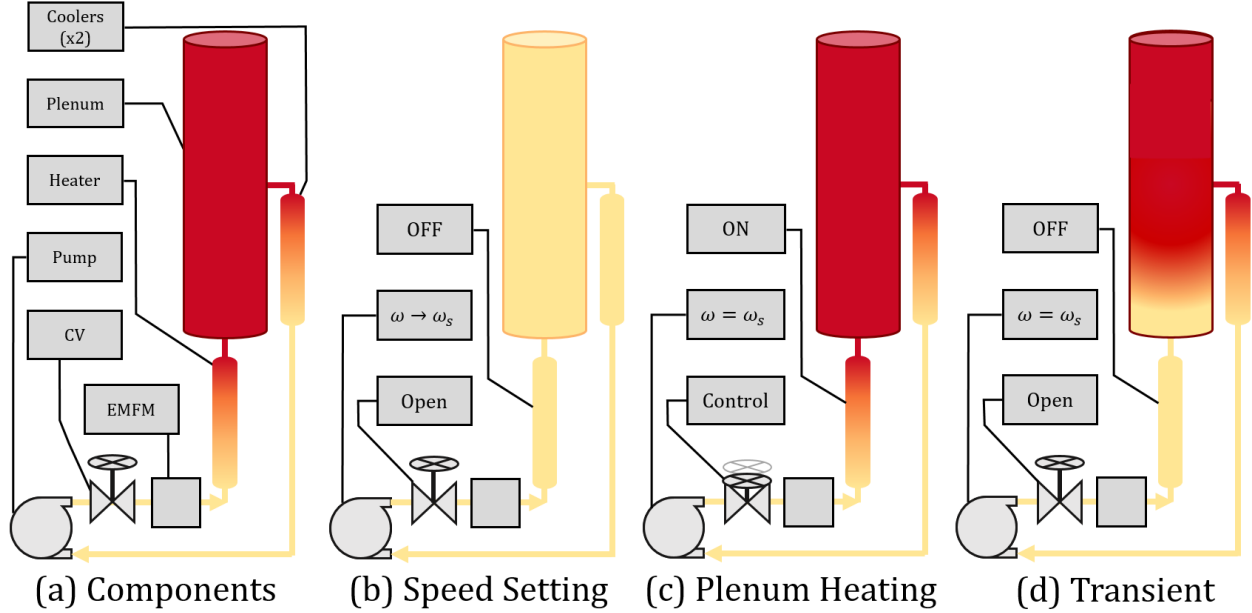


Figure 4.1: (a) Components of the GaTE system used for manipulation of fluid conditions to ensure accurate and repeatable transients. (b) The pump speed is set to meet the set-point flow rate requirements of the test. (c) The scaled plenum is heated to the set-point temperature. (d) The transient is started and data collection established.

the set-point value and was stable throughout the transients. Therefore, efforts to ensure experimental fidelity were focused on the control of the temperature.

While control of the loop injection temperature can be maintained, due to the thermal capacity of the ‘core’ and steel piping leading to the inlet of the scaled plenum, it is not possible to achieve a step change in temperature. The three slowest transients were most impacted by this, taking the most time before  $50^{\circ}\text{C}$  coolant passed through the ‘core’ and into the plenum. However, all transients had reached cold injection temperature prior to colder gallium exiting the plenum, allowing for the behavior of the temperature transient to be observed in its entirety in the lower plenum. An example transient, including system information is shown in Figure 4.2.

Input parameters (pre-transient plenum temperature, loop/injection temperature, and injection velocity) dictated test schedule. With a consistent  $\Delta T$  ( $100^{\circ}\text{C} - 50^{\circ}\text{C}$ ), the seven injection velocities were replicated at least three times to insure consistency of output parameters (SWI-DTS temperature profile and transient time). These experimental results are

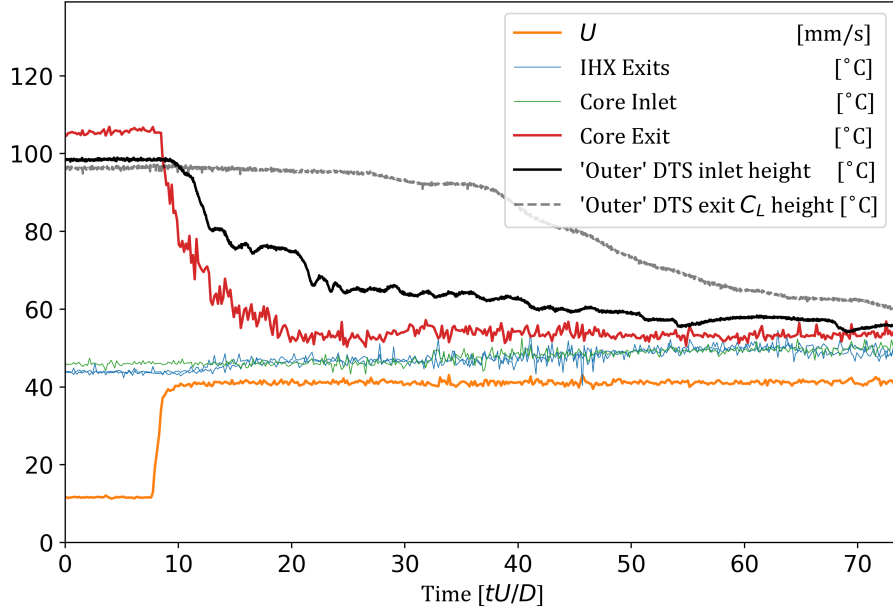


Figure 4.2: Example transient system information: EMFM output (scaled to represent core  $U$ ) and thermocouple readings are shown accompanied by plenum inlet and outlet height SWI-DTS information from the ‘outer’ DTS strand.

used to present temperature fluctuation and gradients in the plenum. The results are used to validate theoretical transition criteria in terms of  $Ri_f$  and an empirical model of  $Pr_{\tau}$ , presented in sub-section 4.3.1.

## 4.3 Results and discussion

### 4.3.1 Estimation of turbulent Prandtl number

$Pr_{\tau}$  cannot be observed without the use of vertical velocity perturbation and gradient evaluation. These parameters are necessary in the calculation of  $Ri_f$  behavior around its critical value. However, if  $Pr_{\tau}$  can be estimated, the link between experimentally controllable  $Ri$  and its counterpart,  $Ri_f$ , can be determined.

Previous estimates and theory on  $Pr_{\tau}$ <sup>63</sup> have been unsuccessful in predicting liquid metal

boundary layer behavior<sup>42</sup>. An equation based on modeled transport equations with empirically fitted coefficients is presented in<sup>3</sup>:

$$Pr_\tau = 0.85 + \frac{182.4}{Pr Re^{0.888}} \quad (4.1)$$

This generic correlation allows capture of higher  $Pr$  fluids while also exhibiting flexibility in use with liquid metals or other low  $Pr$  fluids. Using Equation 4.1 allows for prediction with liquid metal flow with the  $Re$  ( $Pe$ ) dependence of  $Pr_\tau$ <sup>42</sup> not normally exhibited by higher  $Pr$  fluids.

It should be noted that the theory is dependent on constants determined at higher  $Re$  flows and does not take into account distance from the walls. While the works used by Jischa & Rieke<sup>3</sup> and Weigand, Ferguson, & Crawford<sup>42</sup> use relatively high  $Re$  flows, similar behaviors in direct numerical simulation of flows comparable to the ones presented here have been observed<sup>6413</sup>. The approximation of  $Pr_\tau$  can be considered the mean for the entire boundary layer<sup>342</sup>, allowing for simple estimation of  $Pr_\tau$  and subsequently  $Ri_f$ .

### 4.3.2 Observation of critical $Ri$ in liquid metal

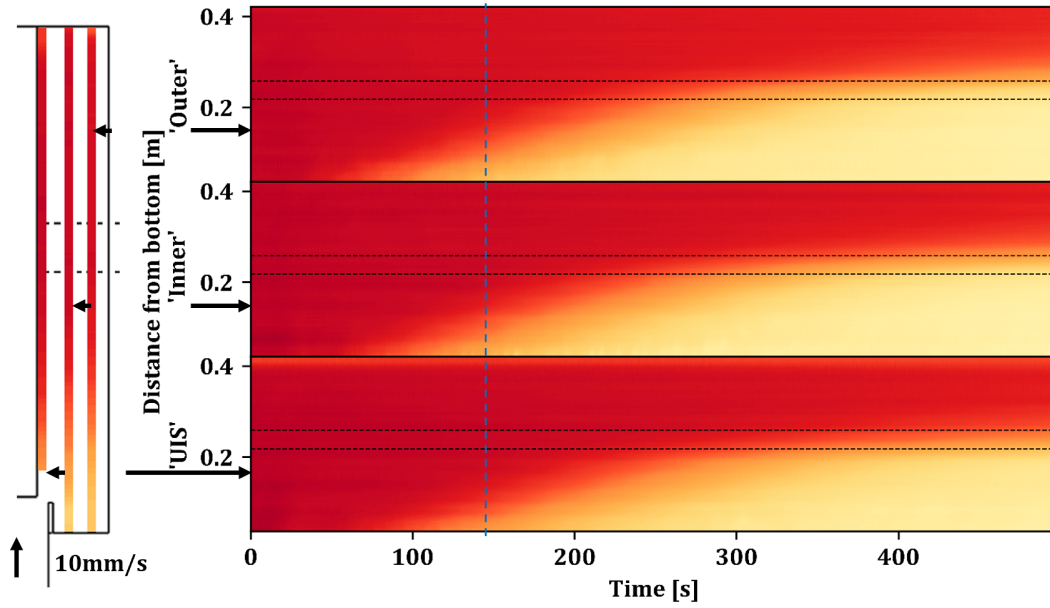
The design of the SWI-DTS geometry allows for high resolution axial temperature measurement of the entire plenum at multiple radial locations. Figure 4.3 shows two transients: 10mm/s ( $Ri_f = 3.1$ ,  $Re = 1770$ ) and 40mm/s ( $Ri_f = 0.54$ ,  $Re = 7070$ ) with each transient having a ‘snapshot’ one-dimensional axial temperature profile (left) and time-dependent temperature contour plot (right) showing the entire transient at each radial location. At lower  $Re$  (10mm/s), the normalization provided by the buoyant restoration creates a flat plane of temperature, effectively creating a unidirectional thermal stratification front in the plenum. In contrast, at higher  $Re$  (40mm/s), this unidirectional approximation is clearly invalid. But to see this effect throughout the entire transient, the use of a time-dependent contour plot is employed. Here, the structure of the front can be observed. In the 10mm/s case, a uniform diffusive thermal gradient is seen consistently advancing upwards through the plenum at all

radial locations as the cold (50°C) fluid enters from below. However, in the 40mm/s case, the consistent and predictable gradient is gone and has been replaced with fluctuations along the interface.

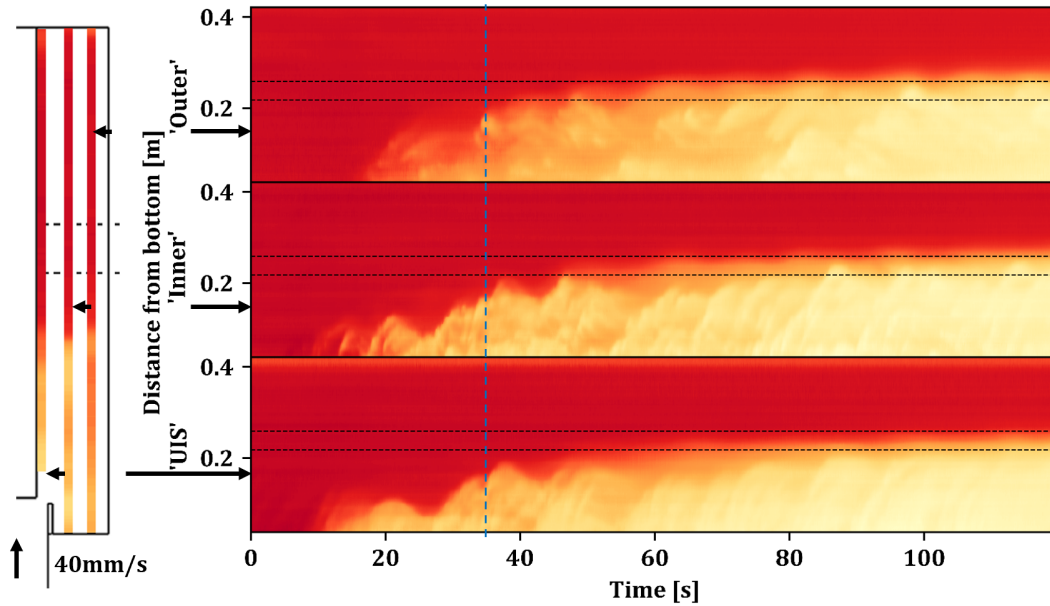
Evaluation of the gradients (both radially and axially) provide indication as to the degree of fluctuations occurring within the plenum. In Figure 4.4, the temperature difference for two radial locations is shown for three transients: 10mm/s, 20mm/s ( $Ri_f = 1.3$ ,  $Re = 3540$ ), and 40mm/s at the 0.20m height (just below the IHX exit channel). For every transient there is some effect on the profile by cooling of the walls (seen by the slight negative values), but this effect is well below what is caused by fluid fluctuations in the plenum as inlet speed is increased. In the 10mm/s case, the gradient is consistently negative and provides a baseline for comparison; in the 20mm/s case, there is clearly some divergence from the baseline, however, these fluctuations are within 5°C (10% of the total change); in the 40mm/s case, large, sharp swings with both positive and negative gradients can be seen with peak to peak amplitude >50% of the total change. This transition from planar stratified to fluctuating, shown in Figure 4.4, is part of the overall interpretation of the data. The axial gradients also provide valuable input.

In Figure 4.5, all seven inlet flow conditions are shown with their respective ‘inner’ time-dependent contour plots (2.39mm/s to 80mm/s - (a) to (g), respectively). Displayed to the left of the contours are the bulk flow parameters for reference and comparison:  $Ri$ ,  $Pe$ , and  $Re$ . And to the right are the estimated  $Pr_\tau$  and  $Ri_f$  values predicted by Equations 4.1 and 1.2. The first three transients ((a), (b), & (c)) exhibit the predictable evolution of the temperature gradient through the plenum up to the exit heights. (d) begins to diverge from this behavior. Although more diffuse, there are non-uniform structures that can be seen in the profile, just at a lower level than the first three transients (quantified in Fig. 4.4). In (e) there is a clear difference between it and any slower case. Large fluctuations in temperature can be seen as the front moves through the lower plenum. In the two fastest cases, (f) and (g), the front edge of the cold front and accompanying fluctuations are at the exits almost immediately after cold fluid enters the plenum.

The transition away from planar thermal stratification aligns well with expected values



(a)  $Ri_f = 3.1$ ,  $Re = 1770$ .



(b)  $Ri_f = 0.54$ ,  $Re = 7070$ .

Figure 4.3: SWI-DTS data at  $tU/d \approx 26$  into two transients for all radial locations [‘UIS’, ‘Inner’, & ‘Outer’] next to SWI-DTS data for the entire transient for these locations. Horizontal dashed lines represent plenum exit channel height; vertical solid lines on the contour plots represent the time snapshot.

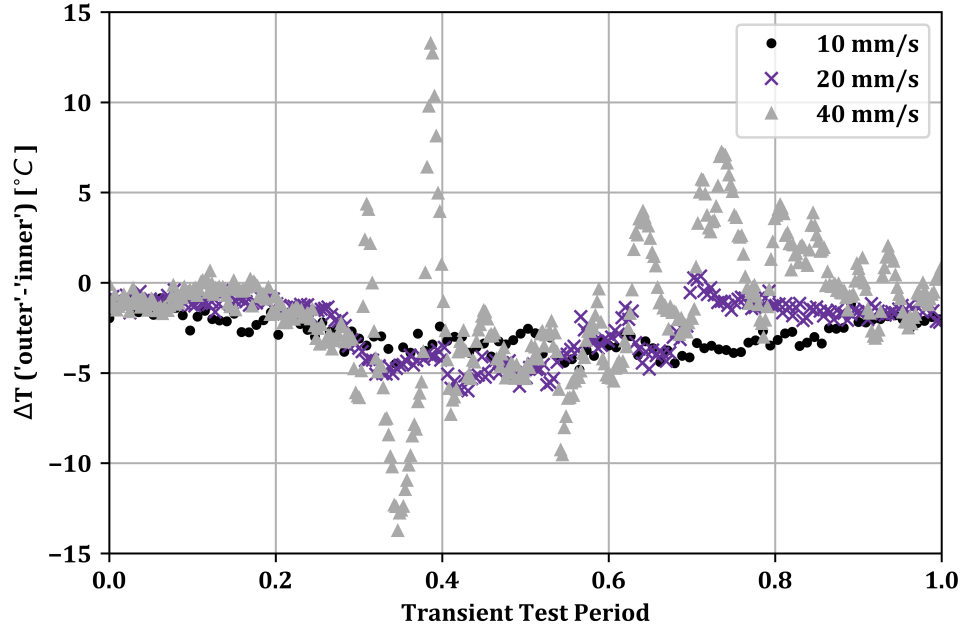


Figure 4.4: Radial temperature difference in the fluid segments of the SWI-DTS (‘outer’-‘inner’) of three inlet conditions nearing the transition away from unidirectional. Time series data is plotted for the entire transients at the 0.20m (above the bottom) height.

of  $Ri_f$ . At  $Ri = 8.0$  and  $Ri_f = 1.3$ , the temperature profiles maintain the predominantly unidirectional progression of the thermal stratification front. Only very small thermal fluctuations are observed, dissipating in the later stages of the test. When at  $Ri = 2.0$ ,  $Ri_f$  is below the theoretical critical limit for  $Ri_{f,crit} \leq 1$  with the value of 0.54. The stratification interface fluctuates, exhibiting no dependable radial or axial temperature profile.

## 4.4 Critical $Ri$ behavior

Exploration of the critical flux Richardson number  $Ri_{f,crit}$ , where turbulent kinetic energy generated by shear production is equal to the amount dissipated by buoyant potential, in a liquid metal plenum has been presented with the help of an experimental study. Parametric control of flow injection rates in the experiments is achieved by a moving magnet pump. High-resolution spatio-temporal temperature response in the plenum is monitored with the SWI-

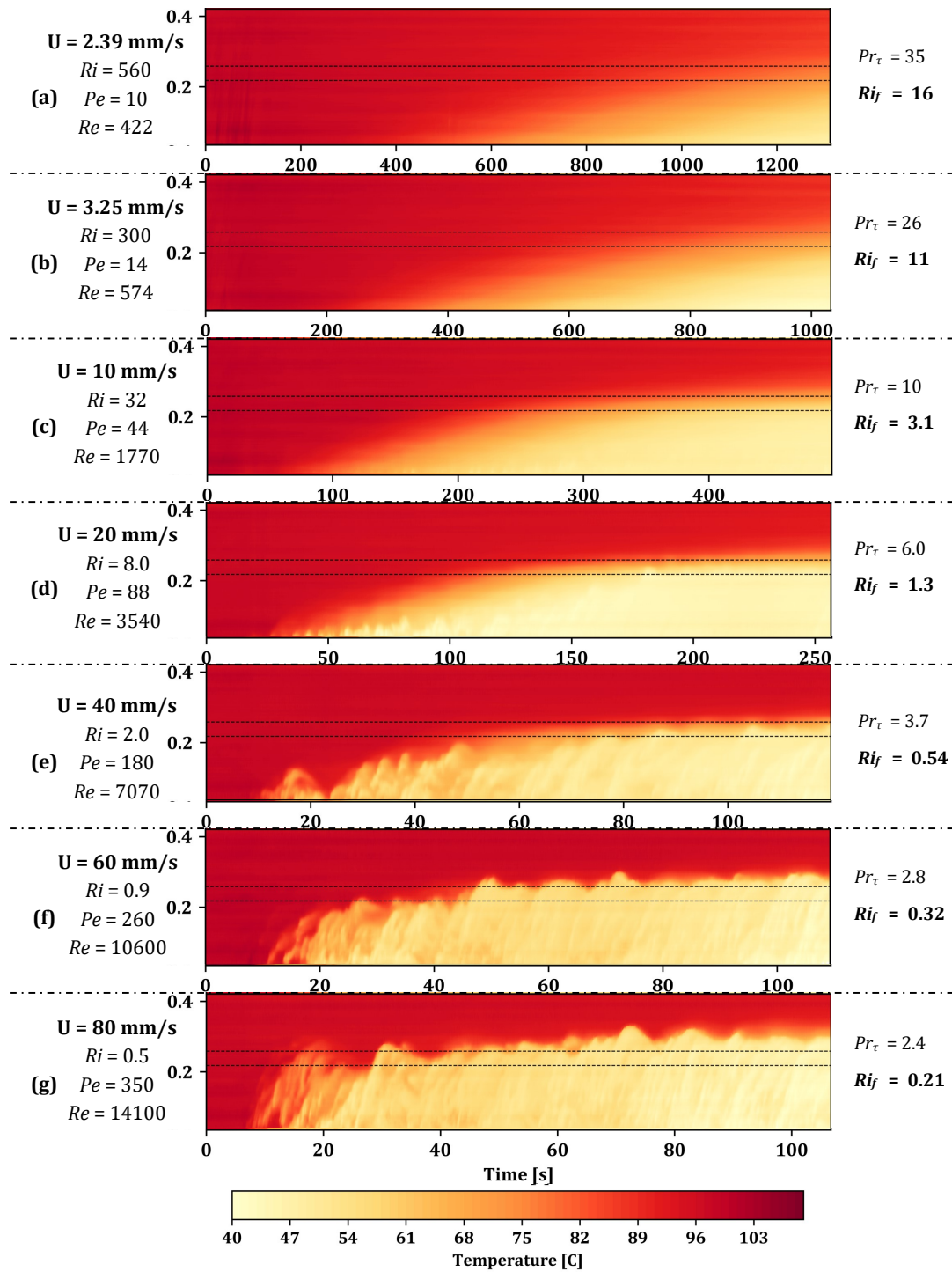


Figure 4.5: Axial temperature distribution of the 'Inner' SWI-DTS segment time-dependent contour (horizontal dashed lines represent plenum exit channel height). As  $Ri_f$  approaches its theoretical critical value of 1, the stratification is transitioning away from unidirectional; below  $Ri_f = 1$  clear fluctuations on the interface can be observed.

DTS. Cold fluid injection rate was the primary control variable in this experimental study and increase in the flow rates shows monotonic reduction in the  $Ri_f$ . Different experimental cases with  $Ri_f$  values 16, 11, and 3.1 clearly exhibit a unidirectional evolution of planar thermal stratification fronts. When  $Ri_f \sim 1.3$  small thermal fluctuations are seen near the injection end die away at later stages of the experiments. This is a special case as all other cases where  $Ri_f < 1.3$  the distinct presence of thermal fluctuations are observed at all times. For all cases with  $Ri_f \leq 0.54$ , non-uniform radial distribution is observed where the front is not unidirectional in the plenum. For  $Ri_f = 0.32$  and  $0.21$  thermal fluctuations dominate the behavior.

Experimental tests demonstrate that when the flux Richardson number is lowered to a theoretical critical value, the radial and axial temperature distribution in the plenum do not show a diffuse planar front. The experiments present clear agreement with the theoretical transition criteria of  $Ri_f \leq 1$  where thermal stratification front is expected to experience fluctuations, shown graphically in Figure 4.6. But the experiments were not able to measure or maneuver  $Ri_f$  directly. An approximate value of  $Pr_\tau$ , based upon the existing empirical correlations for liquid metals, was used to establish relationship between  $Ri_f$  and  $Ri$ . This is because  $Ri$  can be estimated directly from bulk parameters such as flow rates and  $\Delta T$ . Therefore, this experimental study was able to present a practically more relevant transition criteria based on the global Richardson number ( $Ri \leq 8$  in this geometry).

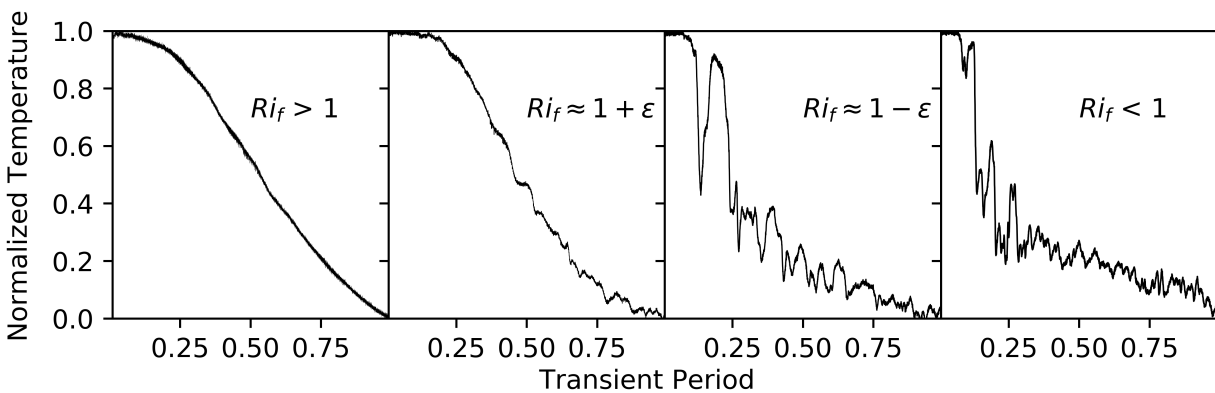


Figure 4.6: Regime transition through the critical flux Richardson number of 1.

Although the experimental results were able to validate theoretically expected critical  $Ri_f$  and empirical  $Pr_\tau$ , for their application to liquid-metal cooled reactor safety, more detailed experiments are needed. In order to make quantifiable interpretations such as directly estimating  $Ri_f$  from the experiments, detailed flow field measurements (leading to local estimates of  $w', \frac{\partial \bar{w}}{\partial z}$ ), are needed. For this, the UDV system will also be used in Chapter 5 to obtain these directly.

## Chapter 5

Turbulent scaling laws and their  
influence on eddy diffusion in liquid  
metal

## 5.1 Turbulent scaling framework

This chapter will address the physical meaning and variation in low Prandtl number fluids for two previously described models: the estimation of eddy thermal diffusivity from Chapter 2 ( $\hat{\kappa} = f(IRe/Ri)$ , with  $I$  turbulence intensity determined ad hoc using an additional empirical correlation) and the relationship for the turbulent Prandtl number of Chapter 4 ( $Pr_\tau = (C + D/(PrRe^{0.888}))$ , with  $C$  and  $D$  empirically determined). The  $\hat{\kappa}$  model was derived using Direct Numerical Simulation of stratified turbulence at a  $Pr$  of 0.72. *The Chapter 2 simulations show agreement with the model but experimental verification for  $Pr \ll 1$  is required. The  $Pr_\tau$  model is intended to be generic in nature, explicitly capturing low  $Pr$  effects, but the empirical constants are fitted using high  $Re$  pipe data, not large volume mixing.* The stability threshold determined using this model in Chapter 4 provided a global agreement; however, no direct measurement of the quantity was made. To understand these models and their behavior, to explicitly measure their quantities for verification in stably stratified turbulence of liquid metal, a framework for turbulent scaling laws is presented along with how the turbulent spectra can be used to map eddy thermal diffusivity.

Various heuristic theories have been used to describe the turbulent energy cascade from large scale to molecular dissipation (by diffusion of either temperature or momentum). Notably, Kolmogorov's 1941 theory<sup>16</sup> describes the -5/3 power law dependence through the inertial range of isotropic turbulent spectra - the velocity spectrum is proportional to  $k^{-5/3}$  where  $k$  is the wavenumber, Fourier component of the velocity spectra. This was later followed by various theories including the one independently developed by Bolgiano<sup>65</sup> and Obukhov<sup>66</sup> (BO59) as well as those outlined by Batchelor, Howells, and Townsend (BHT59)<sup>67</sup> with particular importance to microscale definitions of Equations 5.1 and 5.2, respectively. These theories describe the microscale dependence of spectral power law behavior, used here to explain this variation in mixing behavior. The first is the Bolgiano microscale (BO59), used here to describe the relative (buoyant) influence the scalar field has on the flow (i.e. how 'active' it is - the opposite of passive)<sup>68;69</sup>; the second is the thermal turbulent microscale (sometimes called the Obukhov-Corrsin scale, analogous to the Kolmogorov microscale and

in contrast to the Batchelor scale, more relevant to  $Pr > 1$  fluids), the scale at which molecular diffusion begins to dominate convective thermal fluctuations. The microscales (and reciprocal wavenumbers) are defined as

$$\frac{1}{L_B} \equiv k_B \equiv \frac{\chi^{3/4}}{\varepsilon^{5/4}} (g\beta)^{3/2} \quad \begin{array}{l} \chi \equiv \kappa \langle (\frac{\partial T}{\partial x_i})^2 \rangle \\ \varepsilon \equiv \nu \langle (\frac{\partial u_i}{\partial x_j})^2 \rangle \end{array} \quad (5.1)$$

$$\frac{1}{\eta_T} \equiv k_{\eta_T} \equiv \left( \frac{\kappa^3}{\varepsilon} \right)^{-1/4} \quad (5.2)$$

where  $\chi$  and  $\varepsilon$  can be thought of here as the respective average dissipation rates for potential and kinetic energy along with the partial derivatives (summed by Einsteinian notation) of temperature,  $T$ , and velocity,  $u$ .

While other scales are important in the study of density stratified flows<sup>70;71</sup>, this chapter will focus on these two only. Other important scales (namely Ozmidov and Thorpe) are not as relevant in the geometry and flow configuration under investigation here; only in a portion of the test geometry, where the mean vertical flow is zero, do these scales become important but have been left out of the scope for this work.

The inertial-convective range, defined by the following spectral behavior, can be broken down by either passive or active scalar participation. Obukhov<sup>66</sup> and Corrsin<sup>17</sup> generalized the arguments in K41 theory to that of a passive scalar. The spectral density of momentum,  $E$ , is only dependent on the kinetic energy dissipation rate and wavenumber (K41); the spectral density of temperature  $\Gamma$  is additionally dependent on the dissipation rate of its variance. That is:  $E \sim \varepsilon^{2/3} k^{-5/3}$  is analogous to  $\Gamma \sim \chi \varepsilon^{1/3} k^{-5/3}$ . BO59 theory accounts for buoyancy's impact in both momentum and temperature:  $E(k) \sim \chi^{2/5} (g\beta)^{4/5} k^{-11/5}$ ,  $\Gamma(k) \sim \chi^{4/5} (g\beta)^{-2/5} k^{-7/5}$ . Their transition scale is defined in Equation 5.1 but it can be easily derived by setting the scaling regimes equal to one-another and solving for the wavenumber ( $\chi \varepsilon^{1/3} k^{-5/3} \sim \Gamma \sim \chi^{4/5} (g\beta)^{-2/5} k^{-7/5} \rightarrow k_B \equiv \frac{\chi^{3/4}}{\varepsilon^{5/4}} (g\beta)^{3/2}$ ). Conceptually, this represents the exchange of kinetic energy into the background potential field with the momentum spectrum losing energy faster than isotropic turbulence ( $11/5 > 5/3$ ) and the thermal spectrum losing energy to the smaller scales less quickly ( $7/5 < 5/3$ ). These scaling laws are listed in Table 5.1

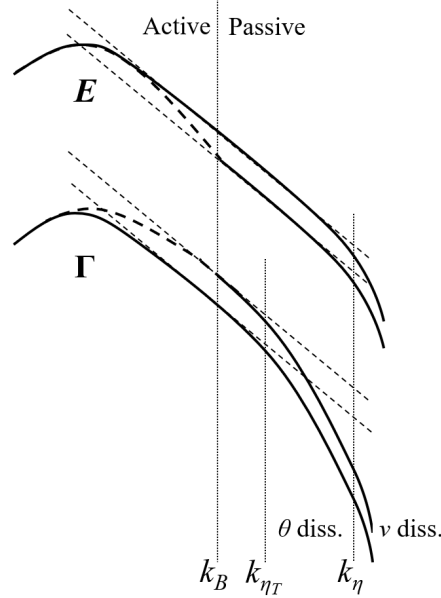


Figure 5.1: Pictorial turbulence spectrum of the velocity and temperature shown with dashed line modifiers for active regions of the spectrum. Parallel lines in the passive region show  $-5/3$  power law scaling (K41); vertical lines show important microscales:  $k_B$  - Bolgiano (Active $\rightarrow$ Passive);  $k_{\eta T}$  - Obukov-Corrsin (inertial-convective  $\rightarrow$  inertial-diffusive); and  $k_\eta$  - Kolmogorov (inertial  $\rightarrow$  diffusive).

and shown pictorially in Figure 5.1 along with the influence the low  $Pr$  has on the thermal spectrum, described next.

Table 5.1: Scaling laws of liquid metal mixed convection.  $k^n$  dependence breakdown by scale regime and variable.

| Regime                 | $E(k)$  | $\Gamma(k)$   |
|------------------------|---------|---------------|
| $1/L > k > 1/L_B$      | $-11/5$ | $-7/5$        |
| $1/L_B > k > 1/\eta_T$ | $-5/3$  | $-5/3$        |
| $\eta_T > k > 1/\eta$  | $-5/3$  | $-9/3, -17/3$ |

The discussion on the inertial-diffusive range exclusive to low  $Pr$  fluids (inertial characteristics of the momentum with diffusive scalar behavior) has need of additional data sets<sup>72;73</sup>. Scaling analysis of this range has indicated two power law behaviors:  $\Gamma \sim \chi \varepsilon^{2/3} \kappa^{-3} k^{-17/3}$  from the BHT59 analysis and, separately,  $\Gamma \sim \chi \kappa^{-1} k^{-3}$  from Gibson<sup>74;75</sup>. These are listed in Table 5.1. No breakdown of the inertial diffusive range is shown on Figure 5.1 (more on this in Gibson<sup>76</sup> and later in this chapter) but what is demonstrated is the much steeper cascade in this region - quickly removing thermal fluctuations at smaller scales to molecular action.

There are very few data sets capturing this scaling law behavior of liquid metal with both temperature and velocity<sup>77–79</sup>. There is a unique opportunity to observe the spectra and how the scaling law behavior changes based on global parameters with the GaTE system.

## 5.2 GaTE tests

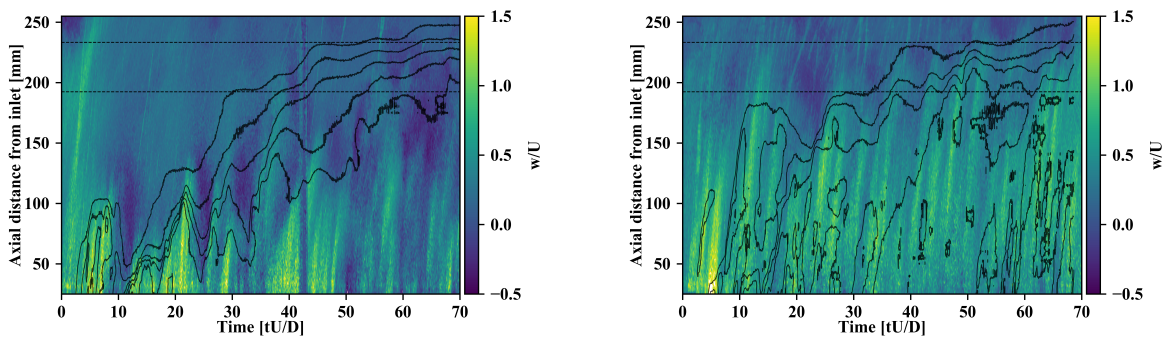


Figure 5.2: Cold step-transient ( $Pe = 180, 260$  (left, right),  $g\beta\Delta T = 0.006$  (both)) with temperature isotherms drawn in black over the velocity contour. Dashed black lines indicate exit channel dimensions.

To understand the factors influencing scaling law behavior in liquid metal, the GaTE can sweep through cold step tests with stability criteria near  $Ri_f = 1$ . The cold step-transients are performed as described in Chapter 4 by injecting cold fluid at the bottom of a preheated plenum. Injection velocities, constant throughout their respective tests, were paired with a preset temperature difference. To maintain margin between the cold temperature and freezing, the minimum temperature of the loop was maintained at  $50^\circ\text{C}$  with the initial plenum temperature at  $100^\circ\text{C}$  ( $g\beta\Delta T = 0.006$ ). Example cold step data are shown in Figure 5.2 where the color contour displays the velocity and the black line contour shows isotherms of the temperature, displayed together to show their interaction. The lower global  $Pe$  transient shows a close coupling between the two sets of data and internal waves, especially closer to the bottom, where large-scale oscillations can be seen. In contrast, the  $Pe = 260$  transient has fewer definitive coupled features in the lower plenum. While this display helps qualitatively show the relative passivity of the transients in the time-domain, a deeper, more quantitative understanding of the respective turbulent spectra will be required.

## 5.3 Scaling law results

### 5.3.1 Transient evolution of turbulent scaling

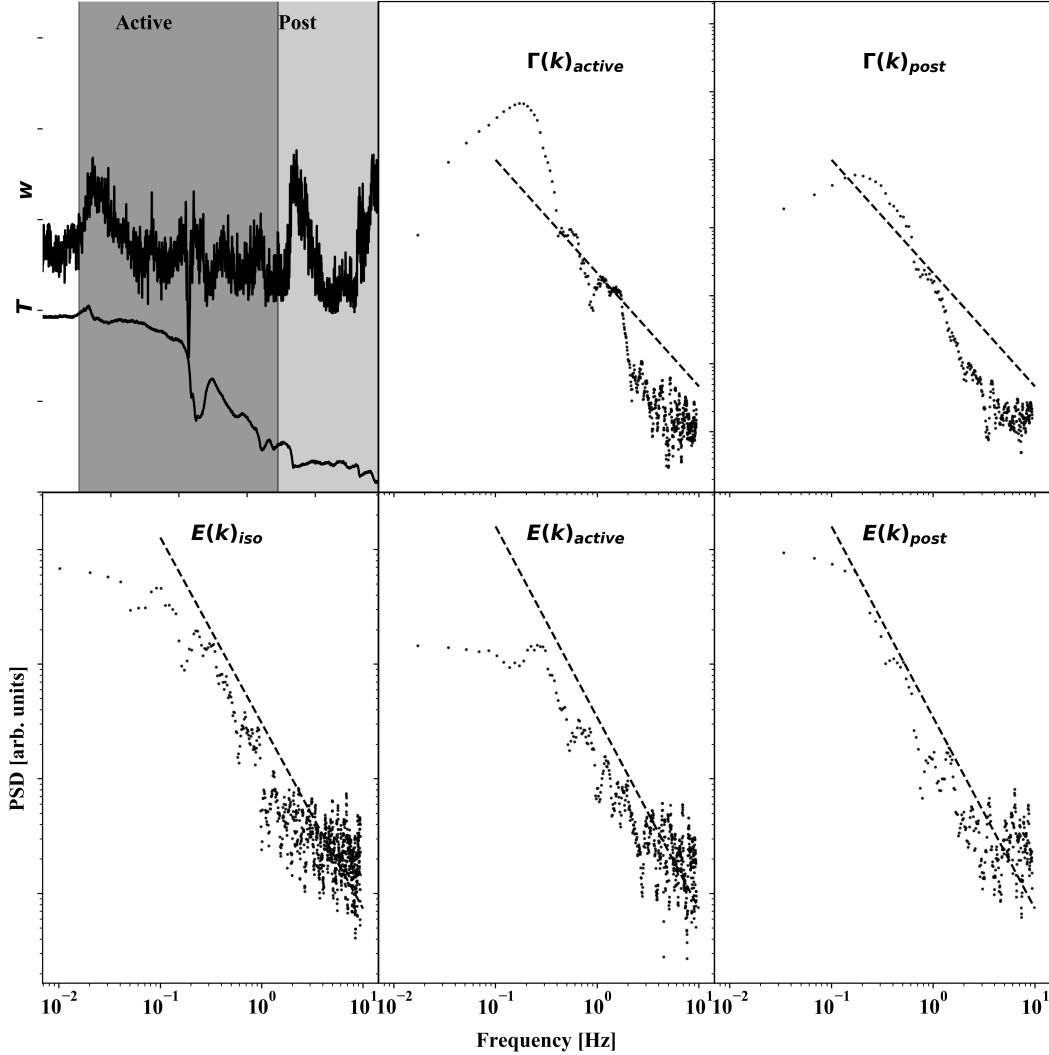


Figure 5.3:  $Pe = 180$  spectral composition of  $w'$  (isothermal-active transient-post transient :: left-right) and  $T'$  (active - post transient :: left-right) at the  $z = 125mm$  location. The active transient period shows similar theoretical features illustrated in Fig. 5.1.  $-5/3$  power law lines are drawn for reference in each.

By looking at different time windows of the transient period, the relative passivity of the scalar field can be observed. Three regimes are shown in Figure 5.3: isothermal (completely passive, N/A), active transient (least passive), and post transient (mostly passive). The BO59 scaling laws should only apply to the active transient period, where buoyancy has the largest

role; described pictorially in Figure 5.1. The isothermal tests procedure is as described in Appendix F<sup>61</sup> and represents 6000 time steps at 18.8Hz. This reference spectrum is shown in the bottom left of Figure 5.3. The remaining panes show the behavior of a  $Pe = 180$  cold step-transient. The temporal data, including the expected ‘Active’ and ‘Post’ zones, representing roughly 800 time steps each, is shown for transient with the corresponding  $z = 125mm$  temporal data in the bottom left. The remaining four panes show temperature (top) and velocity (bottom) spectra in an attempt to highlight the regions seen pictorially in Figure 5.1.

Clearly, the information pertaining to scaling laws for short time windows is more difficult to visually decipher than one would hope. The only discernible spectral feature is the knee in temperature (just below 1 Hz), corresponding to the thermal microscale. The perception problem exists even when computing only the power spectral densities<sup>80</sup> of the fluctuating components,  $w'$ ,  $T'$  (as shown in the figure - with the large motions subtracted out by a moving-mean, moving-median filter with window width set to 10% of the transient period). With such a small difference (e.g.  $-5/3$  vs.  $-7/5$  for  $T'$ ), a different technique will have to be used to identify active spectrum scaling laws.

### 5.3.2 Spectral Richardson number and BO59 scaling

Besides development of the scaling law behavior in active turbulence, Bolgiano<sup>65</sup> also developed a spectral representation of the Richardson number based on similarity constraints from Batchelor<sup>81</sup>:  $Ri_x \sim (g\beta)k^{-1/2}\Gamma(k)^{1/2}/(kE(k))$ . When  $E$  and  $\Gamma$  are governed by active scalar participation, as described in BO59 scaling ( $E(k) \sim \chi^{2/5}(g\beta)^{4/5}k^{-11/5}$ ,  $\Gamma(k) \sim \chi^{4/5}(g\beta)^{-2/5}k^{-7/5}$ ), then the spectral Richardson number,  $Ri_x$ , is unity by definition. This can be seen in Figure 5.4 where two sets of tests (two each for  $Pe = 180, 260$ ) are shown with their location dependence of  $Ri_x$ . Of importance in this Figure is the frequency at which  $Ri_x$  diverges from unity is the buoyancy (Brunt-Väisällä) frequency,  $N$ , above which the faster turbulent events are only weakly influenced by buoyancy<sup>40</sup>. This interaction is also a cue that inspection of the spectra ( $E, \Gamma$ ) around  $Ri_x = 1$  should be governed by BO59 behavior.

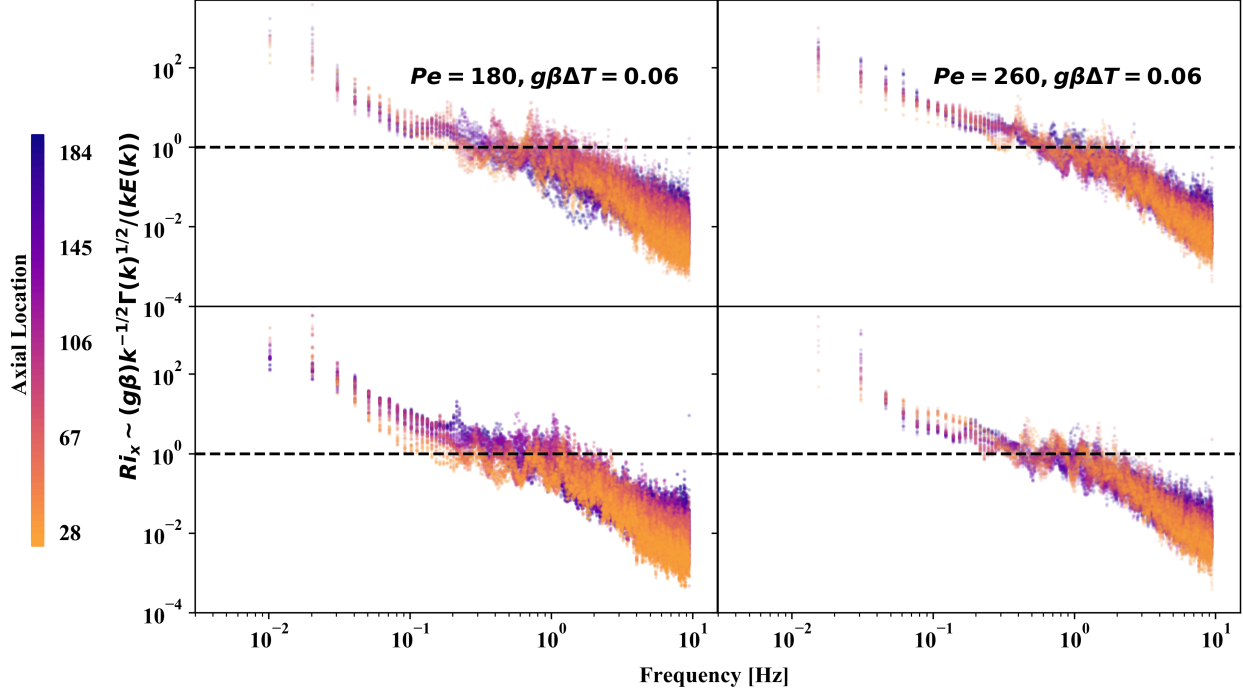


Figure 5.4:  $Ri_x$ : Spectral  $Ri \sim (g\beta)k^{-1/2}\Gamma(k)^{1/2}/(kE(k))$ , two replicates (top,bottom) for each set of  $Pe$ .  $Ri_x = 1$  for active turbulence; the narrower the spectral range at unity, the more passive the behavior.

Taking a closer look at this is Figure 5.5. For the corresponding  $Pe$  and  $z$ , a shaded region around  $Ri_x \approx 1$  is shown and carried through the compensated ( $\times k^n$ ) spectra and co-spectra ( $\Sigma(k) \sim \chi^{3/5}(g\beta)^{1/5}k^{-9/5}$  for  $w'T'$ <sup>68;73</sup>). In all cases the total window is less than a decade, consistent with expectations in low  $Pr$  active turbulence<sup>68</sup>. General trends in the scaling follow from inspection of the definition of the Bolgiano microscale (Equation 5.1). The difference in  $Pe$  are shown to push the cutoff scale to lower frequencies for the faster inlet cases; likewise, the the lower end of the spectrum is truncated at the higher speeds due to energy deposition at faster scales. This all leads to smaller windows of BO59 scaling for the higher  $Pe$  cases. The impact of distance from the inlet plays is less pronounced in these cases; however, the local  $Pe$  and therefore local thermal microscale are impacted. In the case  $Pe = 180$  and  $z = 151$  of Figure 5.6 the apparent thermal microscale attenuates the thermal response before the BO59 region even begins. Further investigation of the thermal spectrum specifically to survey the inertial-diffusive range, the behavioral range that makes low  $Pr$  fluids unique, is then required.

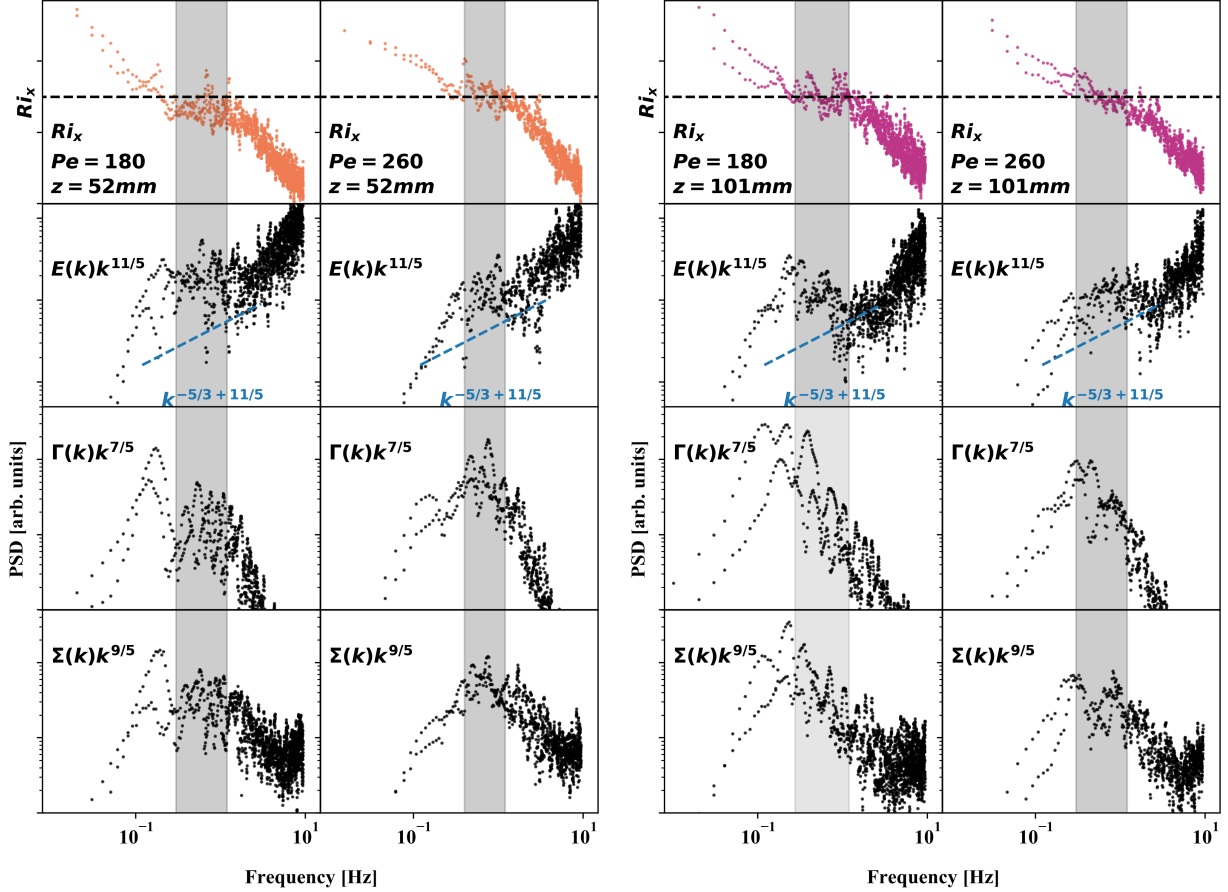


Figure 5.5: Spectral  $Ri$  (top) - color mapping elevation is consistent with Fig. 5.4.  $Ri_x \approx 1$  (shaded region) compared to compensated ( $\times k^n$ ) spectra of  $w'$  ( $E(k)$ ),  $T'$  ( $\Gamma(k)$ ), and co-spectra  $w'T'$  ( $\Sigma(k)$ ).

### 5.3.3 The thermal microscale

The theories of BHT59<sup>67</sup> (-17/3 scaling law) and Gibson's<sup>74;75</sup> (-9/3 scaling law) were shown to both exist simultaneously at different points in the spectrum, with no one scaling relation dominating the entire inertial-diffusive range<sup>76</sup>. With the temporal resolution of the GaTE's SWI-DTS, these ranges are distinguishable (though with some limitations). In Figure 5.7, multiple compensation orders of the same thermal spectra (at different  $Pe$  and  $z$  location) are shown similar to Gibson (1978)<sup>76</sup>. The uncompensated spectra are shown in the insets and are truncated to avoid the distortion of the noise floor which alters the maximum value, especially for the -17/3 regime. While not the purpose of the manipulation, the truncation does show how as elevation increases (local  $Pe$  decreases) the variance,  $\Gamma(k)$ , decreases to

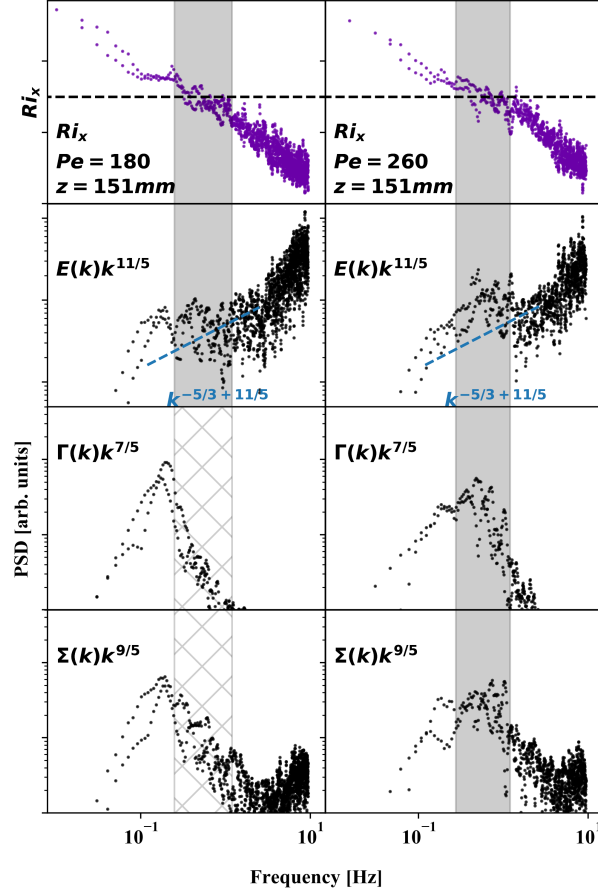


Figure 5.6:  $Ri_x \approx 1$  (shaded region) compared to compensated spectra of  $w'$  ( $E(k)$ ),  $T'$  ( $\Gamma(k)$ ), and co-spectra  $w'T'$  ( $\Sigma(k)$ ). In the case with lower inlet velocity higher in the plenum, the BO59 scaling is replaced by inertial-diffusive temperature scaling.

levels lower than can be differentiated from noise.

The other important trends from the figure are that the  $-9/3$  scaling is an intermediate scaling law between the  $-5/3$  (or  $-7/5$ , which is not easily contrasted from  $-5/3$  in this plot) and  $-17/3$ . In general, the  $-9/3$  scaling is the most dominant for the GaTE thermal dynamics. As the elevation increases the microscale corresponding to the intersection of  $-5/3$  and  $-9/3$  decreases, consistent with Equation 1.4 ( $\eta_T/l = Pe_l^{-3/4}$ , replacing the  $L$  with  $l$  for local scaling). All of this is consistent with the previously described literature and another validation data set has been added to a limited list. True not only for the inertial-diffusive scaling, but the BO59 scaling in liquid metal as well.

To summarize the results from this section:

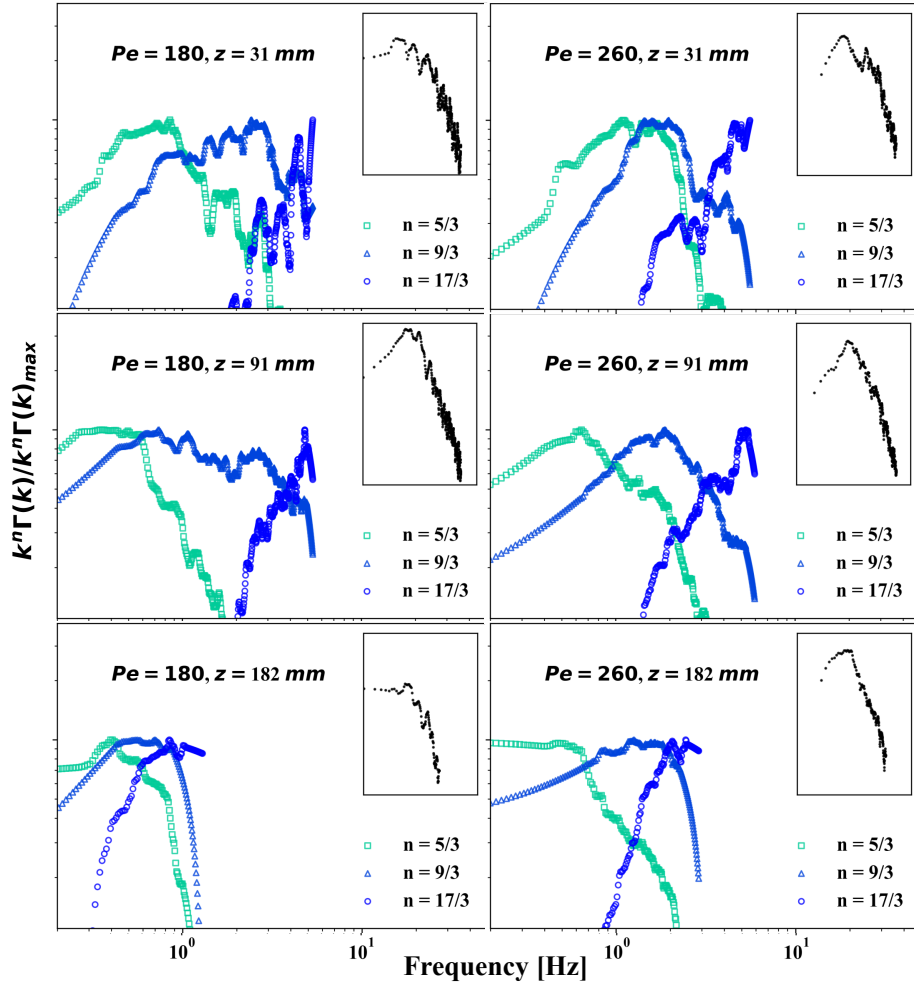


Figure 5.7: Compensated thermal spectra to identify inertial-diffusive scaling law regions; un-compensated corresponding spectra are shown in the insets.

1. With the aid of the spectral  $Ri$ , the range which signifies active scalar turbulence was highlighted - Fig. 5.4. This range is impacted by a variety of factors.
2. To increase the range to lower frequencies a lower local  $Pe$  is required - by either increasing elevation away from the inlet or decreasing global  $Pe$  - Fig. 5.5.
3. Lower local  $Pe$  also lowers the frequency of the thermal microscale. Truncation of the active region can occur when the inertial-diffusive sub-range dynamics begin to dominate - Fig. 5.6.

The next section uses the spectral integrals for quantity estimation with the behavior explained by these trends.

## 5.4 Eddy diffusivity results

In the previous section, the spectra of velocity and temperature were used to affirm scaling law theory for active scalar turbulence of a low  $Pr$ . The spectral representation of Richardson number that was developed by Bolgiano<sup>65</sup> was used to help determine active scaling regions in the frequency domains of interest. This is one of the many Richardson numbers available with scaling following the constraints of similitude<sup>81</sup> (e.g. ‘global’, ‘flux’, ‘gradient’, ‘spectral’). This section presents how the values of variances (e.g.  $\langle w'^2 \rangle = \int_0^\infty E(k)dk$ ) can be used to approximate the local structures that influence eddy thermal diffusivity including  $Ri$ .

Chapter 2 outlined an empirical framework<sup>4;40</sup> that was used to quantify the scaling distortion. That framework outlines the total diffusivity,  $\hat{\kappa} = (\kappa_\tau + \kappa)/\kappa$ , as a function of the turbulent Reynolds number divided by the Richardson number,  $Re_\tau/Ri$ . The behavior is divided into the three regimes shown in Figure 2.3 of molecular, transitional, and energetic. To corroborate this framework and provide a familiar basis for comparison, the GaTE UDV and SWI-DTS data were used to construct  $\kappa$  as well as  $Re_\tau/Ri$  with the following spectral definitions and measurement uncertainties:

$$\kappa = \sqrt{\frac{\langle (w'T')^2 \rangle}{\langle (\partial\bar{T}/\partial z)^2 \rangle}} \pm 16.6\% \quad (5.3)$$

$$Re_\tau = \frac{\sqrt{\langle w'^2 \rangle} D}{\nu} \pm 14.5\% \quad Ri = \frac{g\beta\sqrt{\langle (\partial\bar{T}/\partial z)^2 \rangle}}{\langle (\partial\bar{w}/\partial z)^2 \rangle} \pm 12.3\% \quad (5.4)$$

$$Re_\tau/Ri = \frac{\sqrt{\langle w'^2 \rangle} D}{\nu} \frac{\langle (\partial\bar{w}/\partial z)^2 \rangle}{g\beta\sqrt{\langle (\partial\bar{T}/\partial z)^2 \rangle}} \pm 19.1\% \quad (5.5)$$

### 5.4.1 Mapping diffusivity measurements

To achieve a more granular map of the diffusivity response, each transient was divided into 200 uniform temporal intervals. Computation of the integrated spectra was carried out using trapezoidal approximation on each interval:  $\langle w'^2 \rangle_{0-200} = \int_0^\infty E_{0-200}(k)dk$ . Shown in Figure 5.8 are the  $\kappa$  (5.3) by  $Re_\tau/Ri$  (5.5) maps. The medians are shown as the top dashed blue

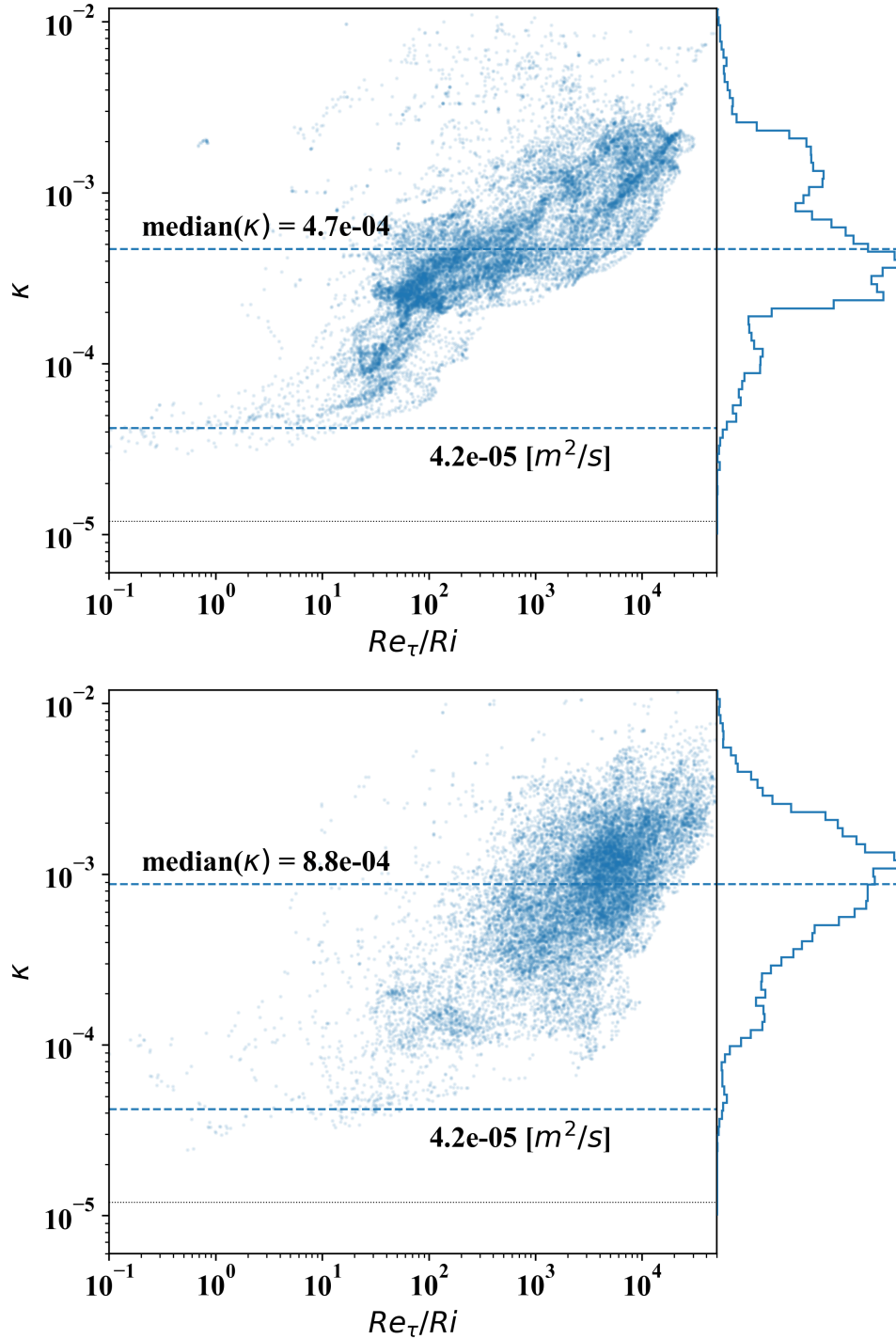


Figure 5.8: Eddy thermal diffusivity measurement map for transients  $Pe = 180$  (top) and  $Pe = 260$  (bottom) with respective histograms. Blue dashed lines corresponding to their respective medians are provided as well as the lower ‘floor’ of the diffusivity. The black dotted line is the molecular value ( $1.2 \times 10^{-5} \text{ m}^2/\text{s}$ ).

line with their respective values; as expected, the higher  $Pe$  results in an increased  $\kappa$  median. (Due to near zero temperature gradients there are outliers that the means are more sensitive to.) For each there is a shared ‘floor’ in the total diffusivity of the system corresponding to the lower molecular diffusivity limit. The value is 3.5 times the molecular value of  $1.2\text{e-}05\text{ m}^2/\text{s}$ , likely due to the physical separation of the sensors for  $w'T'$  computation.

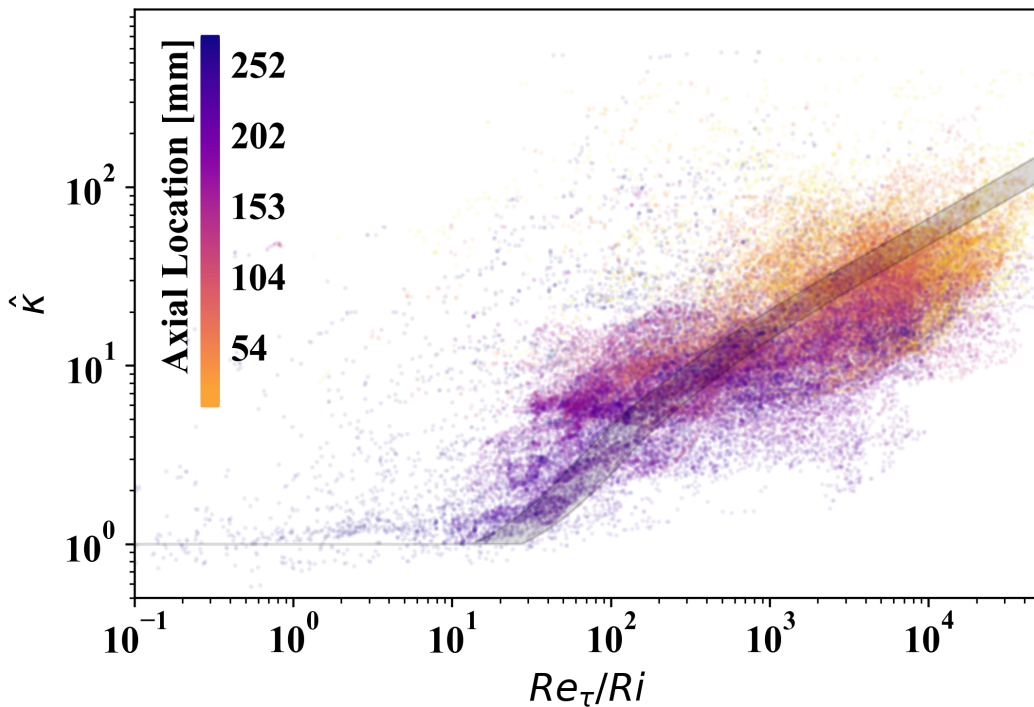


Figure 5.9: Normalized eddy thermal diffusivity measurements from the GaTE. The points represent all transient cases,  $Pe = 180, 260$  at  $g\beta\Delta T = 0.006$  (2 each), at all elevations measured during all temporal intervals. The grey band shows the smoothed empirical relationship described in Figure 2.3.

This bias correction has been carried forward through the rest of this chapter. To start with, it has been used to normalize the data in Figure 5.9 shown with all four transient tests. Additional information has been provided for elevation as well as the empirical relationship between  $\hat{\kappa}$  and  $Re_\tau/Ri$  illustrated in Figure 2.3 of Chapter 2 with banding inclusive of a range of turbulence intensities,  $I = \frac{w'}{w}$ <sup>82</sup> ( $Re_\tau = 5\%Re$  [same as Chapter 2] to  $10\%Re$  [more in line with Figure 2.6]). The most energetic mixing occurs at the bottom of the plenum, nearest the inlet with the transition to molecular diffusivity occurring over the region closer

to the exits. Almost all of the molecular level diffusivity occurs above the exit channel height ( $z > 233mm$ ) where the turbulence is weakest. Showing that Shih's<sup>4</sup> parameterization of eddy thermal diffusivity normalized by  $Re_\tau/Ri$  is the first step; however, there still needs to be accounting for  $Pr_\tau$  in the model.

To map  $Pr_\tau$  similarly to the map in Figure 5.9 an estimate and uncertainty for eddy momentum diffusivity needs to be formulated similarly to that of Equation 5.3:

$$\nu = \sqrt{\frac{\langle (w'u')^2 \rangle}{\langle (\partial\bar{w}/\partial z)^2 \rangle}} \sim \frac{\langle (w'^2) \rangle}{\sqrt{\langle (\partial\bar{w}/\partial z)^2 \rangle}} \pm 30.7\% \quad (5.6)$$

However, due to geometric constraints and the inability to measure UDV through the plenum wall, no radial velocimetry is available at this time. Given the data provided, the best estimate for  $\langle w'u' \rangle$  is going to be  $\langle w'u' \rangle$  ( $\langle w'^2 \rangle$ ). In the mixed convection flow, local anisotropy ( $\langle w'^2 \rangle \neq \langle u'^2 \rangle$ ) is entirely expected. However, given that liquid metals have a much smaller active spectral region ( $1/L < k < 1/L_B$ ; shown here and in literature<sup>68;78</sup>), the assumption of local isotropy may not result in poorly estimated  $\langle w'u' \rangle$  magnitudes. Using this assumption, Figure 5.10 shows the variation of  $Pr_\tau$  measured this way (ratio of Equations 5.6 and 5.3, bias corrected) with respect to the  $Ri$  of Equation 5.4. This is compared to Jischa's 1979 model<sup>3;42</sup>, used in Chapter 4 to lay the groundwork for understanding  $Ri_{f,crit}$  in the GaTE.

The substitution of  $\langle w'u' \rangle$  into  $Pr_\tau$  seems to have been acceptable. The information drawn from higher in the plenum shows  $Pr_\tau$  decreases with elevation, consistent with observations of slower (lower  $Re$ ,  $Pe$ ) flows. Most of the estimates for  $Pr_\tau$  are above or near the  $Re \rightarrow \infty$  limit of 0.85 with a few outlying exceptions. To cross check these values, those obtained in Chapter 4 for determining  $Ri_f = 0.54$  and  $0.32$  (for  $Pe = 180$  and  $260$  at  $g\beta\Delta T = 0.006$ ) via Equation 1.2 ( $Ri = Pr_\tau Ri_f$ ) shows a combined average of 0.99 and 0.37, respectively. The second set (0.32 vs. 0.37) is a much better comparison, most likely due to the higher  $Re$  and, therefore, local isotropy. Based on this confirmed understanding of the eddy diffusivities (and their ratio), the next sub-section offers an overview of the impact the turbulent scaling laws have and provides a final, combined closure to the models and assumptions used throughout this dissertation.

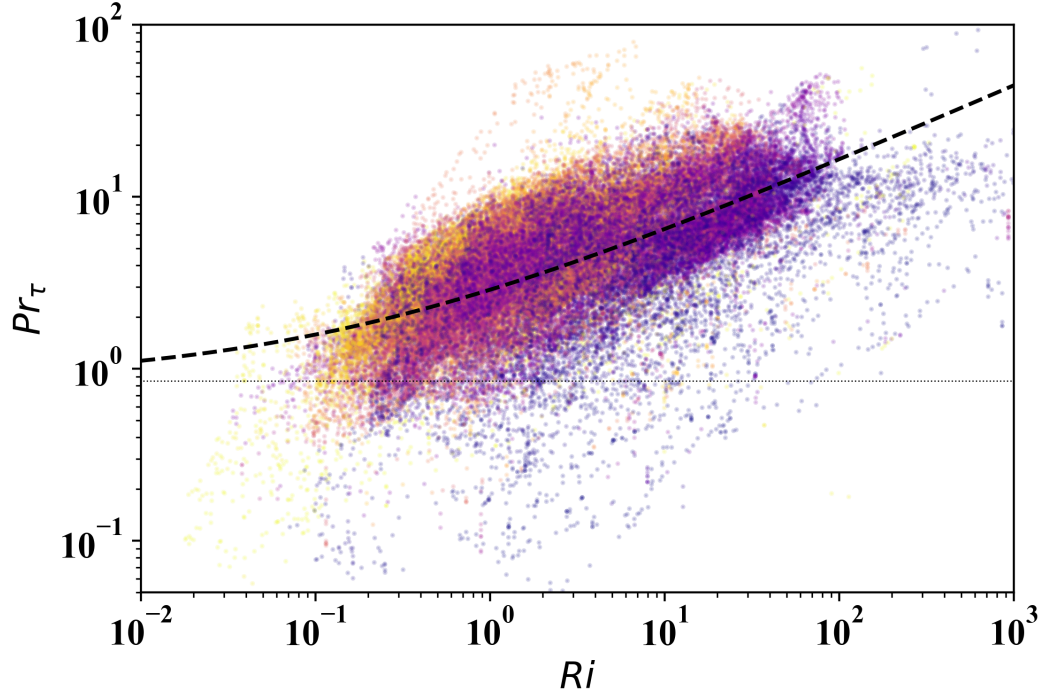


Figure 5.10:  $Pr_\tau$  spectral estimation. The black dashed line shows the empirical relationship  $Pr_\tau = 0.85 + 182.4/(PrRe^{0.888})^3$  with the small dotted line representing the limit,  $Pr_\tau = 0.85$ . Color mapping elevation is consistent with Fig. 5.9.

### 5.4.2 Influence of scaling laws

This sub-section is designed to take all previously demonstrated information from the GaTE system, inclusive of empirical models, scaling behavior, and data, and provide and explain a new model based on this understanding.

What is known so far:

1. Stratified turbulence mixing efficiency can be parameterized by the eddy turnover time per buoyant restoration time, represented either by  $\varepsilon/\nu N^2$  or  $Re_\tau/Ri$ <sup>4;40</sup>.
  - (a) This has been shown here with GaTE data to be true in liquid metals.
2. Because of the low molecular  $Pr$ , the  $Pr_\tau$  is expected to be larger than predicted by Reynolds analogy for slower flows<sup>13;63</sup>.
3. Stratified turbulence occurs below the sufficient criteria of  $Ri_f < 1$ . This is true for all fluids and flows<sup>9</sup> including liquid metal<sup>6</sup>.

None of this is surprising but the interpretation may not be intuitive. That is: there are certain stratified flows in liquid metal where the global  $Ri$  will be greater than unity (sometimes much greater) that still does not exhibit uniform stratified front behavior.

The explanation for this is that uniform stratification usually occurs under weak inertial forces since there is only so much density difference in natural or engineered temperature deltas. The strong damping of temperature fluctuations in liquid metal allows uniformity of the temperature front provided with a much larger inertial influence ( $Pe \ll Re$ ). This is seen in the inertial-diffusive sub-domain influence. What is interesting is that when input with enough inertia to finally overturn the front, the system is already at a high enough  $Re$  that the differing density eddies are relatively unaffected by buoyancy, dissipating their heat faster than buoyancy can act<sup>26</sup>. These make the behavior more passive (seen in the shortening of the Bolgiano microscale) when the critical  $Ri_f$  is reached.

To use this information to better model stratified turbulence in LFMRS, a combination of the empirical models already presented can be used, validated with the combined GaTE SWI-DTS and UDV systems and tied to the deeper physical understanding of turbulent microscales in an active, low  $Pr$  flow. Shown in Figure 5.11 are the eddy thermal diffusivity measurements. They are not normalized by  $Re_\tau/Ri$  or the modified model would consolidate into the original model (the region breakdown by Shih<sup>4</sup> is maintained); they are instead mapped against by the measured derived  $Ri$  ( $\frac{g\beta\sqrt{\langle(\partial\bar{T}/\partial z)^2\rangle}}{\langle(\partial w'/\partial z)^2\rangle}$ )(left) and the global  $Ri$  ( $\frac{g\beta\Delta T}{U^2}$ )(right). On each frame both models (original and modified) are shown. The modified version incorporates the notion of using  $Ri_f$  instead of  $Ri$ , only necessary as  $1/Pr$  increases.

Written out:

$$\hat{\kappa} = f \left[ I \frac{UD}{\nu} \frac{U^2}{g\beta\Delta TD} \left( 0.85 + 182.4 / \left( \frac{\nu}{\kappa} \left( \frac{UD}{\nu} \right)^{0.888} \right) \right) \right] = f \left[ I \frac{Re}{Ri} \left( 0.85 + \frac{182.4}{Pr Re^{0.888}} \right) \right] \quad (5.7)$$

where the function  $f$  is still defined by the original parameterization and the turbulence intensity,  $I$ , of 5-10% matches well with the GaTE's inlet impinging on the sealed UIS passing over a backwards step - further refinement may be required if the geometry is significantly different.

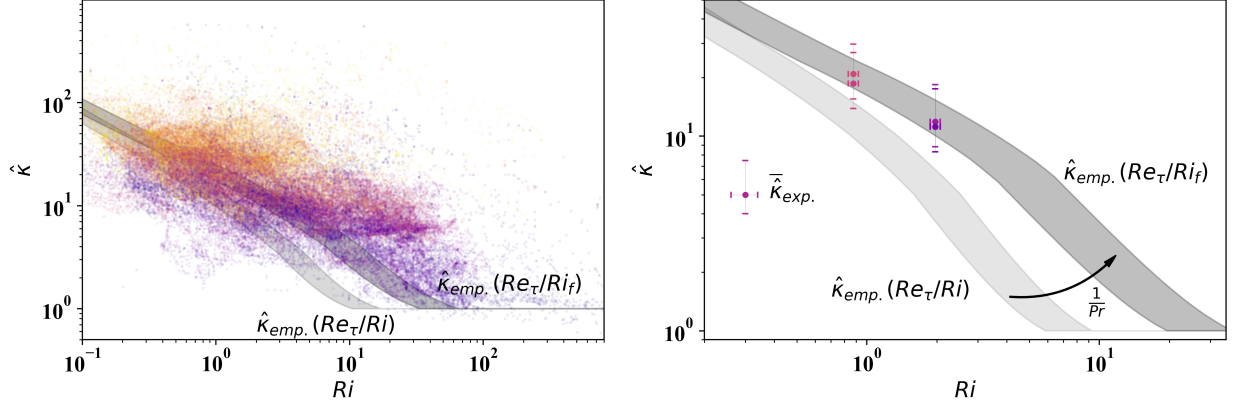


Figure 5.11: Eddy thermal diffusivity measurements by measured  $Ri$  ( $\frac{g\beta\sqrt{\langle(\partial T/\partial z)^2\rangle}}{\langle(\partial w/\partial z)^2\rangle}$ ) (left) and global average by global  $Ri$  ( $\frac{g\beta\Delta T}{U^2}$ ) (right) compared to the  $\hat{\kappa}$  functions of the empirical parameterization<sup>4</sup> ( $\hat{\kappa}_{emp.} = f(Re_\tau/Ri)$ ) and modified empirical expectation for use with liquid metal ( $\hat{\kappa}_{emp.} = f(Re_\tau/Ri_f) = f(Re_\tau Pr_\tau/Ri)$ ).

The models converge as  $Ri$  goes down ( $Re$  goes up) or as  $1/Pr$  goes down, returning  $Pr_\tau$  to the 0.85 limit. Where the transition to non-molecular thermal diffusion begins is a function of the passivity of liquid metal; the increased eddy diffusion is a function of the inertial-diffusive dominated spectrum, maintaining turbulent mixing in a calmer thermal field.

What is implied in the use of this model:

1. The strong thermal diffusion of low  $Pr$  fluids results in weaker influence of buoyant restorative forces (more passive). On the macroscale the baroclinic torque ( $\nabla P \times g\beta\nabla T$ ) is reduced by reducing the magnitude of the temperature gradient with strong diffusion. This is seen in the examination of the microscale, the maximum of a half-decade of observable  $Ri_x = 1$  conditions (or very short ‘active’ spectral region - Fig. 5.4).
2. Flux parameters (such as those in  $Pr_\tau$ ,  $Ri_f$ ) are capable of capturing this and the full effects of the turbulent energy budget, but are difficult to measure. Validated models, such as the two used in this chapter are required - Fig. 5.9 and 5.10.

## 5.5 Spectral synopsis

Two important, independent microscales help describe the temperature (and, for active turbulence, the velocity) dynamics in the GaTE scaled plenum. The BO59 scaling, between the integral microscales and the Bolgiano microscale, has been highlighted using the spectral Richardson number,  $Ri_x$ . The scaling law behavior is consistent with BO59 for velocity  $w'$ , temperature  $T'$ , and  $w'T'$  in this region. However, the region can be truncated in liquid metal by another important and unique scale, the thermal microscale. At scales smaller than the thermal microscale, the inertial-diffusive range dictates the scaling showing both scaling exponents expected from theory, Gibson's<sup>75</sup>  $-9/3$  and BHT59's<sup>67</sup>  $-17/3$  at smaller scales.

The impact of global parameters on these microscopic scales has been observed due to the GaTE's UDV and SWI-DTS system's ability to measure all elevations simultaneously. Experimental data agrees well with previously hypothesized theories for both sets of scaling ranges (BO59, inertial-diffusive). Although no new theoretical framework has been developed from the data, confirmation of existing theory gives confidence in the ability to use this spectral data for estimation of turbulence quantities, namely the experimentally quantified eddy thermal diffusivity.

Estimates derived from spectra integrated variables have been mapped and are in agreement with the empirical mixing efficiency of Chapter 2 when parameterized by turbulence quantity  $Re_\tau/Ri$ . The influence of liquid metal dynamics modifies this behavior, captured by the empirical  $Pr_\tau$  model of Chapter 4 which estimates eddy thermal diffusivities higher than what would be expected of a fluid of  $Pr \sim 1$ . This is attributed to the sustained turbulent action of the momentum in the inertial-diffusive governed flows, increasing the eddy thermal diffusivity despite relatively calm thermal behavior.

# Chapter 6

## Conclusions

Thermal stratification of liquid metal in pool type LMFBRs complicates the design of these reactors. Understanding this behavior is required to improve the accuracy of safety analysis codes. Observations on thermal stratification in liquid metal have been obtained by developing a scaled-down experimental facility, the Gallium Thermal-hydraulic Experiment. This work presents the scaling analysis performed to achieve this design, the design of the system and use of specialized distributed temperature and velocity sensors, the experiments used to capture the pertinent phenomena, and detailed evaluation of the thermal stratification using turbulent spectra.

Throughout this dissertation, the eddy thermal diffusivity,  $\kappa_\tau$ , is used as a way to parameterize and explain the unique physics of stably stratified liquid metal turbulence. First used as an output parameter in the design of the scaled system to quantify scaling distortion, through to its experimental measurement. This is paired, through their ratio in the turbulent Prandtl number,  $Pr_\tau$ , to the momentum eddy diffusivity. From a macroscopic viewpoint, the value of  $Pr_\tau$  is a fundamentally unique aspect of liquid metal flows; even in moderately high  $Re$  flows, the value of  $Pr_\tau$  can be greater than 1. The very strong molecular thermal diffusivity of the liquid metal acts as a low-pass filter and damps out high frequency fluctuations, skewing the ratio of eddy diffusivities in favor of a relatively smaller  $\kappa_\tau$ .

Liquid metal exhibits another unique feature important to the study of mixed convection: the strong molecular diffusivity weakens buoyant energy dissipation and tilts the ratio of buoyant suppression to inertial generation of turbulent kinetic energy. This ratio is quantified by the flux Richardson number,  $Ri_f$ , where the global balance of forces,  $Ri$ , is equated by product of  $Pr_\tau$  ( $Ri = Pr_\tau Ri_f$ ). With a critical value at  $Ri_{f,crit} = 1$  and a  $Pr_\tau > 1$ , the critical global balance in liquid metal then is  $Ri_{crit} > 1$ . On a macro-scale, diffusivity in the horizontal direction weakens the baroclinic torque; on a micro-scale, the low-pass cutoff for thermal fluctuations can occur below the restorative buoyant turnover time, leaving a smaller portion of the spectrum capable of acting with gravity.

Exploration from the spectral viewpoint is investigated. A theoretical framework for turbulent scaling laws in liquid metal (or other low  $Pr$  fluids), the expected deviations from the isotropic assumptions in K41's -5/3 law, is outlined with experimental validation. A

small active spectral region consistent with theory is highlighted using Bolgiano's spectral  $Ri$ . Truncation by the thermal microscale and the inertial-diffusive region, a unique feature of liquid metal scalar mixing, reduces the active region and damps out higher frequency fluctuations in the temperature.

Direct observations of these phenomena are possible with the use of the specialized distributed sensors. Measurements of the fluctuations (e.g.  $w'$ ,  $T'$ ) and the gradients (e.g.  $\partial T/\partial z$ ) estimate  $\kappa_\tau$  ( $= \overline{w'T'}/\frac{\partial T}{\partial z}$ ) and other important turbulent flux parameters ( $Pr_\tau$ ,  $Ri_f$ ). In doing so, validation of an empirical framework, laid out throughout the dissertation, is possible. Together, these validated models provide a tool for estimating both the relative mixing efficiency and the critical global stability of a liquid metal system based on global parameters. This link between the underlying physics, the global inputs to a liquid metal system, and the critical outputs provides one of the necessary stepping blocks for evaluating aspects of LMFR safety.

# Bibliography

- [1] Y.I. Chang, P.J. Finck, C. Grandy, J. Cahalan, L. Deitrich, F. Dunn, D. Fallin, M. Farmer, T. Fanning, T. Kim, et al. Advanced burner test reactor preconceptual design report. Technical report, Argonne National Laboratory (ANL), 2008.
- [2] B. Ward, A. Wiley, G. Wilson, and H. Bindra. Scaling of thermal stratification or mixing in outlet plena of sfrs. *Annals of Nuclear Energy*, 112(1):431–438, 2018.
- [3] M. Jischa and H.B. Rieke. About the prediction of turbulent prandtl and schmidt numbers from modeled transport equations. *Int. J. Heat Mass Transfer*, 22:1547–1555, 1978.
- [4] Lucinda H Shih, Jeffrey R Koseff, Gregory N Ivey, and Joel H Ferziger. Parameterization of turbulent fluxes and scales using homogeneous sheared stably stratified turbulence simulations. *Journal of Fluid Mechanics*, 525:193–214, 2005.
- [5] Vibhav Durgesh, Jim Thomson, Marshall C Richmond, and Brian L Polagye. Noise correction of turbulent spectra obtained from acoustic doppler velocimeters. *Flow Measurement and Instrumentation*, 37:29–41, 2014.
- [6] B. Ward, J. Clark, and H. Bindra. Thermal stratification in liquid metal pools under influence of penetrating colder jets. *Experimental Thermal and Fluid Science*, 103: 118–125, 2019.
- [7] Dan Gabriel Cacuci. *Handbook of Nuclear Engineering: Vol. 4: Reactors of Generations III and IV*, volume 2. Springer Science & Business Media, 2010.
- [8] D Tenchine. Some thermal hydraulic challenges in sodium cooled fast reactors. *Nuclear Engineering and Design*, 240(5):1195–1217, 2010.

- [9] P. Kundu, I. Cohen, and H. Hu. *Fluid Mechanics*. Elsevier, 3rd ed. edition, 2004.
- [10] J.S. Turner. *Buoyancy Effects in Fluids*. Cambridge University Press, 1973.
- [11] T.R. Osborn. Estimates of the local rate of vertical diffusion from dissipation measurements. *Journal of Physical Oceanography*, 10(1):83–89, 1980.
- [12] J.E. Simpson. *Gravity Currents: In the Environment and the Laboratory*. In the Environment and the Laboratory. Cambridge University Press, 1997. ISBN 9780521664011.
- [13] W.M. Kays. Turbulent prandtl number-where are we? *Journal of Heat Transfer*, 1994.
- [14] L.A. Glasgow. *Transport Phenomena: An Introduction to Advanced Topics*. Wiley, 2010. ISBN 9780470626603.
- [15] S. N. Singh. Heat transfer by laminar flow in a cylindrical tube. *Applied Scientific Research*, 7(5):325–340, 1958. doi: 10.1007/bf03184993.
- [16] Andrey Nikolaevich Kolmogorov. The local structure of turbulence in incompressible viscous fluid for very large reynolds numbers. *Cr Acad. Sci. URSS*, 30:301–305, 1941.
- [17] Stanley Corrsin. On the spectrum of isotropic temperature fluctuations in an isotropic turbulence. *Journal of Applied Physics*, 22(4):469–473, 1951. doi: 10.1063/1.1699986.
- [18] T H Fanning and T Sofu. Modeling of thermal stratification in sodium fast reactor outlet plenums during loss of flow transients, Dec 2009.
- [19] Sundar Namala, Rizwan-Uddin, and Tyler Sumner. Modelling thermal stratification in upper plenum of sodium fast reactor using systems code sas4a/sassys-1 and using cfd. *18th International Topical Meeting on Nuclear Reactor Thermal Hydraulics (NURETH-18)*, 2019.
- [20] K. Huber and J. W. Thomas. Coupled calculations of sas 4 a / sassys-1 and star-ccm + for the shrt-45 r test in ebr-ii. 2015.

- [21] Y. Ieda, I. Maekawa, T. Muramatsu, and S. Nakanishi. Experimental and analytical studies of the thermal stratification phenomenon in the outlet plenum of fast breeder reactors. *Nuclear engineering and design*, 120(2-3):403–414, 1990.
- [22] N. Kimura, H. Miyakoshi, and H. Kamide. Experimental study on thermal stratification in a reactor vessel of innovative sodium-cooled fast reactor mitigation approach of temperature gradient across stratification interface. *Journal of Nuclear Science and Technology*, 47(9):829–838, Jan 2012.
- [23] G. Grotzbach. Challenges in low-prandtl number heat transfer simulation and modelling. *Nuclear Engineering and Design*, 264:41–55, 2013.
- [24] Ali Haghiri and Richard D Sandberg. Large eddy simulations of wall jets with coflow for the study of turbulent prandtl number variations and data-driven modeling. *Physical Review Fluids*, 5(6):064501, 2020.
- [25] F. Roelofs, editor. *Thermal Hydraulics Aspects of Liquid Metal Cooled Nuclear Reactors*. Elsevier, 2019. doi: 10.1016/c2016-0-01216-0.
- [26] Laura Cope, P. Garaud, and Colm-cille Caulfield. The dynamics of stratified horizontal shear flows at low pécelet number. 11 2019.
- [27] Rajneesh Chaudhary, C Ji, Brian G Thomas, and SP Vanka. Transient turbulent flow in a liquid-metal model of continuous casting, including comparison of six different methods. *Metallurgical and Materials Transactions B*, 42(5):987–1007, 2011.
- [28] S. Moriya, N. Tanaka, N. Katano, and A. Wada. Effects of reynolds number and richardson number on thermal stratification in hot plenum. *Nuclear Engineering and Design*, 99:441–451, 1987.
- [29] M. Puustinen, J. Laine, and R. Antti. Ppoolex experiments on thermal stratification and mixing. Technical report, NKS, 2009.

- [30] N. Tanaka, S. Moriya, S. Ushijima, T. Koga, and Y. Eguchi. Prediction method for thermal stratification in a reactor vessel. *Nuclear Engineering and Design*, 120:395–405, 1990.
- [31] M. Uotani. Natural convection heat transfer in thermally stratified liquid metal. *Journal of Nuclear Science and Technology*, 24(6):442–451, June 1987.
- [32] R. Vidil, D. Grand, and F. Leroux. Interaction of recirculation and stable stratification in a rectangular cavity filled with sodium. *Nuclear Engineering and Design*, 105:321–332, 1988.
- [33] T.H. Fanning and et al. *International Conference on Fast Reactors and Related Fuel Cycles*, December 2009.
- [34] IAEA Report. Book of extended synopsis. Technical report, International Conference on Fast Reactors and Related Fuel Cycles, Kyoto, Japan, 2009.
- [35] Novak Zuber, Gary E Wilson, Mamoru Ishii, Wolfgang Wulff, BE Boyack, AE Dukler, P Griffith, JM Healzer, RE Henry, JR Lehner, et al. An integrated structure and scaling methodology for severe accident technical issue resolution: Development of methodology. *Nuclear Engineering and Design*, 186(1):1–21, 1998.
- [36] T. Aoki and et al. Experimental study on thermal stratification, proc. iaea specialists’ meeting. 1982.
- [37] Ronald L. Panton. *Incompressible Flow*, volume 4. John Wiley & Sons, Inc., 2013.
- [38] Tadao Aoki, Hideo Atsumo, and O-Arai Engrg Center. Thermal stratification test program in japan. In *Proc. IAEA Specialists’ Meeting, Internat. Working Group on Fast Reactors, Grenoble*, 1982.
- [39] R Byron Bird, Warren E Stewart, and Edwin N Lightfoot. *Transport phenomena*. John Wiley & Sons, 2007.

- [40] GN Ivey, KB Winters, and JR Koseff. Density stratification, turbulence, but how much mixing? *Annual Review of Fluid Mechanics*, 40, 2008.
- [41] Subhas K Venayagamoorthy and Jeffrey R Koseff. On the flux richardson number in stably stratified turbulence. *Journal of Fluid Mechanics*, 798, 2016.
- [42] B. Weigand, J.R. Ferguson, and M.E. Crawford. An extended kays and crawford turbulent prandtl number model. *International journal of heat and mass transfer*, 40(17):4191–4196, 1997.
- [43] Francois Bertin, Jean Barat, and Richard Wilson. Energy dissipation rates, eddy diffusivity, and the prandtl number: An in situ experimental approach and its consequences on radar estimate of turbulent parameters. *Radio Science*, 32(2):791–804, 1997.
- [44] K YM Lai, M Salcudean, S Tanaka, and R IL Guthrie. Mathematical modeling of flows in large tundish systems in steelmaking. *Metallurgical and Materials Transactions B*, 17(3):449–459, 1986.
- [45] P.F. Peterson. Scaling and analysis of mixing in large stratified volumes. *International Journal of Heat and Mass Transfer*, 37:97–106, 1994.
- [46] M. Aydin, S. Huang, and T.A. Lipo. Axial flux permanent magnet disc machines: A review. Technical report, Wisconsin Electric Machines and Power Electronics Consortium, 2004.
- [47] E.J. Williams. The induction of electromotive forces in a moving liquid by a magnetic field, and its application to an investigation of the flow of liquids. *Proceedings of the Physical Society*, 42(5):466, 1930.
- [48] J.A. Shercliff. *The theory of electromagnetic flow-measurement*. CUP Archive, 1962.
- [49] O J Foust. Sodium-nak engineering handbook. volume iii. sodium systems, safety, handling, and instrumentation. [lmfbr]. 1 1978.

- [50] S. Lomperski, C. Gerardi, and W. D. Pointer. Fiber optic distributed temperature sensor mapping of a jet-mixing flow field. *Experiments in Fluids*, 56(3):55, Mar 2015.
- [51] C Tompkins, M Corradini, and M Anderson. Temperature profiles and mixing in a natural-circulation cooling facility via distributed optical sensors. *Nuclear Technology*, 196(2):346–354, 2016.
- [52] Katrien Van Tichelen, Graham Kennedy, Fabio Mirelli, Alessandro Marino, Antonio Toti, Davide Rozzia, Edoardo Cascioli, Steven Keijers, and Philippe Planquart. Advanced liquid-metal thermal-hydraulic research for myrrha. *Nuclear Technology*, 206(2):150–163, 2020.
- [53] James Schneider and Mark Anderson. Using optical fibers to examine thermal mixing of liquid sodium in a pool-type geometry. *International Journal of Heat and Mass Transfer*, 158:119968, 2020.
- [54] Brendan Ward, Broderick Sieh, and Hitesh Bindra. Experimental measurement of liquid metal flow fields in a scaled sfr upper plenum. *18th International Topical Meeting on Nuclear Reactor Thermal Hydraulics (NURETH-18)*, 2019.
- [55] Willemetz. Dop4000 users manual. Technical report, Signal Processing S.A. - Switzerland, 2019.
- [56] Daniel Brito, Henri-Claude Nataf, Philippe Cardin, Julien Aubert, and Jean-Paul Masson. Ultrasonic doppler velocimetry in liquid gallium. *Experimental Fluids*, 31(6):653–663, 2001.
- [57] Yuji Tasaka, Yasushi Takeda, and Takatoshi Yanagisawa. Ultrasonic visualization of thermal convective motion in a liquid gallium layer. *Flow Measurement and Instrumentation*, 19(3-4):131–137, 2008.
- [58] A Cramer, C. Zhang, and S. Eckert. Local flow structures in liquid metals measured by ultrasonic doppler velocimetry. *Flow Measurement and Instrumentation*, 15(3):145–153, 2004.

- [59] A Downs. *Geophysical Fluid Dynamics*. New York: Blackie Academic and Professional, 1993.
- [60] Philip VanWiltburg. Mitigation of emi generated by a variable-frequency-drive controller for an ac induction motor. 1994.
- [61] Brendan Ward, Thomas Hopkins, and Hitesh Bindra. Experimental validation of cfd models capturing the thermal-hydraulics in liquid metal cooled reactor plena. *Proceedings of 28th International Conference on Nuclear Engineering (ICONE28)*, 2020.
- [62] Hitesh Bindra, Pablo Bueno, Jeffrey F Morris, and Reuel Shinnar. Thermal analysis and exergy evaluation of packed bed thermal storage systems. *Applied Thermal Engineering*, 52(2):255–263, 2013.
- [63] W.M. Kays and M.E. Crawford. *Convective Heat and Mass Transfer*, volume 3rd. Ed. McGraw-Hill, 1993.
- [64] N. Kasagi, Y. Ohtsubo, and Y. Tomita. *Eighth Symposium on Turbulent Shear Flows, Tech. Univ. of Munich*, Sept. 1991.
- [65] R Bolgiano Jr. Turbulent spectra in a stably stratified atmosphere. *Journal of Geophysical Research*, 64(12):2226–2229, 1959.
- [66] AM Obukhov. Temperature field structure in a turbulent flow. *Izv. Acad. Nauk SSSR Ser. Geog. Geofiz*, 13:58–69, 1949.
- [67] GK Batchelor, ID Howells, and AA Townsend. Small-scale variation of convected quantities like temperature in turbulent fluid part 2. the case of large conductivity. *Journal of Fluid Mechanics*, 5(1):134–139, 1959.
- [68] Detlef Lohse and Ke-Qing Xia. Small-scale properties of turbulent rayleigh-bénard convection. *Annual Review of Fluid Mechanics*, 42, 2010.
- [69] Qi Zhou. Far-field evolution of turbulence-emitted internal waves and reynolds number effects on a localized stratified turbulent flow. 2015.

- [70] Geert Brethouwer, Paul Billant, Erik Lindborg, and Jean-Marc Chomaz. Scaling analysis and simulation of strongly stratified turbulent flows. 2007.
- [71] Erik Lindborg. The energy cascade in a strongly stratified fluid. *Journal of Fluid Mechanics*, 550:207, 2006.
- [72] AS Monin and AM Iaglom. Statistical fluid mechanics: Mechanics of turbulence. volume 2/revised and enlarged edition. *mit*, 1975.
- [73] Mahendra K Verma. *Energy transfers in fluid flows: multiscale and spectral perspectives*. Cambridge University Press, 2019.
- [74] Carl H Gibson. Fine structure of scalar fields mixed by turbulence. i. zero-gradient points and minimal gradient surfaces. *The Physics of Fluids*, 11(11):2305–2315, 1968.
- [75] Carl H Gibson. Fine structure of scalar fields mixed by turbulence. ii. spectral theory. *The Physics of Fluids*, 11(11):2316–2327, 1968.
- [76] Carl H Gibson. Zero gradient points in turbulent mixing. In *Structure and Mechanisms of Turbulence II*, pages 347–352. Springer, 1978.
- [77] John Parley Clay. Turbulent mixing of temperature in water, air and mercury. 1974.
- [78] S Cioni, S Ciliberto, and J Sommeria. Temperature structure functions in turbulent convection at low prandtl number. *EPL (Europhysics Letters)*, 32(5):413, 1995.
- [79] Till Zürner, Felix Schindler, Tobias Vogt, Sven Eckert, and Jörg Schumacher. Combined measurement of velocity and temperature in liquid metal convection. *Journal of Fluid Mechanics*, 876:1108–1128, August 2019. doi: 10.1017/jfm.2019.556.
- [80] Spectral analysis. *UH Currents Group*, 2020.
- [81] GK Batchelor. The conditions for dynamical similarity of motions of a frictionless perfect-gas atmosphere. *Quarterly Journal of the Royal Meteorological Society*, 79(340): 224–235, 1953.

- [82] Stephen B. Pope. *Turbulent Flows*. Cambridge University Press, August 2000. doi: 10.1017/cbo9780511840531.
- [83] Eugene A. Avallone, Theodore Baumeister, and Ali Sadegh. *Marks' Standard Handbook For Mechanical Engineers (Standard Handbook for Mechanical Engineers)*. McGraw-Hill Professional, 2006. ISBN 0071428674.
- [84] M.G. Hvasta, W.K. Nollet, and M.H. Anderson. Designing moving magnet pumps for high-temperature, liquid-metal systems. *Nuclear Engineering and Design*, 327:228 – 237, 2018. ISSN 0029-5493. doi: <https://doi.org/10.1016/j.nucengdes.2017.11.004>.
- [85] Christian Poelma. Ultrasound imaging velocimetry: a review. *Experiments in Fluids*, 58(1):3, 2017.
- [86] Babak Khorsandi, Laurent Mydlarski, and Susan Gaskin. Noise in turbulence measurements using acoustic doppler velocimetry. *Journal of Hydraulic Engineering*, 138(10): 829–838, 2012.
- [87] Derek G. Goring and Vladimir I. Nikora. Despiking acoustic doppler velocimeter data. *Journal of Hydraulic Engineering*, 128(1):117–126, Jan 2002. doi: 10.1061/(asce)0733-9429(2002)128:1(117).
- [88] Tony L Wahl. Discussion of “Despiking acoustic doppler velocimeter data” by derek g. goring and vladimir i. nikora. *Journal of Hydraulic Engineering*, 129(6):484–487, 2003.
- [89] Minnan Liu, Nallamuthu Rajaratnam, and David Z Zhu. Turbulence structure of hydraulic jumps of low froude numbers. *Journal of Hydraulic Engineering*, 130(6):511–520, 2004.
- [90] Bahareh Doroudian, Fereshteh Bagherimiyab, and Ulrich Lemmin. Improving the accuracy of four-receiver acoustic doppler velocimeter (adv) measurements in turbulent boundary layer flows. *Limnology and Oceanography: Methods*, 8(11):575–591, 2010.

# Appendix A

## Moving magnet pump characterization

To quantify the pump's output for use in SAS4A/SASSYS-1, characteristic curves were required to be developed. Ideally, affinity law or affinity-like law scaling should be developed to help in understanding transients like pump coast-down. The scaling is dependent on relationships between total developed head ( $H$ ), flowrate ( $Q$ ), and (for a centrifugal pump) impeller speed ( $N$ ):

$$\left(\frac{N}{N_0}\right) = \left(\frac{Q}{Q_0}\right)^n = \left(\frac{H}{H_0}\right)^m \quad (\text{A.1})$$

where  $n$  and  $m$  are 1 and 2, respectively, for centrifugal pumps (within limit<sup>83</sup>). Identifying these scaling quantities for the GaTE's pump is the goal here but to develop these from theory, more understanding is required.

The GaTE moving magnet pump is a disc-type design: the pump has two discs embedded with permanent magnets in an alternating array encompassing the gallium tubing on top and bottom<sup>46</sup>. This is shown pictorially in Fig. A.1. There are two flow paths (essentially two pumps) that can be modeled the same and the discussion is identical. So, for the sake of brevity, only the 1" data are shown. The discs are rotated using a motor controlled by a variable frequency drive (VFD). The VFD controls the speed of the motor with proximity probe feedback to ensure a reliable rotational frequency. As the speed of the permanent magnets increases, the speed of the diamagnetically opposed gallium in the tube will also

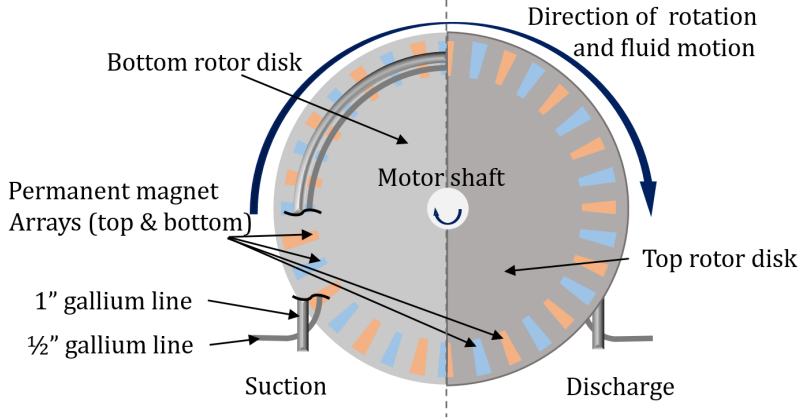


Figure A.1: Pictorial representation of the disc-type moving magnet pump.



Figure A.2: Suction (inlet) flanges of the GaTE pump.

increase<sup>47</sup>. The roughly sinusoidal<sup>84</sup> magnetic field frequency is linearly dependent on the frequency of pump rotation.

Neglecting the other parameters (as they are fixed for the GaTE system) such as air gap thickness, field strength, magnet pitch, magnet radius, gallium electrical conductance and magnetic permeability, and a slew of geometry constraints (rotor radius, etc.) greatly simplifies the problem. This leaves the pressure that the pump can output only a linear function of frequency:

$$\Delta P = f(\omega) = C\omega \quad (\text{A.2})$$

where  $C$  is the constant to lump all of the other parameters. Clearly then, the exponent in an affinity-like law for speed ratio vs total developed head ratio (or pressure) must be 1:

$$\left(\frac{N}{N_0}\right) = \left(\frac{H}{H_0}\right)^1.$$

However, losses in the pump (which are predominantly fluid friction) will cause this to deviate, as a function of flowrate. Then:

$$\Delta P(Q) = C\omega - (f_D + K)\frac{\rho V^2}{2} \frac{L}{D} \quad (\text{A.3})$$

where the new parameters ( $f_D, \rho, V, L, D$ ) are all from the Darcy-Weisbach equation, where  $f_D$  can be solved for using the Colebrook equation, and  $K$ , the pressure drop coefficient, was added to account for the pipe bending around the radius of the pump (and the other turns it makes - see for example in Fig. A.2). In this case, the flow dependence on rotational speed is a straightforward relationship dependent only on the internal friction of a pipe - an easily estimated quantity: a function of the velocity (or flowrate, by continuity) squared. Then the exponent  $n$  from relationship A.1 is 2:  $\left(\frac{N}{N_0}\right) = \left(\frac{Q}{Q_0}\right)^2$ . An  $m$ - $n$  reversal from centrifugal pump performance.

In order to test this,  $C$  and  $K$  must be determined, the only parameters that cannot be easily estimated. For this, generation of a pump curve (head, flow) was required. It was fit using a set of data for a rotational speed of 401rpm. The fitted  $C$  and  $K$  were used to draw new ‘affinity’ lines from the 401rpm curve. The original 401rpm curve data, the fitted curve, the new ‘affinity’ curves, and the associated data from those pump rotational speeds are all shown in Figure A.3.

The only note worth mentioning further: there is a pattern of deviation as the rotational speed is increased and the system flow is restricted where the output pressure is lower than expected. In the determination for these curves it was assumed that the losses in the pump were due to fluid friction only; however, from experience it is known that the output of the pump can warm significantly at the faster rotational speeds (implying more than just fluid friction but also inefficiency in the EM mechanisms as well).

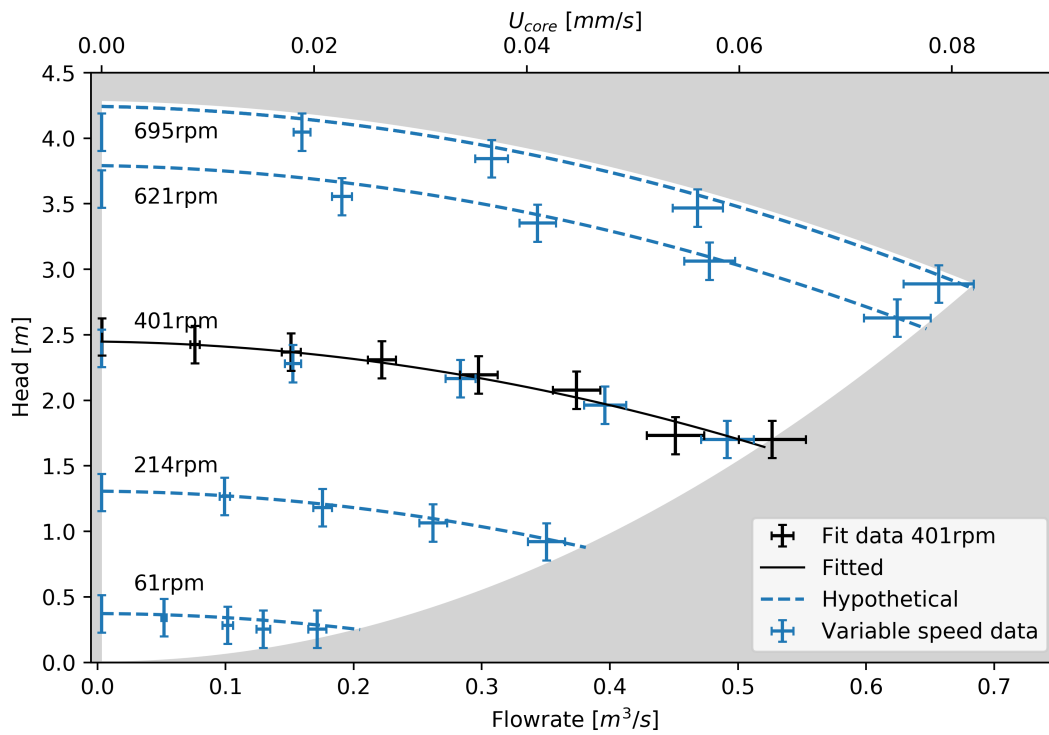


Figure A.3: The GaTE characteristic curves: pump and system limits. Pump affinity curves using  $\left(\frac{N}{N_0}\right) = \left(\frac{Q}{Q_0}\right)^2 = \left(\frac{H}{H_0}\right)^1$

# Appendix B

## EMFM Calibration

Calibration of the EMFM was accomplished by comparing an observed volumetric flowrate of a calibration cylinder with respect to the voltage output simultaneously obtained by the EMFM.

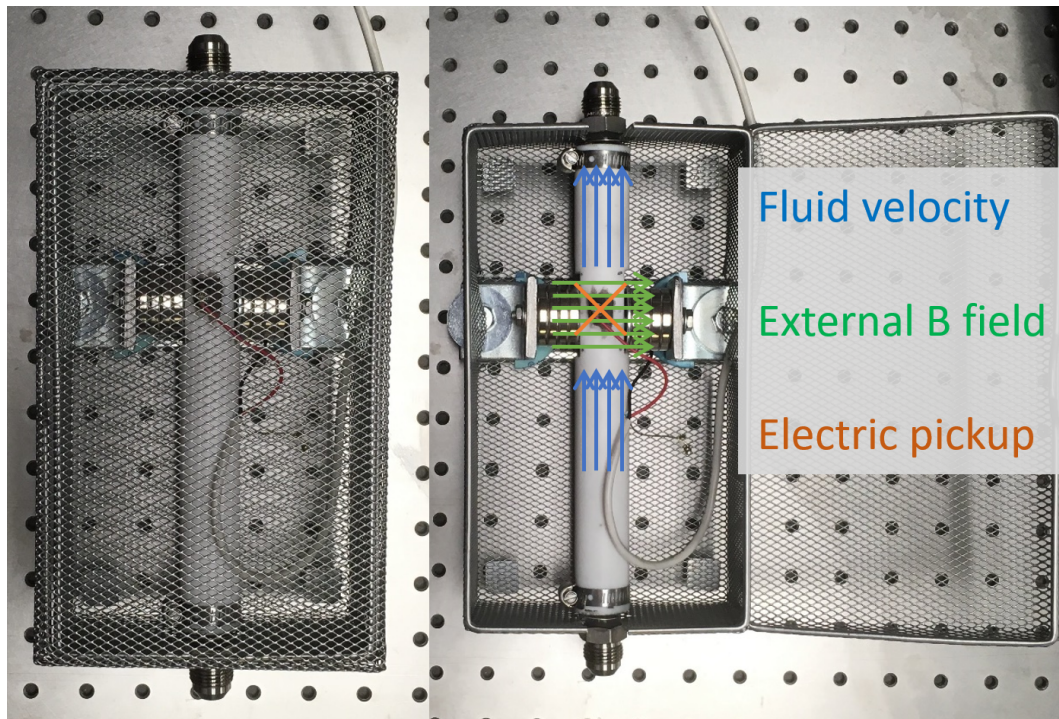


Figure B.1: GaTE electromagnet flow meter: teflon pipe, grounded cage, and permanent magnet construction. Electric pickups measure the orthogonal emf as the conductive fluid moves through the transverse magnetic field. The pipe ID (and pickup screw distance) is 0.5", increasing the local velocity to produce a larger emf.

The system was reconfigured such that the only flow path between the calibration cylinder and the plenum was through the EMFM. This is shown in Figure B.2. The filling procedure was modified to ensure compressible gases were not present during the tests. The core was heated by its oil circulator, maintained at a temperature of 50°C to avoid changes in density during the prolonged testing.

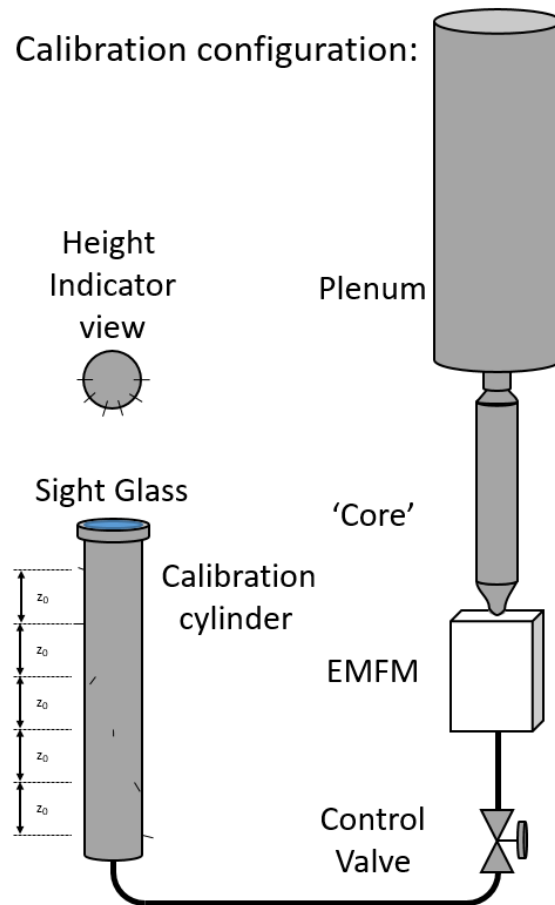


Figure B.2: Calibration cylinder details and flow path.

For each test the calibration cylinder started at the highest liquid level, given the inventory in the system. A gas valve was opened to allow the top surface to be pressurized - forcing the gallium down the calibration cylinder, through the EMFM, and into the empty plenum. As the gallium level in the calibration cylinder reached below the second lowest height indicator, the pressure was vented, and the cylinder was allowed to fill back up.

Video of each test was recorded while the EMFM voltage was read. The video was used to determine timing of the important events (e.g. initial pressurization, the time the liquid

level reached an indicator, etc.). The time between indicators of known spacing (i.e. volume) allowed computation of the average volumetric flow rate in that section of the calibration cylinder. However, since only the average could be computed, a functional extrapolation needed to be used. For the system being modelled, Bernoulli's equation with substitution of  $\dot{h}$  for velocity, can be used to determine the behavior of the liquid level as a function of time:  $h(t) + \frac{P}{\gamma} + \frac{\dot{h}(t)^2}{2g} + K \frac{\dot{h}(t)^2}{2g} = C = H_0 + \frac{P_1}{\gamma} + 0$  allows us to solve the differential equation for liquid level height:  $h(\mathbf{t}) = -(\frac{P_2}{\gamma}) \pm \sqrt{\frac{g(1+K)}{2} c_1 \mathbf{t} - \frac{1}{4} c_1^2 + C - \frac{g\mathbf{t}^2}{2(1+K)}}$  which yields a solution dependent on initial conditions, pressure differences, and the system's resistance to flow. Differentiating shows that the liquid level in the calibration cylinder should change linearly with time with a step change in pressure:

- filling of system from calibration cylinder

$$\dot{h}(\mathbf{t}) = \sqrt{2g(1+K)\left(\frac{P-P_0}{\gamma}\right)} - \frac{g\mathbf{t}}{1+K} \quad (\text{B.1})$$

- draining of system from calibration cylinder

$$\dot{h}(\mathbf{t}) = \sqrt{2g(1+K)(H_f - H_0)} - \frac{g\mathbf{t}}{1+K} \quad (\text{B.2})$$

The procedure for determining the constant of proportionality between flow rate and EMFM voltage is then as follows:

1. For each test use the recorded videos to determine when the liquid level reaches each indicated height (event).
2. Use the event timing and known volume to compute the average volumetric flow rate for at least two segments of the calibration cylinder.
3. Determine a line from the two averaged flow rates and convert to the corresponding characteristic velocity for the EMFM internal diameter (this assumes incompressibility of the gallium/system).
4. Use a regression optimization to determine the constant of proportionality, " $C_i$ ", between the recorded EMFM voltage and the calculated EMFM velocity. (Eg. Fig. B.3)

- Do this for a randomly selected half of the tests and determine the calibration constant for each.

This calibration set attempted to span the range of flowrates seen during normal GaTE operation. To accomplish this, different pressures were used to generate the push as well as different system resistances to slow down the flow. The averaged calibration constant, representing the variation between-test uncertainty, and shown in Fig. B.4 is:

$$C \approx \text{Mean}(C) + \text{RMSE}(C) = 304258 \pm 3306 \text{ [mm/s / V]}.$$

- This averaged constant was then applied to the remaining tests and the root mean square deviation between each tested calibration cylinder flow rate and the  $\text{EMFM} * C_{\text{average}}$  was determined.

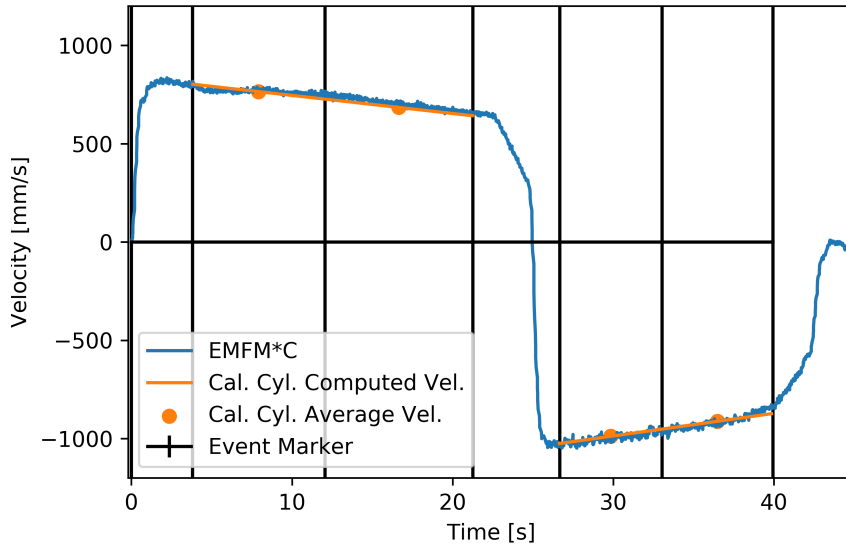


Figure B.3: Determination of calibration cylinder velocity (dots, solid lines); the corresponding EMFM output (multiplied by C factor) is shown for reference.

This procedure includes the following sources of uncertainty:

- DAQ electronic noise
- Variation from linear fit within-test
- Variation between-tests
- Uncertainty in timing the calibration cylinder events

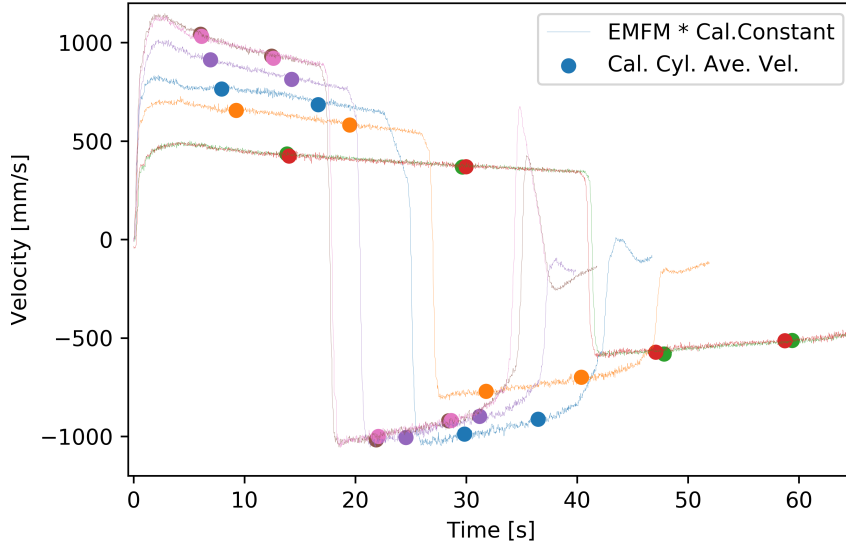


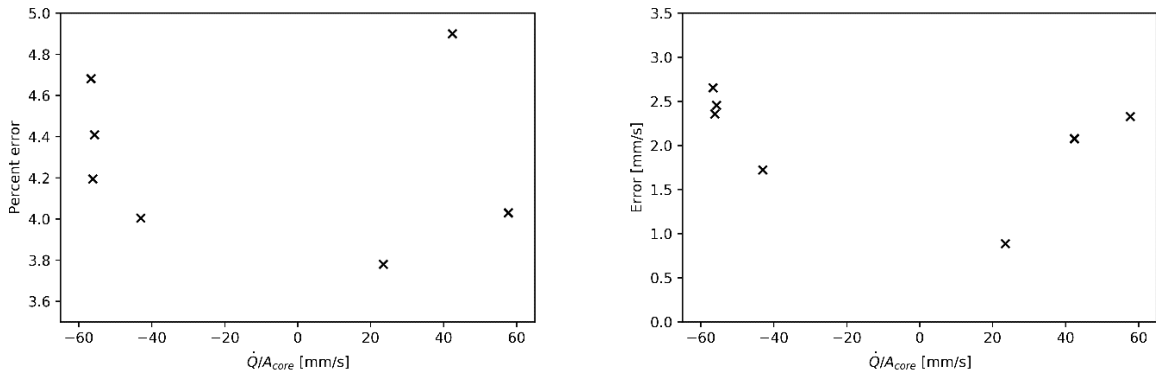
Figure B.4: Multiple tests were ensembled to determine the calibration constant (with a random half of the tests) while the other half were compared to the calibration constant to determine statistical agreement.

- Uncertainty of the volume between event markers

The first three sources are confounding and represents the uncertainty associated with the comparison of the calibration cylinder data to the EMFM output. The final two sources represent the uncertainty associated with the calibration cylinder data itself. The timing of events from the video are associated with determining which of two frames (of a 30 fps video) correspond to the level reaching that marker.

- $\bar{Q} = \frac{A(x_1 - x_2)}{(t_1 - t_2)}$
- $\sigma_Q = \sqrt{\left(\left(\frac{-A(x_1 - x_2)}{(t_2 - t_1)^2}\right)\sigma_{t,1}\right)^2 + \left(\left(\frac{-A(x_1 - x_2)}{(t_2 - t_1)^2}\right)\sigma_{t,2}\right)^2 + \left(\left(\frac{A}{(t_2 - t_1)}\right)\sigma_{x,1}\right)^2 + \left(\left(\frac{A}{(t_2 - t_1)}\right)\sigma_{x,2}\right)^2}$
- $\sigma_{x,1} = \sigma_{x,2} = 1/16[\text{in}]; \sigma_{t,1} = \sigma_{t,2} = 2/30[\text{s}]; (x_1 - x_2) = L = 4[\text{in}]$
- $\sigma_Q = \sqrt{\frac{2A^2L^2\sigma_t^2}{(\Delta t)^4} + \frac{2A^2\sigma_x^2}{(\Delta t)^2}} \therefore \max(\sigma_Q) = 3.3 \times 10^{-6} \text{ m}^3/\text{s}; \min(\sigma_Q) = 1.1 \times 10^{-6} \text{ m}^3/\text{s};$
- This corresponds to a percent uncertainty of 3.6 and 3.4 respectively

Multiplication of the calibration correction to the observed flow rates requires addition of the RMSE from each of the tests to capture the first three uncertainty terms determined from



(a) Percent error of the calibrated EMFM. (b) Absolute error of the calibrated EMFM.

Figure B.5: EMFM error quantification from the calibration.

the regression analysis. The total % uncertainty for the EMFM, including all the sources of uncertainty listed above, corresponds to a bounded 5% for the entire tested\* range.

\* Given  $E=4BQ/\pi D$  from Foust<sup>49</sup> as long as the velocity profile is axially symmetric, as it would be for all GaTE system conditions, the constant C can be applied for any flow rate ( $E=CQ$ ).

# Appendix C

## Despiking velocimetry signals

The primary difficulty for UDV capture in a large hot gallium pool is oxide management on the probe tip and its effect on the signal to noise ratio. The UDV system uses a strong degree of correlation between the Doppler shifting of the pulse spectrum<sup>55;85</sup>. If noise weakens the correlation then spurious, non-physical velocities can be interpreted. These spurious signals are well documented in UDV use with several mitigation strategies available<sup>5;86;87</sup>. This creates a noise ‘floor’ where, when attempting to measure turbulence statistics, the fluctuations present in the power spectral density (per frequency) are drowned out when the signal gets weak enough (typically in the higher frequencies). This is shown pictorially in Fig. C.1.

For the strategies available, the phase-space detection strategy outlined by Goring and Nikora<sup>87</sup> is used here to ‘despike’ the velocity to optimize the usable signal. The method

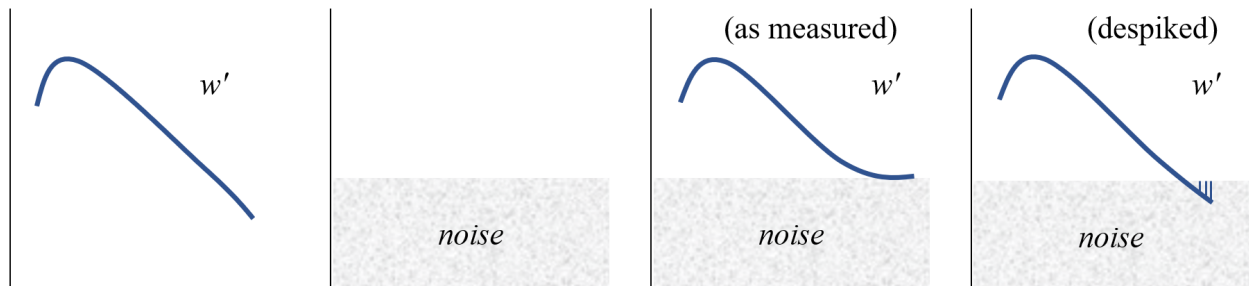


Figure C.1: Pictorial representation of impact noise has on power spectral density of the measured UDV signal. Adapted from Durgesh et. al.<sup>5</sup> to include despiking.

uses the phase-space detection method where differences in the signal, compared to other adjacent locations, are used to determine whether the UDV system has encountered a spike. The universal threshold, the theoretical expected maximum value of  $N$  independent samples drawn from a standard normal distribution<sup>88</sup> ( $\lambda_U = \sqrt{2\ln(N)}$ ), is used to identify spikes. The phase-space (three-dimensional space of  $u$ ,  $\Delta u$ , and  $\Delta^2 u$ ) data are generally in an ellipsoid. Any signal outside of the ellipsoid, defined by relationships between the universal threshold and phase standard deviations, is considered a ‘spike’. After spike replacement by the recommended third order polynomial fit, the standard deviations are recomputed and the process is iterated until no spikes or no change in spikes are detected. This method has had success in other systems making turbulence measurements from UDV sensors<sup>86;89;90</sup>. An example phase space (Fig. C.2) and time series (Fig. C.3) from the GaTE UDV data are shown.

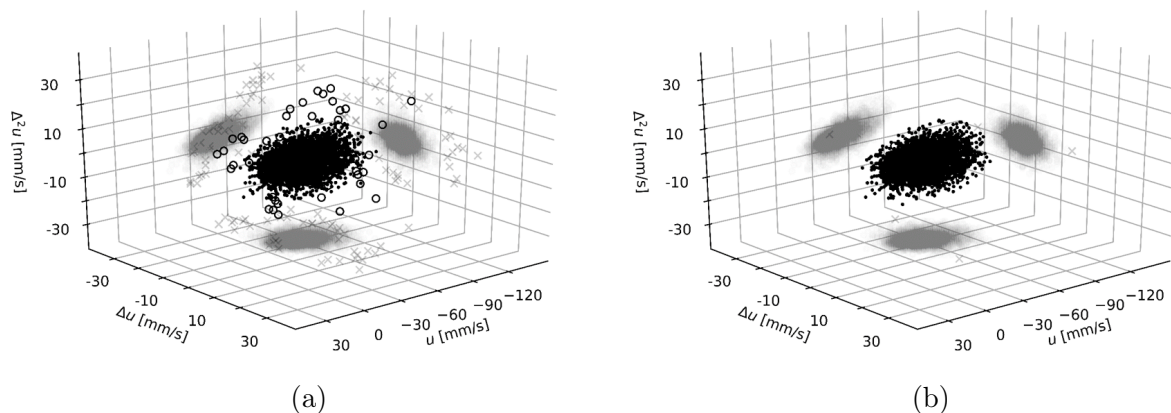


Figure C.2: Phase space of velocity signal from GaTE UDV data. Circles identify the spikes outside of the ellipse. The left figure shows the raw signal; the right shows after the despiking is complete.

The spike detection rate is relatively low in the system. Depending on the depth, 5 to 15 percent of the total signal is despiked. Farther field, near the inlet where the signal is largest, is generally less susceptible to noise. Example power spectral densities are shown in Fig. C.4.

Since the spike detection threshold is based on the standard deviations in phase-space, thermal transients do not benefit as much from the process. Widening of the standard

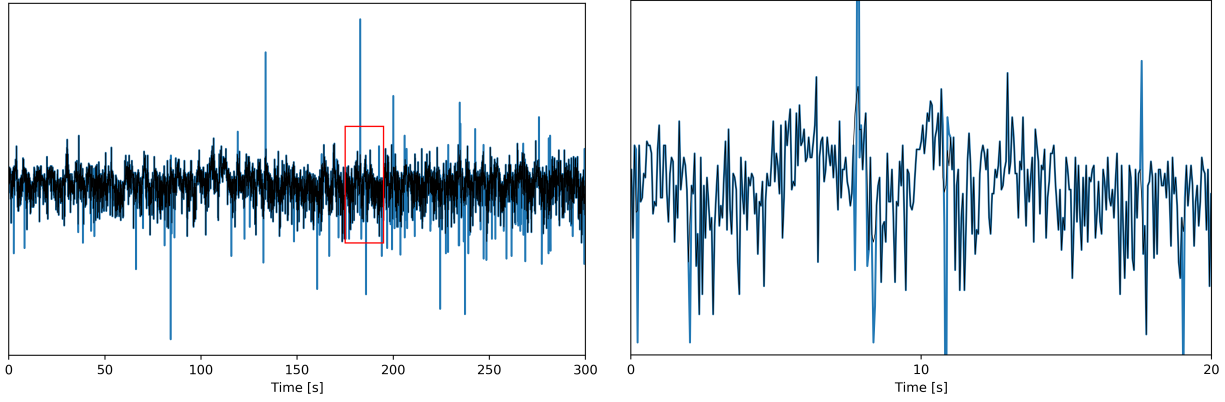


Figure C.3: Entire 6000 point isothermal test data of vertical velocity by time. Blue is raw; black is despiked signal. The red box on the left shows the display area of the right sub-figure.

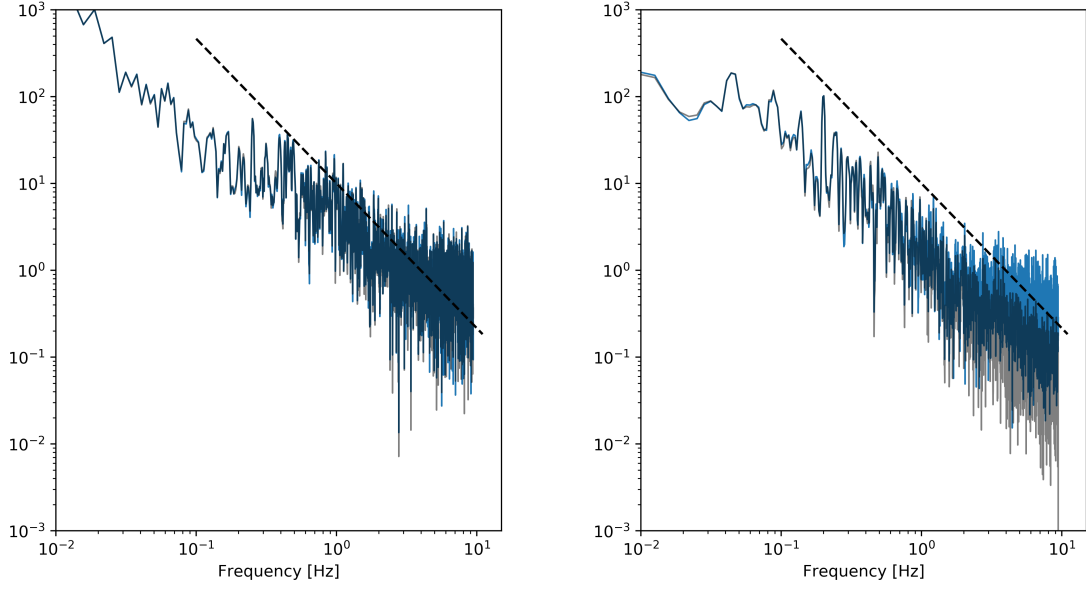


Figure C.4: Power spectral density of the UDV signal. Blue is raw; black is despiked signal; dashed line represents  $-5/3$  power scaling. The relative effectiveness of the despiking method depends on the location within the plenum.

deviation will reduce the spike detection and therefore reduce the effectiveness of the method; however, even with a wider threshold, the process still reduces the more distinct spurious readings and reduces the impact of noise.

# Appendix D

## Python scripts for Chapter 5

```

2 import numpy as np
3 from scipy import signal
4 from scipy import interpolate
5
6 def specfreq(timesize,dt):
7     #function takes the length of the time array and the temporal dt
8     #and returns the corresponding [positive] frequencies
9     return np.fft.fftfreq(timesize,dt)[1:int(timesize/2)]
10
11 def spectrum(sig1,sig2):
12     #function takes two signals of the same size (eg. w'w' or w'T')
13     #and returns the power spectral density similar to
14     #https://currents.soest.hawaii.edu/ocn_data_analysis/
15     #https://currents.soest.hawaii.edu/ocn_data_analysis/_static/Spectrum.html
16     nt = len(sig1)
17     ccf = 1/nt * np.correlate(sig1,sig2,mode='full') #auto or cross correlation
18     psd = np.fft.fftfreq(ccf) #fourier transform of acf/ccf
19     #next line normalizes https://www.fil.ion.ucl.ac.uk/~wpenny/course/fourier.pdf
20     psd = psd * np.exp(1j*np.arange(2*nt-1)*2*np.pi*(nt-1)/(2*nt-1))
21     #next line accounts for imaginary and negative values (phase information is
22     #lost but the amplitude is correct)
23     sigsig = np.abs(np.real(psd)*2)[1:int(nt/2)]
24     return sigsig
25
26 def specpower(spectralfrequency,spectraldensity):
27     #function takes PSD frequency x density and returns integration
28     #by trapezoidal approximation
29     return np.trapz(spectraldensity,x=spectralfrequency)
30
31
32 def readthatdata(velcase,velcase2,nondim):
33     #function takes the case ID in string format
34     #(velcase = U [mm/s]),(first or second) and whether or not
35     #nondimensionalization is required.
36     #returns Tprime (Tpout), Tbar (Tbarout), wp (wpout), wbar (wbarout)
37     #which are all z by time arrays.
38     #the function pulls in the data, creates prime and bar from raw and
39     #interpolates so the arrays are the same size (same z by same time)
40
41     #####
42     ##### TEMPERATURE DATA LOAD #####
43     TempTime = np.load('..\\processdata\\nTime'+velcase+'_'+velcase2+'.npy')
44     TrawtT = np.load('..\\processdata\\T2'+velcase+'_'+velcase2+'.npy')[1:-1,:]
45     if nondim == 1:
46         TrawtT = (TrawtT - 50)/(100-50)
47         TbartT = np.zeros((TrawtT[:,0].size,TrawtT[0,:].size))
48
49     barwindow = 10*0.0525/(int(velcase)/1000) #10 t*
50     windowwidth = int(barwindow/0.045) #10 t*/T_f
51     if int(barwindow/0.045)//2 == (int(barwindow/0.045)+1)//2: #can't be odd
52         windowwidth = int(barwindow/0.045)+1
53     #moving median, moving mean of filter width 10 t*
54     TbartT = signal.savgol_filter(signal.medfilt2d(TrawtT,(windowwidth,1)),\
55                                 windowwidth,1,axis=0)
56
57     TptT = TrawtT - TbartT
58     #####
59     ##### VELOCITY DATA LOAD #####
60     velTime = np.loadtxt('..\\processdata\\velTime'+\
61                         velcase+'_'+velcase2+'.csv',delimiter=',')
62     if nondim == 1:
63         velrawzv = np.load('..\\processdata\\vdsbk'+\
64                           velcase+'_'+velcase2+'.npy')/-int(velcase)
65     else:
66         velrawzv = np.load('..\\processdata\\vdsbk'+\
67                           velcase+'_'+velcase2+'.npy')
68     #####

```

Figure D.1: Routines for PSD and integration and part 1/2 of data input.

```

67 #####
68 ##### LOCATION DATA LOAD #####
69 zout = np.arange(26,86*2.6+52.3,2.6)/1000
70 zv = np.linspace(300.47,0,310)/1000
71 #####
72 ##### RESAMPLE ALL DATA #####
73 timeout = velTime
74 Tpout = np.zeros((timeout.size,zout.size))
75 Tbarout = np.zeros((timeout.size,zout.size))
76 for i in range(len(zout)): #i+10 to start at the exit \
77     # (shared w/ UDV sensing area)
78     f2 = interpolate.interp1d(TempTime, TptT[:,(i+10)]\
79         , fill_value="extrapolate")
80     f3 = interpolate.interp1d(TempTime, Tbart[:,(i+10)]\
81         , fill_value="extrapolate")
82     Tpout[:,i] = f2(timeout+50)
83     Tbarout[:,i] = f3(timeout+50)
84 velraw = np.zeros((timeout.size,zout.size))
85 for i in range(timeout.size):
86     f1 = interpolate.interp1d(zv, velrawzv[i,:], fill_value="extrapolate")
87     velraw[i,:] = f1(zout)
88 wbarout = np.zeros((timeout.size,zout.size))
89 windowwidth = int(barwindow/0.0531) #10 t*/T_f
90 if int(barwindow/0.0531)//2 == (int(barwindow/0.0531)+1)//2:
91     windowwidth = int(barwindow/0.0531)+1
92 wbarout = signal.savgol_filter(signal.medfilt2d(velraw,(windowwidth,1))\
93     ,windowwidth,1,axis=0)
94 wpout = velraw - wbarout
95 #####
96 # Use only the length of a the active transient
97 #this corresponds to a total time window of t*~70
98 if velcase2 == '2' and velcase == '60':
99     Tpout = Tpout[:1227]
100    Tbarout = Tbarout[:1227]
101    wpout = wpout[:1227]
102    wbarout = wbarout[:1227]
103    timeout = timeout[:1227]
104 elif velcase2 == '1' and velcase == '60':
105     Tpout = Tpout[:-50]
106     Tbarout = Tbarout[:-50]
107     wpout = wpout[:-50]
108     wbarout = wbarout[:-50]
109     timeout = timeout[:-50]
110 elif velcase2 == '2' and velcase == '40':
111     Tpout = Tpout[:1855]
112     Tbarout = Tbarout[:1855]
113     wpout = wpout[:1855]
114     wbarout = wbarout[:1855]
115     timeout = timeout[:1855]
116 elif velcase2 == '1' and velcase == '40':
117     Tpout = Tpout[:-150]
118     Tbarout = Tbarout[:-150]
119     wpout = wpout[:-150]
120     wbarout = wbarout[:-150]
121     timeout = timeout[:-150]
122 #####
123 ## OUTPUT FOR USE: Tp, Tbar, wp, wbar x z, time
124 #####
125
126 return Tpout, Tbarout, wpout, wbarout, zout, timeout
127
128
129
130
131
132

```

Figure D.2: Part 2/2 of data input.

```

133 import matplotlib.pyplot as plt
134 #Loop through all four tests
135 for i in range(4):
136     if i == 0:
137         velocity = '40'
138         test = '1'
139     elif i == 1:
140         velocity = '40'
141         test = '2'
142     elif i == 2:
143         velocity = '60'
144         test = '2'
145     elif i == 3:
146         velocity = '60'
147         test = '1'
148
149     ## calculate k_eddy using RAW data nondim != 1
150     Tp, Tbar, wp, wbar, z, time = readthatdata(velocity,test,0)
151     #determine the temperature and velocity gradients w.r.t z
152     dTdz = np.gradient((Tbar),z,axis=1)
153     dWdz = np.gradient((wbar/1000),z,axis=1) #mm/s > m/s conversion
154
155     zcolors = [] #for the axis legend (done last)
156     winnum = 200 # number of temporal divisions per transient
157     #setup the arrays: these are the spectral integrals for each point (z,t)
158     specpowerdTdz = np.zeros((z.size,winnum))
159     specpowerdWdz = np.zeros((z.size,winnum))
160     specpowerwpwp = np.zeros((z.size,winnum))
161     specpowerwpTp = np.zeros((z.size,winnum))
162     #for each point (z,t0-t1) integrate the spectrum
163     for j in range(z.size):
164         for i in range(winnum):
165             ilow = i*time.size//winnum
166             ihigh = (i+1)*time.size//winnum
167             specpowerdTdz[j,i] = \
168                 specpower(specfreq(time[ilow:ihigh].size,0.0531),\
169                             spectrum(dTdz[ilow:ihigh,j],dTdz[ilow:ihigh,j]))
170             specpowerdWdz[j,i] = \
171                 specpower(specfreq(time[ilow:ihigh].size,0.0531),\
172                             spectrum(dWdz[ilow:ihigh,j],dWdz[ilow:ihigh,j]))
173             specpowerwpwp[j,i] = \
174                 specpower(specfreq(time[ilow:ihigh].size,0.0531),\
175                             spectrum(wp[ilow:ihigh,j]/1000,wp[ilow:ihigh,j]/1000))
176             specpowerwpTp[j,i] = \
177                 specpower(specfreq(time[ilow:ihigh].size,0.0531),\
178                             spectrum(Tp[ilow:ihigh,j],wp[ilow:ihigh,j]/1000))
179             zcolors.append((z[-1]-z[j])/(z[-1]-z[0])*0.8)
180
181     #small moving median filtering window to help clarify trends
182     winsize = int((time.size//winnum)/int(velocity)*85)
183     if winsize % 2 == 0:
184         winsize += 1
185     specpowerdTdz = signal.medfilt2d(specpowerdTdz,(winsize,winsize))
186     specpowerdWdz = signal.medfilt2d(specpowerdWdz,(winsize,winsize))
187     specpowerwpwp = signal.medfilt2d(specpowerwpwp,(winsize,winsize))
188     specpowerwpTp = signal.medfilt2d(specpowerwpTp,(winsize,winsize))
189
190     #definitions given by equations of turbulent scaling laws chapters
191     Res = (np.sqrt(specpowerwpwp)*0.053/2.96e-7) #Reynolds number
192     Ris = (9.81*1.2e-4*np.sqrt(specpowerdTdz)/((specpowerdWdz))) #Richardson
193     RetbRi = Res/Ris
194     kappa = np.sqrt(specpowerwpTp)/np.sqrt(specpowerdTdz)
195     kappaguess = 1.2e-5*3.5 #per discussion, there is a non-zero bias in the
196     #w'T' data that is accounted for by the 3.5*molecular_kappa
197     kappa /= kappaguess
198     #and plot with color

```

Figure D.3: Code to interpret and plot  $\kappa$  by  $Re_\tau/Ri$  part 1/2.

```

199     RetbRi = RetbRi.flatten()
200     kappa = kappa.flatten()
201     plt.scatter(RetbRi,kappa\
202                ,s=3,marker='.',alpha=.05,c=np.asarray(zcolors),cmap='plasma')
203
204     plt.loglog()
205     plt.ylim(.5,9.9e2)
206     plt.xlim(1e-1,5e4)
207     plt.xlabel(r'$Re_{\tau}/Ri$')
208     plt.ylabel(r'$\hat{\kappa}$')
209
210     #this produces the empirical curve behind the data
211     U = np.logspace(-3.5,.5,300) #draw an array of representative U
212     Ri = 0.06*.0525/U**2
213     Re = U*0.0525/2.96e-7
214     Rel = .05*U*0.0525/2.96e-7 #5% to 10% turbulence intensity
215     Reu = .1*U*0.0525/2.96e-7
216
217     Prt = .9 + 182.4/(.025*Re**(0.888)) #JIIscha's empirical correlation
218     Rif = Ri/Prt
219
220     def keddr(value): #Shih's empirical correlation
221         if value < 150:
222             output = 1
223         elif value < 1000:
224             output = .015*value
225         else:
226             output = .4*value**.5
227         return output
228
229     #based on the lower and upper estimates for Ret, what are the kappas
230     kelf = np.zeros((U.size))
231     keuf = np.zeros((U.size))
232     for i in range(U.size):
233         kelf[i] = keddr(Rel[i]/Rif[i])
234         keuf[i] = keddr(Reu[i]/Rif[i])
235     #plot band
236     plt.fill_between(Rel/Rif,\
237                    signal.savgol_filter(kelf,51,1),signal.savgol_filter(keuf,51,1)\
238                    ,color='k',alpha=.15)
239
240     #plot color legend
241     z = np.load('z.npy')
242     colors = plt.cm.plasma(np.linspace(.8,0,z.size))
243     lineplot = np.logspace(.8,2.8,z.size)
244     for i in range(z.size-1,0,-1):
245         plt.scatter([0.3],lineplot[i],color=colors[i],marker='s')
246     for i in range(z.size-10,0,-19):
247         plt.annotate(str(int(z[i]*1000)),(.4,lineplot[i]))
248     plt.annotate('Axial Location [mm]',(.15,10),rotation=90)
249
250
251
252
253
254
255
256
257
258
259
260
261
262
263
264

```

Figure D.4: Code to interpret and plot  $\kappa$  by  $Re_{\tau}/Ri$  part 2/2.

# Appendix E

## Instrumentation uncertainty and propagation of uncertainty

This appendix consolidates and presents the instrumentation uncertainty and computes the propagation of uncertainty for computed quantities.

Table [E.1](#) contains the instrument uncertainties obtained either from the manufacturer or as measured in the system.

- The thermocouple (T/C) uncertainty is from the manufacturer but is validated by the IHX water-side boiling transition temperature
- the EMFM is calibrated with uncertainty defined in [Appendix B](#)
- distributed temperature is the sum of squares of the RMS static temperature uncertainty and the tare (T/C) uncertainty
- liquid level is between two stationary electric pickup probes; fill procedures for the GaTE put the level between these two heights
- liquid level perpendicularity is verified using a bubble-level gauge
- UDOP verification is discussed in [Chapter 3](#) but quantities are shown here

| System instrumentation    |              |          |              |
|---------------------------|--------------|----------|--------------|
| Device                    | $\pm$        | $f$ [Hz] | DAQ $f$ [Hz] |
| IHX outlet T/Cs           | 0.75%        | 0.04     | 5            |
| Core inlet T/C            | 0.75%        | 0.04     | 5            |
| Core outlet T/C           | 0.75%        | 3.3      | 5            |
| EMFM (see Appendix B)     | <5%          | –        | 5            |
| Plenum instrumentation    |              |          |              |
| Device                    | $\pm$        | $f$ [Hz] | DAQ $f$ [Hz] |
| Distributed velocity*     | <15%         | –        | 18.8         |
| Distributed temperature** | 3.6%         | –        | 22.8         |
| Liquid level              | +0.0/-4.0 mm | –        | –            |
| Perpendicularity          | 0.7 degrees  | –        | –            |

\*See UDOP verification table for detail  
\*\*Inclusive of both instrument and tare uncertainty  
\*\*with percentage reflecting 1.8°C out of a 50°C $\Delta T$

Table E.1: Instrumentation uncertainties

| Case                      | % error (mean) | RMS uncertainty (%) |
|---------------------------|----------------|---------------------|
| 12.3mm/s (50°C)           | <b>4.8</b>     | <b>14.5</b>         |
| -12.3mm/s (50°C)          | 3.6            | 9.8                 |
| 25mm/s (50°C)             | 0.7            | 10.0                |
| -25mm/s (50°C)            | 0.8            | 9.3                 |
| 25mm/s (75°C)(Not shown)  | 1.5            | 9.0                 |
| -25mm/s (75°C)(Not shown) | 1.8            | 6.5                 |

Table E.2: Distributed velocity verification

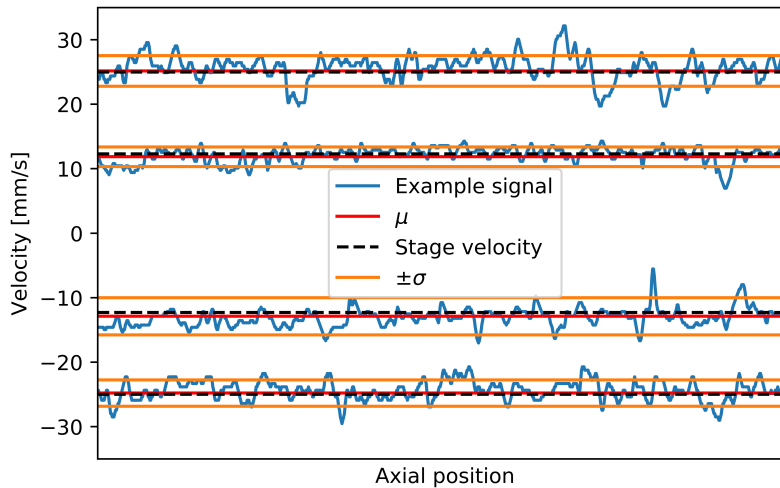


Figure E.1: Figure 3.5 shown here for reference. Verification of UDV snapshot (blue), including mean (red) and  $\pm$  one standard deviation (orange), to axial stage velocities (dashed black).

The UDOP verification information is shown in part in Figure E.1 and Table E.2. The bounding case for the moving axial stage method described in Chapter 3 shows the time independent ( $\bar{w}$ ) uncertainty bounded by 4.8% while the fluctuating uncertainty ( $w'$ ) is bounded by 14.5%. A global modifier for the uncertainty of 1.05% was added to these to account for the change in temperature (and therefore speed of sound), as discussed in Chapter 3. Then the uncertainties for  $w'$  is 14.54% and  $\bar{w}$  is 4.91%.

The root sum of squares approach for adding the independent uncertainties is used to estimate the uncertainties involved in turbulent flux parameters. In the case of gradient quantities, the uncertainty for the measurement is used in slope determination twice (central difference) with residual error associated with  $\mathcal{O}h^2$  (0.0026m, limiting). For example for  $\kappa_\tau$ :

$$\frac{\sigma_{\kappa_\tau}}{\kappa_\tau} = \sqrt{\left(\frac{\sigma_{T'}}{T'}\right)^2 + \left(\frac{\sigma_{w'}}{w'}\right)^2 + \left(\frac{\sigma_{\partial\bar{T}/\partial z}}{\partial\bar{T}/\partial z}\right)^2} = \sqrt{(3.6\%)^2 + (14.54\%)^2 + (2 \cdot 3.6\% + 0.0026^2)^2}$$

(E.1)

= 16.6%

The remainder of the turbulence flux parameters are computed in this way with their results shown in Table E.3.

| Quantity      | function of  | uncertainty (%) |
|---------------|--|-----------------|
| $\kappa_\tau$ | $w', T', \partial\bar{T}/\partial z$                     | 16.6            |
| $\nu_\tau$    | $w'^2, \partial\bar{w}/\partial z$                       | 30.7            |
| $Re_\tau$     | $w'$   | 14.5            |
| $Ri$          | $\partial\bar{T}/\partial z, \partial\bar{w}/\partial z$ | 12.3            |
| $Pr_\tau$     | $\kappa_\tau, \nu_\tau$                                  | 35.0            |
| $Re_\tau/Ri$  | $Re_\tau, Ri$  | 19.1            |

Table E.3: Uncertainty associated with turbulent flux parameters.

# Appendix F

**ICONE28-2020-16661**

ICONE28-2020-16661

## EXPERIMENTAL VALIDATION OF CFD MODELS CAPTURING THE THERMAL-HYDRAULICS IN LIQUID METAL COOLED REACTOR PLENA

Brendan Ward, Thomas Hopkins, Hitesh Bindra  
Nu-EST Lab  
Alan Levin Department of  
Mechanical and Nuclear Engineering  
Kansas State University  
Manhattan, Kansas 66506  
Email: BrendanWard@ksu.edu, HBindra@ksu.edu

### ABSTRACT

High fidelity velocity field experimental data in a liquid metal plenum is presented and compared with numerical simulations. While work has already been established for fluids like air and water, research on low  $Pr$  fluids ( $Pr \ll 1$ ) (e.g. liquid metals) has fewer experimental data sets with validation-quality data. Work in advanced reactors using liquid metal coolant requires validated numerical simulations for safety analyses. The Gallium Thermal-hydraulic Experiment (GaTE) facility is outfitted with acoustic backscattering measurement techniques to generate the high fidelity distributed flow field data in a liquid metal plenum (a 1/20th scale of the Department of Energy's sodium cooled Advanced Burner Test Reactor design). The high spatial and temporal resolution of the sensors are required to capture the fluctuations of velocity to allow a more direct comparison to the numerical simulations. For these simulations the coupled mass and momentum equations under the large eddy simulation (LES) framework were solved with the wall-adapting local eddy-viscosity (WALE) model for sub-grid scale formulations. Since the temperature transients of interest for reactor safety have a period of about a minute in the GaTE system, there may not be enough time to allow statistical tools to check one-to-one correspondence. So the data collection period for both data sets was extended to allow convergence of the mean and a larger sample size for other statistics during system steady-state, isothermal tests. Two characteristic velocities of the plenum inlet barrel

were investigated ( $U = 40, 60$  mm/s;  $Re = 7,000, 11,000$ ). Probability distributions show good agreement between experiment and simulation with the difference only in the low-probability tails that LES is not expected to simulate. The time averaged mean axial distribution of the vertical velocity also shows good agreement between the two setups.

### NOMENCLATURE

$U$  Characteristic velocity  
 $D$  Characteristic length  
 $w$  Vertical velocity field component  
 $\nu$  Kinematic viscosity  
 $\kappa$  Thermal diffusivity  
 $x'$  Fluctuations on variable  $x$   
 $\bar{x}$  Time average on variable  $x$

#### Definition

$Re$  Reynolds number  $UD/\nu$   
 $Pr$  Prandtl number  $\nu/\kappa$

### INTRODUCTION

The thermal-hydraulics of the hot plena of liquid metal cooled reactors plays an important part in understanding accident scenarios. In particular, the tendency for thermal stratification to develop, when colder coolant is introduced from the output of the

reactor at the bottom of the plenum, has implications for natural circulation loop dynamics and solid structure thermal fatigue [1]. In an effort to understand these implications with tests on scaled models, it has been shown that different plenum geometries impact the stratification behavior [2, 3]. Since full scale tests on every potential geometry is not practical there is a need for numerical models.

Computational fluid dynamics (CFD) modeling of liquid metal cooled reactor systems, with their very low Prandtl number ( $Pr \ll 1$ ) and complex geometries, has many challenges [4]. In order to validate these models, scaled-down facilities must be used to capture high fidelity temperature and velocity information [1]. Liquid metal velocimetry using Ultrasonic Doppler Velocimetry (UDV) has shown to be useful in obtaining this information [5,6] but there are few reports that compare UDV to CFD results [7–9]. In order to do this, in the context of nuclear reactor thermal-hydraulics, the Gallium Thermal-hydraulic Experiment (GaTE) was built.

The GaTE plenum is a scaled model of the Advanced Burner Test Reactor [10, 11] that serves as the apparatus to collect experimental temperature and velocity profiles [12, 13]). In this study, UDV observes the axial distribution of the vertical velocity during system steady-state, isothermal conditions and compares them to a corresponding CFD model. Extended data captures (>5 minutes whereas temperature transients typically last  $\approx 1$  min.) allow the use of statistical tools to check and make one-to-one correspondence between the two like systems in order to determine applicability for the faster thermal transients.

Outlined in the following sections are the experimental conditions used to capture the UDV data, the construction and methods used for the corresponding CFD simulation, and the comparison of the two sets of data for two characteristic velocities of plenum inlet barrel:  $U = 40, 60$  mm/s ( $Re = 7,000, 11,000$ ), selected for their proximity to conditions important for studying thermal stratification.

## EXPERIMENTAL SETUP

The GaTE system regulates the inlet condition of the plenum. The system flow rate is driven by a disk-type moving magnet pump (governed by a variable frequency drive with proximity probe speed feedback for stable pump rotational speed). The system flow rate is measured by a transverse field electromagnetic flow meter built in-house; calibration yielded an uncertainty of  $< 5\%$  for all flow rates. The plenum is regulated at  $50^\circ\text{C}$  for the duration of all tests with an uncertainty of  $0.75\%$ . An oil circulation heater and heat exchanger act only to negate any parasitic losses throughout the loop prior to returning to the scaled plenum.

The GaTE scaled plenum is equipped with a rotatable instrumentation platform equipped with a single UDV sensor (TR0405LS - Signal Processing) and distributed temperature

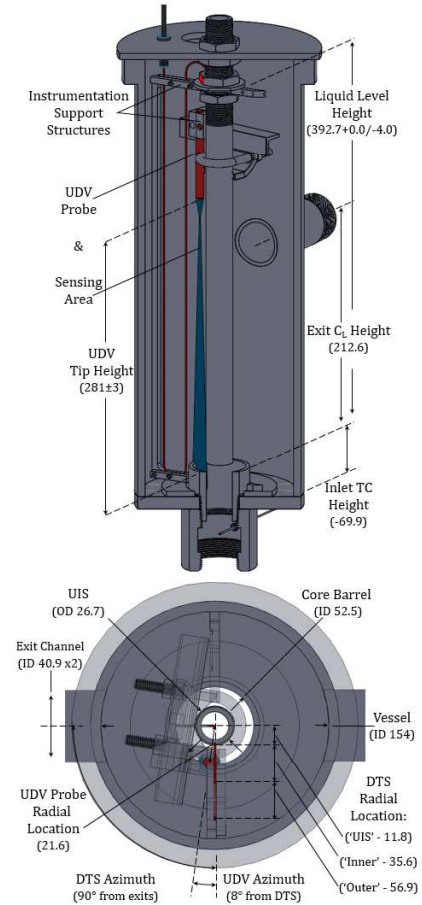


**FIGURE 1: GaTE PLENUM GEOMETRY AND KEY COMPONENT DIMENSIONS AND LOCATIONS.**

sensor (DTS) (the DTS is only used here to ensure steady state temperatures). The UDV probe, and other fixtures of the instrumentation platform and GaTE system are shown in Figure 1. Not shown is the small wiper used to clear the UDV probe tip of accumulated gallium oxide, the tracer particles.

The plenum UDV probe and data acquisition system (DOP4000 - Signal Processing) settings have been optimized for velocity capture in the gallium environment [13]. Every  $800\mu\text{s}$  a  $60V_{pp}$  ('high' DOP4000 [14]) ultrasonic pulse is emitted. With a  $T_{PRF}$  (pulse repetition period) of  $800\mu\text{s}$  and 50 emissions per profile, the recording rate is 18.8Hz. For the 4MHz probes used and the DOP4000 system in gallium, the length of the sampling volumes will be 1.4mm in length. The 0.972mm pitch then can capture the entire axial profile simultaneously with partially overlapping sampling volumes. With these settings, the instrumentation uncertainty is  $\leq 2.5\text{mm/s}$ . Here, in the single probe configuration, mounted vertically 281mm above the inlet and pointed towards the inlet, the vertical component of the velocity will be captured. By convention, velocity tracking towards the probe is

designated with a negative sign.

For the entire data collection period of 6000 profiles (319s) the system is at steady-state (bulk flow and temperature) for an uninterrupted data acquisition sequence. For each data collection sequence the probe tip is cleared of accumulated oxide particles using alcohol based cleaner, is re-positioned into the plenum, and acquisition is triggered. Two characteristic velocities,  $U$ , of the plenum inlet barrel were chosen to be replicated: 40mm/s and 60mm/s with a total of three and nine tests (resp.) each. These velocities correspond to a  $Re$  of 7,000 and 11,000 ( $D = 0.0525\text{m}$ ,  $\nu = 2.96\text{e-}7\text{m}^2/\text{s}$ ). These inlet conditions were then imposed on a simulated geometry of the plenum, as described in the next section.

## NUMERICAL SETUP

The commercial computational fluid dynamics (CFD) code ANSYS Fluent was used to construct a 3D numerical model of the GaTE plenum in order to simulate the experimental physics described earlier. The physics were simulated using simplified boundary conditions with constant inlet flow conditions. The inlet includes modeling of the constriction present in the experimental setup - the heat exchanger outlet (3/4") to the plenum inlet barrel (2") through a reducing bushing. The 3D geometry of the model with inlet and outlet is shown in Figure 2 alongside the meshed geometry. More illustrative captures of the grid details are also provided. Higher refinement for the inlet and lower portion of the plenum, where the velocity is highest, was used to reduce computational burden. It was observed that above the exits the velocity for these conditions drop and a coarser mesh could be used. The resolution within the lower portion of the plenum is 1.4mm. The number of elements in the displayed mesh are 2,426,865 and the number of nodes are 2,517,759. This is with the finalized temporal resolutions of 0.025 and 0.013s ( $U = 40$ , 60mm/s, resp.). It should be noted that this mesh was finalized after grid convergence studies. The isothermal inlet condition was then set to gallium entering at either of the experimental velocities ( $U = 40$  or 60mm/s). The two outlets shown in the figure were subjected to outflow boundary condition, i.e. constant pressure gradient. The top surface (the plane at the maximum height of the plenum) is considered to be a free surface and all the remaining surfaces are considered as walls with zero slip boundary conditions.

The CFD code numerically solves coupled partial differential equations for the problem domain, i.e. Navier Stokes equations; for these isothermal tests, the energy equation is omitted. Numerical simulations were conducted in ANSYS Fluent with the following settings: the Semi-Implicit Method of Pressure Linked Equations (SIMPLE) scheme was used for pressure-velocity coupling, the gradient was computed by least squares cell based method with warped-face gradient correction, and second order spatial discretization for pressure and momentum were

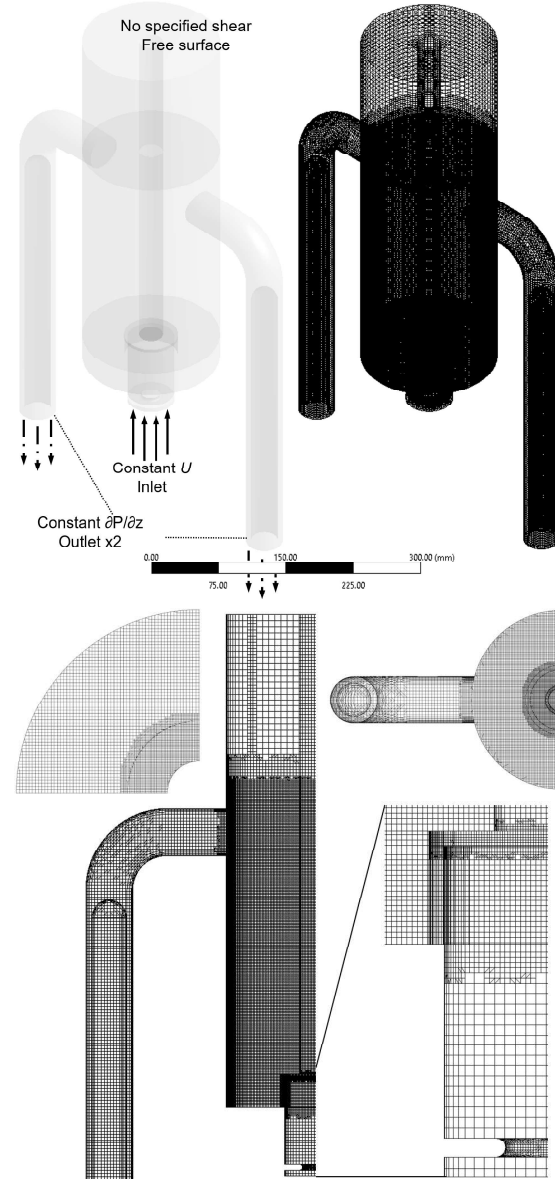


**FIGURE 2:** MESH DETAILS OF THE GaTE PLENUM MODEL.

used with a second order implicit time advancement. Absolute step convergence criteria was set to  $10^{-4}$  for continuity and  $10^{-5}$  for each velocity direction with 40 iterations per step maximum. ANSYS Fluent has several options to select laminar and turbulent flow models. The large eddy simulations (LES) were conducted for all cases with wall-adapting local eddy-viscosity (WALE) model. The settings, models, and mesh were all chosen to best capture the same physics experimentally observed in the GaTE plenum; how well they compare is presented in the following section.

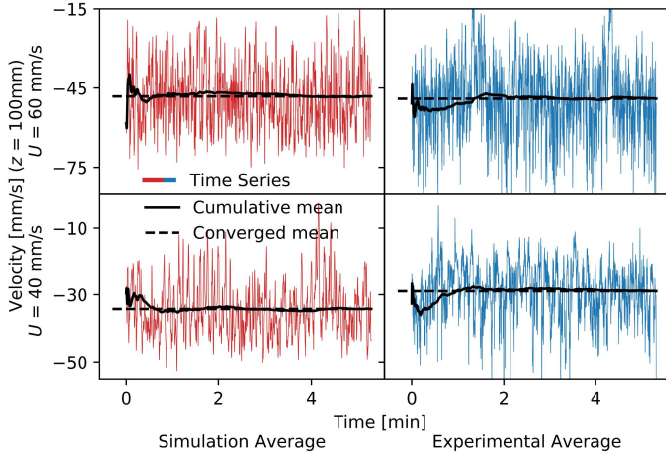


**FIGURE 3: CONVERGENCE IN MEAN VELOCITY.**

## RESULTS

For a commensurable comparison between the LES simulation and the experimental data, the average velocity field for both cannot change in time. Using the definition  $w'(z,t) = w(z,t) - \bar{w}(z)$  of the fluctuating component of the velocity field requires  $\bar{w}(z)$  to be independent of time, i.e. the time window over which the average is obtained must be large enough. In the previous study [13], 9 second windows were used. Comparing multiple 9 second windows showed the plenum dynamics can exhibit drastically different profiles depending on when the data was captured. However, with a longer window the chances of oxide accumulation on the UDV probe impacting the signal/noise ratio also increases. Balancing these resulted in a window length of roughly 5 minutes - a collection of 6000 samples at 18.8Hz. The convergence of example signals for both the experiment as well as the simulation are shown in Figure 3 with satisfactory results.

Comparison of the means at every axial location is included in Figure 4. Example instantaneous and time independent velocity contours show the simulated plenum behavior. The experimental location of the UDV probe is shown in black with the CFD data collection line shown in red. The right sub-figure is the entire time averaged mean axial profile. The immediate near field of the UDV probe ( $\approx 250$ mm and higher) shows over-saturation of the signal while the at 0mm and lower, the signal is obstructed by non-moving solid steel echoes. For the locations in-between, there is agreement between the averages of the experimental runs and the numerical simulation. To better illustrate this agreement, Figure 5 shows the time averaged data from the numerical and all experimental replications. What tests were done and compared in Figure 5 are shown in Table 1. The median is plotted in front of the interquartile range (IQR) and the maximum - minimum of the replications for each axial location. Included in the bottom

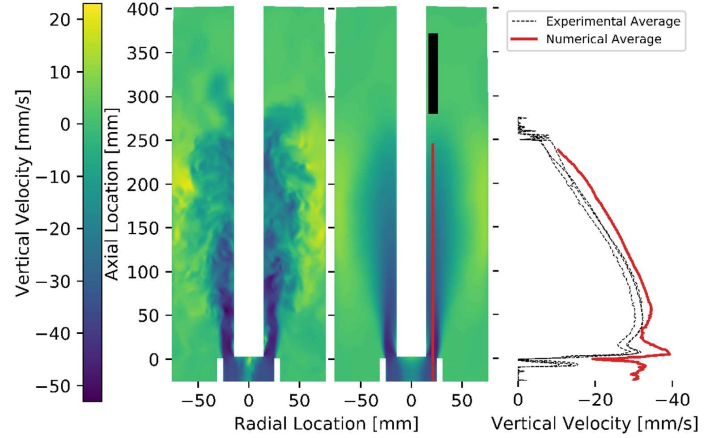


**FIGURE 4: (LEFT TO RIGHT) INSTANTANEOUS AND TIME INDEPENDENT CFD VELOCITY FIELD AND TIME INDEPENDENT AXIAL DISTRIBUTIONS (EXP. AND NUM. DATA COLLECTION LINE),  $U = 40$  mm/s.**

**TABLE 1: CONDITION AND REPLICATION COMPARISON.**

| Data Type | $U$ [mm/s]           | Temp. [ $^{\circ}$ C]   | Replicates |
|-----------|----------------------|-------------------------|------------|
| CFD       | 60, 40               | 50, 50                  | 1, 1       |
| EXP.      | 60, 40 ( $\pm 5\%$ ) | 50, 50 ( $\pm 0.75\%$ ) | 9, 3       |

of Figure 5 is the percent error between these quantities (median, IQR, and max. - min.) and the numerical profile. The absolute difference remains  $< 5$ mm/s from 25mm above the inlet for both cases - the increase in the percent error is attributed to the magnitude of the profile decreasing with nearly constant difference.

The averaging of the velocity profile does not show anything of the dynamics within the plenum. Typically, probability density functions of the velocity fluctuations or increments are able to show the frequency of large-scale eddies and their effect on the field. Since LES simulation solves the energy containing and inertial ranges of the spectrum directly with sub-grid scale models taking over after a cutoff frequency, it has been shown that turbulence statistics comparing LES and experiment should use filtered experimental data [15]. In order to accomplish this filtering a second order Butterworth filter (-12dB/octave) was applied to a filter frequency corresponding to the Taylor microscale ( $\lambda_f^2 = 2u_{rms}^2 / \langle (\frac{\partial u}{\partial z})^2 \rangle$ ). This is shown in Figure 6 where the power spectral density (Fourier transform of the autocorrelation function) of all three signals (simulation, experiment, and filtered experiment) are shown. To see the effect of this filtering a sample time series is shown on the right of the figure.

The data from these two sets of comparable time signals are presented in Figure 7 where their probability densities of  $w'$ , inclusive of all dynamics (as  $\bar{w}$  is independent of time), are shown for the  $z = 100$ mm location. The results are reasonably well

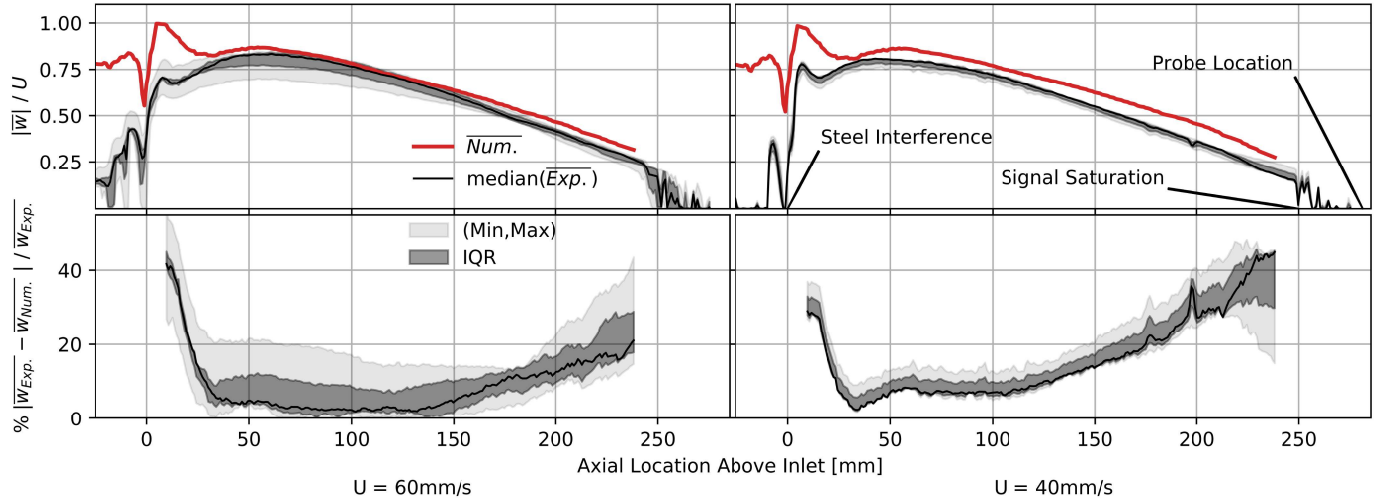


**FIGURE 5:** (TOP) NORMALIZED TIME AVERAGED VELOCITY SIGNALS; (BOTTOM) PERCENT ERROR BETWEEN EXPERIMENTS AND NUMERICAL SIMULATION.

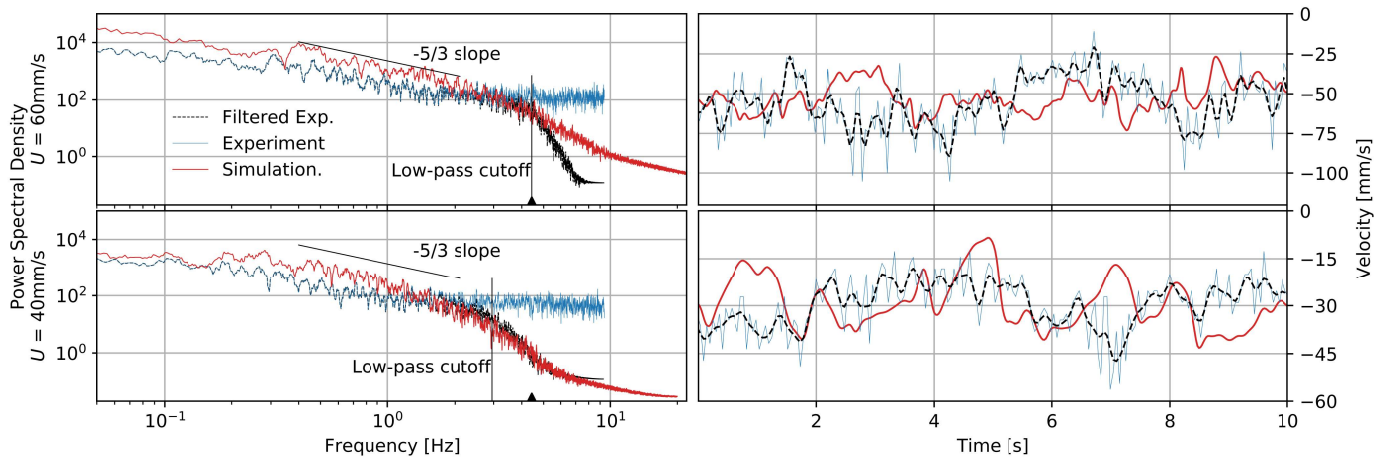


**FIGURE 6:** (LEFT) PSD WITH EXPERIMENT CUTOFF FILTER AT TAYLOR MICROSCALE; (RIGHT) EXAMPLE EFFECT ON TIME SERIES.

matched closer to the mean: within 30% of the experimental median above the  $10^{-2}$  probability for both flow rates. The existence of the low probability tails in the experiments, and not the simulation, is expected. There are more statistical checks that will be performed to verify the dynamic quality of the simulation, but the preliminary checks of the spectral density and probability density of the velocity fluctuations show encouraging results.

## CONCLUSIONS

Experimental UDV measurements and corresponding large eddy simulation CFD data are compared with satisfactory agreement. While some discrepancies exist between the experiment and the simulation data, there are many promising similarities worth further investigation.

The median of the time averaged axial profiles of vertical

velocity match shape and magnitude for both characteristic flow rates ( $U = 40, 60 \text{ mm/s}$ ). Except near the entrance, where solid structure echoes obscure some of the UDV signal, the difference is  $< 5 \text{ mm/s}$  for the remaining axial profile.

Additional checks on the frequency spectrum and probability distribution of the flow field show good dynamic agreement between the two systems. The probability density near the mean shows an error  $< 30\%$  for the  $z = 100 \text{ mm}$  location; the broadened tails of the probability density in the experimental data is consistent with literature (where LES is not expected to exhibit this same behavior).

These results provide some assurance in the validity of the simulations, where time independent as well as preliminary dynamic behavior checks are comparable with the experiments.

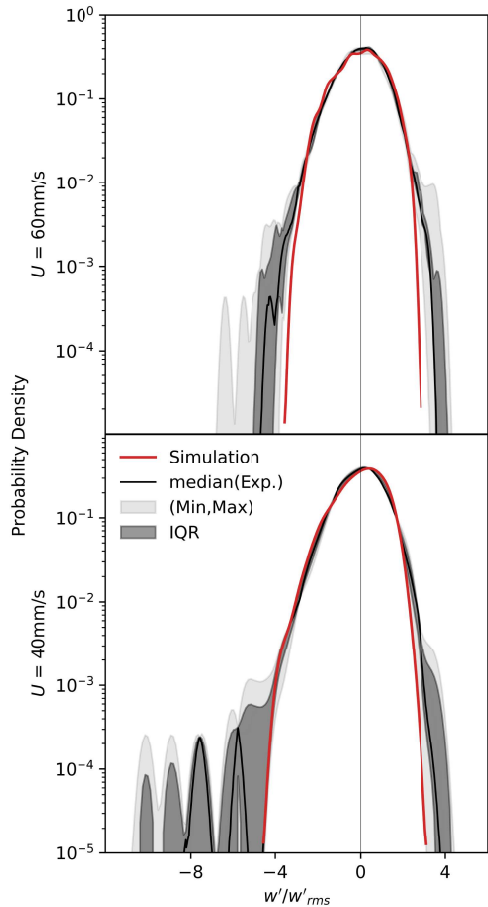


**FIGURE 7:** PROBABILITY DENSITY,  $z = 100\text{mm}$  (KERNEL DENSITY - WINDOW =  $1.06\sigma n^{-1/5}$  - NORMALIZED BY ROOT MEAN SQUARE OF FLUCTUATIONS).

## ACKNOWLEDGMENT

This material is based upon work supported by the Department of Energy under Awards DE-NE0008559 and DE-NE0008498.

## REFERENCES

- [1] Roelofs, F., ed., 2019. *Thermal Hydraulics Aspects of Liquid Metal Cooled Nuclear Reactors*. Elsevier.
- [2] Ieda, Y., Maekawa, I., Muramatsu, T., and Nakanishi, S., 1990. “Experimental and analytical studies of the thermal stratification phenomenon in the outlet plenum of fast breeder reactors”. *Nuclear engineering and design*, **120**(2-3), pp. 403–414.
- [3] Kimura, N., Miyakoshi, H., and Kamide, H., 2012. “Experimental study on thermal stratification in a reactor vessel of innovative sodium-cooled fast reactor—mitigation

approach of temperature gradient across stratification interface—”. *Journal of Nuclear Science and Technology*, **47**(9), Jan, pp. 829–838.

- [4] Grotzbach, G., 2013. “Challenges in low-prandtl number heat transfer simulation and modelling”. *Nuclear Engineering and Design*, **264**, pp. 41–55.
- [5] Cramer, A., Zhang, C., and Eckert, S., 2004. “Local flow structures in liquid metals measured by ultrasonic doppler velocimetry”. *Flow Measurement and Instrumentation*, **15**(3), pp. 145–153.
- [6] Tasaka, Y., Takeda, Y., and Yanagisawa, T., 2008. “Ultrasonic visualization of thermal convective motion in a liquid gallium layer”. *Flow Measurement and Instrumentation*, **19**(3-4), pp. 131–137.
- [7] Chaudhary, R., Thomas, B., and Vanka, S. P., 2012. “Effect of electromagnetic ruler braking (embr) on transient turbulent flow in continuous slab casting using large eddy simulations”. *Metallurgical and Materials Transactions B*, **43**(3), pp. 532–553.
- [8] Avnaim, M., Mikhailovich, B., Azulay, A., and Levy, A., 2018. “Numerical and experimental study of the traveling magnetic field effect on the horizontal solidification in a rectangular cavity part 1: Liquid metal flow under the tmf impact”. *International Journal of Heat and Fluid Flow*, **69**, pp. 23–32.
- [9] Timmel, K., Kratzsch, C., Asad, A., Schurmann, D., Schwarze, R., and Eckert, S., 2017. “Experimental and numerical modeling of fluid flow processes in continuous casting: Results from the limmcast-project”. In IOP Conference Series: Materials Science and Engineering, Vol. 228, IOP Publishing, p. 012019.
- [10] Ward, B., Wiley, A., Wilson, G., and Bindra, H., 2018. “Scaling of thermal stratification or mixing in outlet plena of sfrs”. *Annals of Nuclear Energy*, **112**(1), pp. 431–438.
- [11] Chang, Y., Finck, P., Grandy, C., Cahalan, J., Deitrich, L., Dunn, F., Fallin, D., Farmer, M., Fanning, T., Kim, T., et al., 2008. Advanced burner test reactor preconceptual design report. Tech. rep., Argonne National Laboratory (ANL).
- [12] Ward, B., Clark, J., and Bindra, H., 2019. “Thermal stratification in liquid metal pools under influence of penetrating colder jets”. *Experimental Thermal and Fluid Science*, **103**, pp. 118–125.
- [13] Ward, B., Sieh, B., and Bindra, H., 2019. “Experimental measurement of liquid metal flow fields in a scaled sfr upper plenum”. *18th International Topical Meeting on Nuclear Reactor Thermal Hydraulics (NURETH-18)*.
- [14] Willemetz, 2019. Dop4000 users manual. Tech. rep., Signal Processing S.A. - Switzerland.
- [15] Sagaut, P., 2006. *Large eddy simulation for incompressible flows: an introduction*. Springer Science & Business Media.